# Performance Investigation of Various Cold Thermal Energy Storages

By
David MacPhee

A Thesis Submitted in Partial Fulfillment
of the Requirements for the Degree of

Master of Applied Science in Mechanical Engineering

Faculty of Engineering and Applied Science
University of Ontario Institute of Technology
July 2008

# Abstract

This study deals with the process of solidification and melting of some typical encapsulated ice thermal energy storage geometries. Using ANSYS GAMBIT and FLUENT 6.0 software, fluid motion past cylindrical, slab and spherical capsules containing phase change materials are examined and the resulting energy and exergy efficiencies are analyzed. The main source of irreversibility was from entropy generation due to heat transfer accompanying phase change, although viscous dissipation was included.

All energy efficiencies were well over 99% for all cases; which was found to be quite unreasonable. However, during exergy analysis the efficiencies ranged from around 70% to 92%. It was found that all efficiencies increased with decreased HTF flow rate, while exergetically all processes were most efficient with inlet HTF temperatures closer to the solidification temperature of ice.

The most influential variable affecting exergy efficiency was the inlet HTF temperature, with very small differences in efficiency occurring when varying geometries. Though the most efficient geometries varied according to inlet HTF temperature; the spherical capsules provided competitive values, and due to ease of manufacturing and usage should not be discarded when designing systems such as these.

**Keywords:** Thermal, energy, storage, heat, transfer, energy, exergy, efficiency, encapsulated, ice, charging, numerical, sphere, cylinder, slab, CFD, dissipation, viscous, charging, discharging, flow rate, temperature, geometry, capsule, HTF, TES, PCM.

# Acknowledgements

There are a great number of people who must be acknowledge for the help they have given me during the production of this thesis; I should think that I would not have been able to do it without them. First and foremost, I would like to thank my supervisor, Dr. Ibrahim Dincer, for his guidance and support during my time at UOIT. His vast array of knowledge in many engineering fields provided much needed direction when it was most needed.

To the other professors and post-doctoral researchers whom have helped along the way, I am grateful for their help. Most notably, Dr. Greg Naterer and Dr. Aytunc Erek; their wealth of knowledge has been a constant source for which I have drawn my ideas.

To the many others in the faculty of engineering who have lent a helping hand; to Cristina Preece, who has been very helpful in organizing my graduate affairs, and also Qi Shi, who has been so hospitable about my computing and technical support needs, I am grateful for your assistance.

I would also like to thank Fatih Orhan, who has been there since the beginning, for his companionship and support; it would have been much less interesting not having his friendship during the many late nights studying in the UA building. To my other friends whom I have shared office space with, Yousef Haseli, Ramin Rashidi, and Dr. Mehmet Kanoglu, it was a pleasure to be in your company, and you certainly made life more interesting at times when it seemed dull.

Lastly, I would like to thank my family; Sarah, Brian, Karyn, Bill and Brenda; for without them I wouldn't be here. To Imola, without her company and support, I should think that my life would not nearly be as exciting. To all of you who I have left out during this brief acknowledgement, including the various friends I have made with staff and students along the way, your support has been paramount, and I shall not forget it.

# Table of Contents

# List of Figures

# List of Tables

# Nomenclature

| | | |
|---|---|---|
| $H$ | = | *total specific enthalpy* $\left[J/kg\right]$ |
| $U$ | = | *internal energy* $\left[J/kg\right]$ |
| $t$ | = | *time* $\left[s\right]$ |
| $k$ | = | *thermal conductivity* $\left[W/mK\right]$ |
| $T$ | = | *temperature [K]* |
| $h$ | = | *sensible enthalpy* $\left[J/kg\right]$ |
| $C$ | = | *specific heat capacity* $\left[J/kgK\right]$ |
| $V$ | = | *volume* $\left[m^3\right]$ |
| $u$ | = | *x-velocity* $\left[m/s\right]$ |
| $v$ | = | *y-velocity* $\left[m/s\right]$ |
| $w$ | = | *z-velocity* $\left[m/s\right]$ |
| $L$ | = | *Latent heat* $\left[J/kg\right]$ |
| $p$ | = | *static pressure* $\left[kg/ms^2\right]$ |
| $P$ | = | *total pressure* $\left[kg/ms^2\right]$ |
| $Le$ | = | *length* $\left[m\right]$ |
| $D$ | = | *diameter* $\left[m\right]$ |
| $W$ | = | *wall* |
| $Res$ | = | *Residual Error* |

$Ht$ = *height* $[m]$

$E$ = *total energy* $[J]$

$M$ = *mass* $[kg]$

$S$ = *entropy* $\left[J/K\right]$

$\overline{T}$ = *average temperature* $[K]$

$\vec{P}$ = *average pressure*

$R$ = *radius* $[m]$

## Greek Letters and Special Symbols

$\varepsilon$ = *differential distance* $[m]$

$\rho$ = *density* $\left[kg/m^3\right]$

$\vec{V}$ = *velocity vector* $\left[m/s\right]$

$\vec{i}$ = *unit normal vector in x-direction*

$\vec{j}$ = *unit normal vector in y-direction*

$\vec{k}$ = *unit normal vector in z-direction*

$\vec{f}$ = *wall facet*

$\Xi$ = *total exergy* $[J]$

$\mu$ = *dynamic viscosity* $\left[kg/ms\right]$

$\vec{n}$ = *normal vector*

$\nabla$ = *differential "del" operator*

$\beta$ = *liquid fraction*

$\gamma$ = *dummy variable*

$\in$ = *"is an element of"*

$\notin$ = *"is not an element of"*

| | | |
|---|---|---|
| $\Delta$ | = | *"change in"* |
| $\eta$ | = | *energy efficiency* |
| $\Phi$ | = | *dissipation function* |
| $\psi$ | = | *exergy efficiency* |
| $\infty$ | = | *dead-state* |
| $p^*$ | = | *guessed pressure field* |
| $\frac{D}{Dt}$ | = | *substantial derivative* |
| $\overline{\eta}$ | = | *normalized energy efficiency* |

## Subscripts

| | | |
|---|---|---|
| *l* | = | *latent portion* |
| *i* | = | *ice, inner* |
| *w* | = | *water* |
| *des* | = | *desired* |
| *tot* | = | *total* |
| *cross* | = | *cross-sectional* |
| *wa* | = | *wall* |
| *ns* | = | *no shear* |
| *sf* | = | *solidification* |
| *O* | = | *reference environment* |
| *D* | = | *diameter* |
| *in* | = | *inlet* |
| *C* | = | *cylinder* |
| *S* | = | *slab* |
| *o* | = | *outer* |
| *c* | = | *centroid* |

| | | |
|---|---|---|
| *b* | = | *bulk* |
| *out* | = | *outlet* |
| *pcm* | = | *phase change material* |
| *pvc* | = | *polyvinyl chloride* |
| *htf* | = | *heat transfer fluid* |
| *f* | = | *final* |
| *d* | = | *destroyed* |
| *gen* | = | *generated* |
| *ch* | = | *charging* |
| *dis* | = | *discharging* |
| *sys* | = | *system* |
| *ini* | = | *initial* |
| *cyl* | = | *cylinder* |
| *slab* | = | *slab (rectangular capsule)* |
| *diss* | = | *from viscous dissipation* |
| *trans* | = | *from heat transfer* |

## Superscripts

| | | |
|---|---|---|
| $\gamma$ | = | *dummy variable* |

## Acronyms

| | | |
|---|---|---|
| *AR* | = | *aspect ratio* |
| *PCM* | = | *phase change material* |
| *HTF* | = | *heat transfer fluid* |
| *PVC* | = | *polyvinyl chloride* |
| *TES* | = | *thermal energy storage* |

# 1.0 Introduction

Energy storage is an extremely important part of today's society. In almost every facet of science and technology, energy storage plays a significant role, whether the energy is needed in chemical, heat, mechanical, electrical or potential form. Though the motivation for the recent technological advancements in the various fields of energy storage varies, the overall impetus is the same; our energy supply – whether it comes from the earth or the sun, is never a constant. Day turns to night, winds die down, oil fields eventually run dry, and the geothermal heat from the crust of the earth, although seemingly constant, will eventually diminish. There is, then, a need to store energy, for the purpose of extracting it when it is not readily available. This is clearly evident in solar panels, which convert the sun's radiation into electricity for later use. In fact, the storage of thermal energy perhaps dates back as far as civilization itself; since the beginning of recorded history, people have been harvesting ice to keep things cool when warmer weather approaches. It is this type of thinking which has provided the desire to store many other types of energy from various sources, both for economic and ecologic purposes.

For the past few decades, the world's energy supply has not been keeping up with the increasing demand. Burgeoning countries undergoing industrial reform are consuming an increasing amount of crude oil, coal and electricity, which has contributed to increases of overall energy prices to an unprecedented level. As a result, energy conservation has been on the rise lately, and new sources to feed the human energy hunger are sought without relent. Moreover, the search for more efficient, ecologically friendly and cost effective ways to capture and store energy for later use is always a popular topic.

The opening segment of this thesis will attempt to give the reader an insight into the various types of energy storages and their applications. Finally, the main topic - thermal energy storage using encapsulated ice – will be briefly discussed before a much more intense inquiry into the field will be made in the literature review.

## 1.1.0 Background

As noted earlier, the reasons for energy storage are many. In addition to the economic and ecological benefits of energy storage, some other reasons include portability and reliability. For example, electrochemical batteries provide an excellent portable source of electricity. A typical gas generator, which uses the stored heat of combustion in gasoline, is both portable and reliable. In cases of power failure, the gasoline is combusted, used to propel the rotor of a generator, and electricity is produced. These energy storage types are only a few examples of a huge array of the technologies in use today. At first glance, it is sometimes overwhelming to learn of the astonishing amount of energy storage which is in use in everyday life. However, only the main types of energy storage which will be discussed here, and can be seen in Figure 1.1.

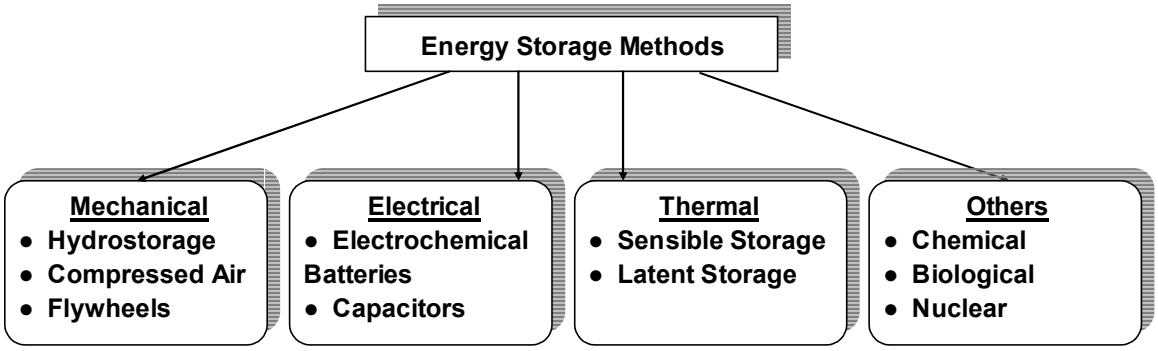


**Figure 1.1: Some of the more common modes of energy storage.**

The different ways of storing mechanical, electrical, thermal energy, and a few others will be discussed, and while there will be a brief outline of each, thermal energy storage will take a front seat in this investigation and will be explained with more rigor.

## 1.1.1 Mechanical Energy Storage

Mechanical energy storage is quite simply as it is stated: mechanical energy, usually in the form of kinetic energy or momentum, can be stored in a number of ways in order to retrieve it at a later date. A great example of mechanical energy storage is the flywheel, which can give or receive rotational energy in times of need. The flywheel is, simply put, a wheel, attached to an axle, which has a known *moment of inertia*, sometimes called the

angular mass. When angular momentum from the axle is transferred to the flywheel, it rotates, storing the angular momentum as angular velocity. This may not seem like a very important type of energy storage at first glance, but a number of public transit vehicles use flywheels to increase energy efficiency. For example, some large city buses, which make frequent stops and as a result can experience terrible fuel efficiencies, can use flywheels to decrease their fuel consumption by up to 50% (Dincer and Rosen, 2002). The premise for this technology is that when the bus makes a stop, the momentum or kinetic energy of the bus is transferred to the flywheel through the axles of the bus, rather than dissipated through its brake pads. When the bus needs to accelerate after the stop is made, the process is reversed and the rotational energy of the flywheel is transferred back to the axle to provide a forward acceleration. Many other vehicles can use flywheels for similar purposes, including subways and trains which require a great deal of energy to both decelerate to a full stop and to accelerate to full speed.

Apart from the flywheel, there are a number of other types of mechanical energy apparent in everyday life. A wind-up wristwatch stores mechanical energy in its internal springs, while hydrostorage and compressed air storage are becoming more popular as energy demand increases. As noted earlier, the energy supply is not constant, so subsequently the price of energy varies as well. Since most electricity generating stations run at a fixed, optimum level, they are usually producing enough electricity to satisfy the entire population. However, when electricity is in low demand, which usually occurs during the night, the electricity production does not stop, because of the start-up costs which these large power plants incur. Instead, electricity is sold at a much cheaper rate, in order to try to level off the energy demand curve. As an example, the Los Angeles Department of Water and Power gives an overnight electricity rate of 50 to 60% less expensive than at day for its residents. So, for those wishing to both save money and, ultimately, conserve energy, the storage of energy is a viable option.

Hydrostorage is one way of storing energy in the form of gravitational potential (mechanical) energy. At night, when electricity rates are much less expensive, pumps are used to pump water from a lower elevation to a higher elevation. When electricity rates increase, this hydrostorage can be used to run turbines and generate electricity at a fraction of the original cost. Compressed air storage works in a similar way; when

electricity demand is low; air is compressed into a storage tank, and is used to run turbines during high demand times.

Though mechanical energy storage is both versatile and useful, it is the chemical energy storage field which has received the greatest amount of attention, and will be discussed next.

### 1.1.2 Electrical Energy Storage

The storage of electrical energy has become increasingly important since Alessandro Volta invented the electric cell in 1800. Though the first battery was relatively crude, consisting of a copper and zinc electrode submersed in sulfuric acid, the battery industry, which powers all of the worlds cell phones and laptops, has been growing ever since.

Although the battery belongs to a certain branch of electrical energy storage systems called electrochemical storage, there are many other applications of electrical storage types which are very important in the world today. Capacitors, for example, are devices that can store energy in the electric field between two charged plates. They are more commonly used in electronic devices to keep a more constant power supply, while batteries are being changed or charged. Studies are currently underway to develop electrochemical double layer capacitors called *supercapacitors*. These devices can store an amount of electrical energy similar to that of the rechargeable battery, while retaining a shelf life thousands of times greater than the current rechargeable batteries on the commercial market today.

Most of the other types of electrical energy storage systems rely on converting excess electrical energy to other forms; including mechanical, chemical, and most importantly to this thesis, thermal forms. However, before the basics of thermal energy storage are addressed, a few other types of energy storage will be discussed next.

### 1.1.3 Others

There are a number of other modes of energy storage which have important roles in helping to satisfy the world's energy demand, and these include chemical, biological and nuclear energy storage.

The future of society may one day depend heavily on chemical energy storage; the hydrogen economy, which has been developing rapidly over the past few years, may provide a safe and ecologically friendly way to store electrical energy in the form of hydrogen. The premise for the storage of energy in hydrogen is straightforward; energy can be used to move hydrogen atoms from a lower energy state (for example, water) to a higher energy state (for example, hydrogen gas). Electricity can be used in the reverse of a voltaic cell to split hydrogen from water to produce hydrogen and oxygen gas, to perform this feat. The hydrogen gas can then be used electrochemically in fuel cells or can be burned to drive generators – both of which are completely harmless to the environment, as water is the only byproduct of these reactions.

Biological energy storage, which can be seen all around us, is indeed almost as old as life itself. Almost all living organisms store energy in some form, in order to extract it when energy supplies are low. For example, plants can store excess energy in the form of starches or other carbon compounds, which can be readily broken down into glucose and used for cell respiration. Animals, on the other hand, can store excess energy in the form of fats, glycogen or other compounds which again can be broken down into glucose for the ultimate purpose of extracting energy from it. Thus, although the concepts in energy storage can sometimes seem complicated and foreign, the main metabolic functions which keep us all alive are ultimately dependent on biochemical and biological energy storage.

Although technology is not yet advanced enough to viably store energy in nuclear materials, we have been extracting nuclear energy from radioactive materials for decades. In fact, nuclear fission reactors are becoming more and more popular as time progresses, due to the decreased environmental and global warming effects incurred when compared to fossil fuel burning. The mass-energy equivalence, which is the basis for nuclear reactions, was discovered in the early 1900s by Albert Einstein. The conversion between energy and mass in readily obtainable mediums is still in its infancy, and it will become a more viable option in the future.

Although chemical, biological and nuclear energy storage make up the remaining popular modes of energy storage; there is another mode which this thesis will delve into more thoroughly: thermal storage. Thermal energy storage (TES) has attracted an

increasing interest in the past few decades, though the research into this area is relatively nonexistent before the 1980's. TES is perhaps the simplest of all means of energy storage; energy in the form of heat (or cold) is stored in a medium, and that thermal energy is later extracted for various heating or cooling purposes. The next section will develop a more thorough understanding of the various types of TES and their applications.

## 1.2.0 Thermal Energy Storage

Before getting into the fundamentals of TES, the reader should be directed to an excellent resource when dealing with any aspect of TES (Dincer and Rosen, 2002). This book provides a wealth of information to anyone looking to learn and study TES, whether at the graduate or undergraduate level.

TES can be stored in of two ways: latent and/or sensible storage. Latent storage refers to the energy change in a substance as it undergoes a change in phase, say from liquid to solid (as ice freezes) or from a liquid to a gas (as water boils). As the material changes state during what is called a *phase transition*, energy is released or absorbed, depending on the direction of the process. The advantage of latent storage is that the energy released/absorbed can be done so at a constant temperature, making the process easier to regulate. However, since phase transitions occur for certain substances only at a certain temperature and pressure, there is sometimes trouble in finding the right phase change material (PCM) to suit certain processes.

In contrast, sensible thermal storage is the energy stored in a change in temperature of a material. All materials have a property called a *specific heat*, which loosely means the amount of energy it takes to change the temperature of one kilogram of a substance by one degree. For example, water at 5ºC has a specific heat of $4.2\,kJ/kgK$. This means that it takes 4.2 kilojoules of energy to change the temperature of one kilogram of water by one degree at 5ºC. Thus, energy can be stored in the temperature change of any material, and since the temperature at which energy is released and stored is variable, sensible TES is applicable to almost any application. However, one of the main drawbacks of sensible TES is its large storage size. For example, freezing just one

kilogram of ice will absorb 334 kJ of energy, while over 79 kg of water would be needed to store the same amount of energy at a temperature difference of 1ºC.

Though each method has its own attractiveness and drawbacks, they both have a place in TES, and are both used for both warm and cool TES.

### 1.2.1 Heat Storage

There are many good methods and sources used to store warm thermal energy. These include solar heaters, solar ponds, geothermal storage methods, and many others. The advantage of warm thermal energy storage is that usually, the warm TES is obtained from an abundant and ecologically friendly source, such as the sun. As a result, heat storage is usually very cost friendly and good for the environment.

Apart from solar energy, warm TES can use waste heat from industrial processes or geothermal energy as a source. For example, geothermal regulators are currently in place at the University Of Ontario Institute Of Technology, which use bored holes into the ground and a heat transfer fluid as the storage medium. During the winter, when the temperature is quite cold outside, a heat transfer fluid is passed through these deep wells and receives heat from the ground, kept constant at a temperature of around 10ºC year-round. The heat transfer fluid can then be used to help heating processes indoors. During the summer, the reverse process occurs: the heat transfer fluid gives off heat energy to the ground and receives it from the air indoors, to help share the air conditioning load.

Latent TES also plays a large role in heat storage. Paraffin waxes, with melting points well over that of water, can achieve relatively large latent heat of fusions, and as a result are used as a phase change material in many heat storage applications. These include solar water heaters and solar collectors, both of which are used in the heating industry. Paraffins, along with many other materials including brines, eutectic salts and some acidic compounds, make for excellent TES mediums, and the search continues for more to suit individual purposes more precisely.

### 1.2.2 Cold Storage

At first glance, the notion of cold thermal energy can be confusing. Since higher energy sources are usually of higher temperature, the concept of "cold energy" can seem contradictory. However, cold energy is a very useful commodity in everyday life. Refrigerators, freezers and air conditioners are all examples of industrial processes which create heat sinks (or extract heat from a medium) which can be referred to as a cold energy source, without loss of generality.

Cold TES is related to various research fields, such as material science, heat and mass transfer, surface science, crystallography, and automatic control (Saito, 2002). It has become much more important in recent years, due to the increased energy demand in most parts of the world. For example, large office buildings in the more tropical parts of the world can spend immense amounts of money and energy in air conditioning alone. As a result, there is a desire to shift the usage electricity from high demand times to lower demand times. This is usually done by storing thermal energy from a cooling system, run with electricity at night, so that the cold thermal energy can be extracted during peak cooling periods during the day. Not only does this save money in electricity costs, but it helps smooth out the electricity demand curve, so that larger power-plants need not be constructed. This helps to alleviate the human dependence on natural resources as more sustainable energy sources are discovered.

Traditionally, cooling is accomplished with a vapor compression refrigeration cycle, which uses an electrically driven pump to drive heat from a cool source to a hot one. However, in recent years, other refrigeration techniques are emerging, including absorption chillers, vacuum cooling, night ventilation, evaporative cooling, desiccant cooling and night sky radiative cooling (Paksoy, 2003). Cold TES can use any of these techniques to cool a medium, which can accept heat from a warm source at a later date to aid in cooling processes.

The materials for cold TES are usually limited to water and eutectic salts. The reason for this is the incredibly low cost of water, and also because of its relatively high heat capacity, as noted earlier. Water has one of the highest latent heat of fusions and sensible heats known, and due to its extremely low cost, it is used almost exclusively in cold TES. However, since it freezes only at a specified temperature and pressure,

eutectic salts are sometime used in conjunction with the water. Eutectic salts are simply a combination of inorganic salts, water and other elements, which create a mixture that will freeze at a desired temperature. Using these eutectic salts can help create materials which are ideal for each cold TES process.

The various types of cold TES can store the cold energy in either latent or sensible ways. Sensible cold TES methods are usually limited to cold water chillers. In these devices, water is chilled (much like an air conditioner chills air) to cooler temperatures at night and stored for future times. Although sensible cold TES is quite simple and cost-effective, the size of these devices, as noted earlier, is quite large when compared to ice storage.

Ice storage for latent cold TES can include a host of methods, including ice harvesting, ice slurry, ice-on-coil and encapsulated ice TES. Ice harvesting, which has been used for centuries, is as simple as it sounds. Ice, which is frozen during the winter in the cooler parts of the world, can be harvested during these colder periods and used as a coolant when temperatures rise. Though this is extremely simple, cost effective and environmentally benign, it is not possible in all parts of the world, which is why other methods of cold TES have been developed.

Ice slurries utilize a brine solution, usually a glycol (antifreeze), which can carry tiny ice particles to or from the desired source. The ice is frozen using a number of methods -which will be discussed in section 3.3.1 in more detail - and the result is a sludge mixture of ice and antifreeze. The thermal storage, which has a reasonably high volumetric heat capacity and is extremely portable, can be directly used in air conditioning applications. However, due to its high start-up and maintenance costs, ice on coil systems and encapsulated ice TES are more frequently used.

Ice-on-coil systems use a coil, which contains sub-cooled antifreeze, immersed in water, to freeze the surrounding water. A vapor-compression refrigeration cycle is usually used for the refrigeration purposes. When the time comes to extract the cold energy, warmer antifreeze can be passed through the coils to dismiss heat (in an internal system) or the ice can be melted from outside the coils and used (in an external system). Ice-on-coil systems, though fairly simple in concept, are still quite expensive to implement on large scales. It is for this reason why encapsulated ice TES systems are

becoming more popular; the low startup cost and high energy savings rates make it one of the best methods for cold latent TES.

The focus of this thesis is concerned with encapsulated ice TES. This is due to a number of factors, including its low cost and attractive economic and environmental benefits. The utilization of encapsulated ice TES, along with other modes of TES, reduces electricity demand, reduces electricity costs, and ultimately lowers carbon emissions through a lowered energy demand. These benefits are the main impetus for the current level of research into encapsulated ice TES.

Encapsulated ice TES utilizes a brine solution, which is again usually a glycol solution, to freeze de-ionized water which is encapsulated in plastic capsules (usually made of PVC, due to its low cost, non-volatility and high durability). The capsules are usually made in a spherical shape, but other geometries including rectangular prism, cylindrical and annular shapes are also possible. These capsules are contained in a large storage tank, and the glycol solution is cooled via any of the above techniques to lower its temperature to below the freezing point of water. During the night, the heat transfer fluid freezes the encapsulated water, and during the day, it can be used as a heat transfer medium between the load (building) and the storage tank. The heat transfer fluid receives heat from the building, and delivers it to the ice capsules, which reduces the overall electricity consumption, saving money and reducing environmental impact.

It is due to the attractiveness of encapsulated ice TES that this thesis has been undertaken, to more specifically assess the shortcomings and advantages of these processes. However, before the problem specification and solution procedures can be addressed, the motivations and objectives for this research project are to be outlined first.

# 2.0 Motivation and Objectives

The motives for this study are straightforward. All over the world, encapsulated ice TES systems are becoming more and more popular. This is due partly to the wildly increasing energy demand, which results in increasing electricity rates. There is another great advantage of encapsulated ice TES, though, which is the environmental benefits resulting from its use. Since the storage of thermal energy at night periods can help level off energy demand curves, the use of systems such as these help to lower overall electricity generation from environmentally malignant sources. Since a portion of all electricity is generated from coal, oil or natural gas fired power-plants, lowering the peak electricity demand will result in a lowered overall greenhouse gas emission from these power-plants. In addition to this, the differences between peak and off-peak energy prices electricity prices puts an added incentive to use electricity at night (when electricity rates are less expensive) in lieu of during the day (when electricity rates are more expensive) to save money. One of the most practical reasons for the use of cold TES is to implement an extra cooling load without altering existing air conditioning systems. These systems can be installed and run in conjunction with existing systems to help alleviate any extra cooling loads that may be required during particularly hot days. These environmental and economical concerns are just a few of the reasons why Encapsulated Ice TES must be considered when building any large scale cooling system. However, the current research level into this field is lacking far behind the other modes of TES, which is surprising due to its popularity. The hope is that the end result of this project will fill a void in the current level of research by analyzing the charging and discharging processes of the ice storage tank at the capsule level. Using a commercially available computational fluid dynamics and heat transfer software program, the following specific objectives are met:

- Energy investigation of the charging and discharging processes
- Exergy investigation of the charging and discharging processes
- Effect of geometry on the performance of the above processes, including
    - spherical capsules
    - rectangular (slab) capsules
    - cylindrical capsules

- Effect of aspect ratio of the above capsules on overall performance
- Effect of inlet heat transfer fluid temperature on performance
- Effect of inlet heat transfer fluid flow rate on performance
- Effect of ambient temperature on performance
- Quantities and locations of exergy destroyed in both processes
- In-depth discussion of the advantages of exergy and energy analyses over energy analyses alone and the differences therein.

It is anticipated that the results put forward in this thesis will encourage designers or researchers in the field of encapsulated ice TES to dwell more on the flow characteristics, heat transfer and thermodynamic aspects of the system on a capsule level to provide better performance and efficiency of the system as a whole.

# 3.0 Literature Review

The following comprehensive review of materials found in existing literature will focus first on broad analyses of TES systems as a whole. While sensible systems will be briefly addressed, the main concentration will be on systems employing latent storage concepts, including both warm and cool thermal storage. Concerning the former, there is a considerable amount of research available, with both micro-encapsulation and packed bed techniques used to store the thermal energy. In the case of the cool latent storage, encapsulated ice (packed bed) is a main proponent, as is ice slurry, ice on coil and ice-harvesting.

The design and optimization of TES systems has drawn specific attention, since it is the ecologic and economic benefits to this technology which make it an attractive alternative in the first place. There are two main streams of research in this area; works which concentrate on the storage tank as a whole, and ones which concentrate on the thermal energy storage and retrieval process on the scale of the single capsule. For each, there are a number of techniques used, which can be broadly grouped as either analytical or numerical techniques. Experimental data in this field is also a common verification tool for many of the works studied here. A more detailed flow diagram of the various families of TES research is included in Figure 3.1, which will assist in the thought process as the literature is presented.

## 3.1.0 TES Systems and Applications – Overview

The storage of thermal energy is very important to many engineering applications. For example, there is a need for waste heat recovery systems for systems where the waste heat availability and utilization times are different. Similarly, for systems such as solar heat collectors, there needs to be an effective medium in which to store the energy for night usage or even on cloudy days. An effective review on some of the main storage mediums can be found in Hasnain *et al*. (1998). As expected, there are two main types – sensible and latent systems. Sensible systems harness the specific heat of materials, which include both liquid and solid materials. Latent systems store thermal energy in the

form of a change in phase, and do not require vast temperature differences to store thermal energy, and can be stored in a variety of PCMs.

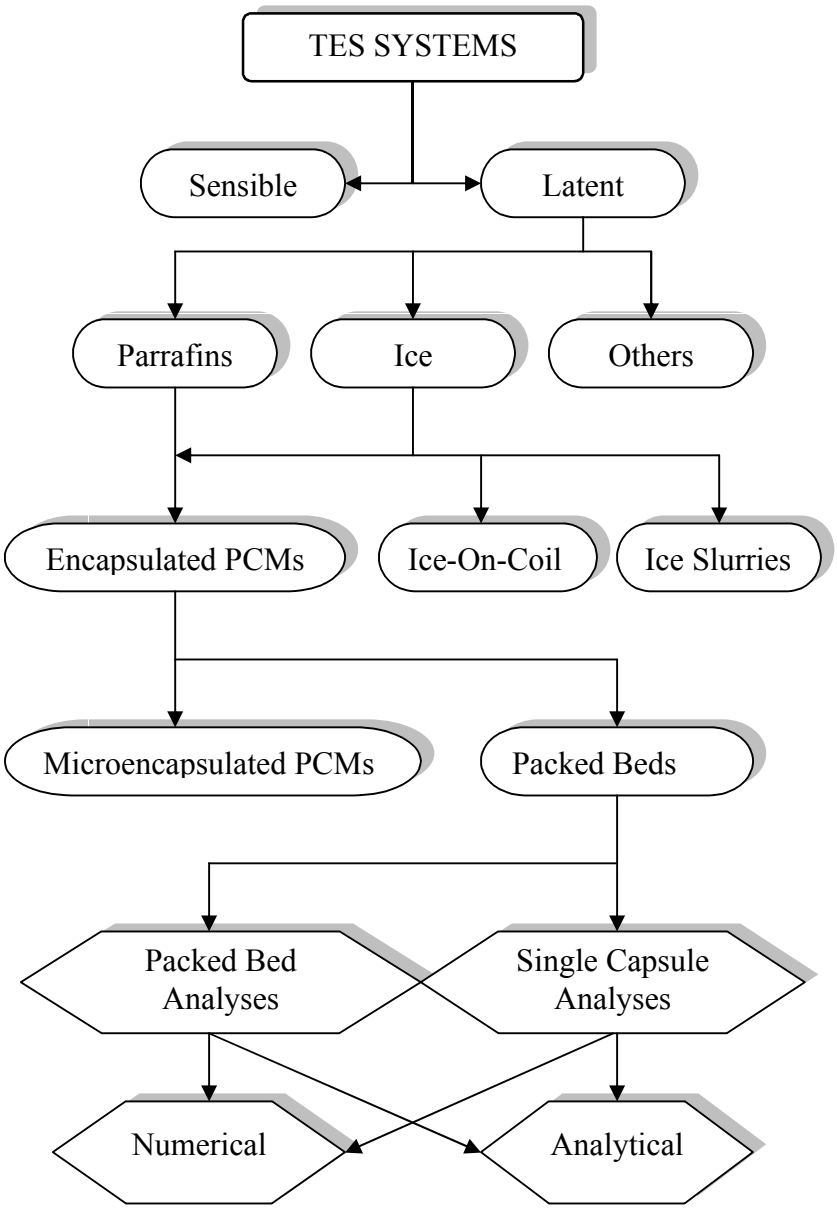


**Figure 3.1: Literature review flowchart.**

### 3.1.1 Sensible TES Systems

The review of works in sensible TES systems is interesting to note, though it is not exactly pertinent to the purpose of this study. Sensible thermal storage is possible in a wide number of mediums, both liquid and solid. Liquid media for thermal storage

include oils, water, molten salts, etc. while solid media are usually in the form of rock or metals, and can include alloys such as zirconium oxide for extreme temperatures [Nsofor, 2005]. There are a number of works regarding both cases, though here we will consider two short examples; a solar pond and a rock bed, both designed for solar energy storage.

Karakilcik *et al*. (2006) perform an interesting performance investigation of a solar pond in Adana, Turkey. The pond was filled with salty water to form three zones of varying density which do not mix. The upper zone is the freshwater layer at the top of the pond, and is fed by rainwater and feed water to compensate for water lost by evaporation. The middle layer, called the insulation zone, is designed to keep the freshwater zone and the lower zone from mixing, while absorbing solar energy in the form of heat. The lower zone, which is the densest mixture, retains the most heat, and absorbs the most heat from the sun, contains the heat exchangers to the solar pond and exchanges heat with both the bottom of the solar tank as well as the insulation zone. As expected, the highest thermal efficiencies of the system came in mid-summer, when solar and ground radiation levels are at their highest and temperature gradients are quite low.

A performance investigation of a solar air heater connected to a rock bed thermal storage device is considered by Choudhury *et al*. (1995). A two-pass, single cover solar air heater is coupled to the rock bed, while operational parameters and geometric design are varied in order to study the effect on efficiency. Factors such as charging time, rock bed size, individual rock size, air velocity and void fraction are studied, as are the effects on thermal efficiency of the system. It was found that the charging time had the most significant effect on the overall efficiency, with the optimal charging time set at 8 hours for this particular location in New Delhi.

There are many other applications pertaining to sensible thermal storage but the main focus here is to present latent TES systems and the current research therein.

### 3.1.2 Latent TES Systems

Latent TES systems have become much more viable for a high volumetric heat capacity. Usually, latent systems can store much more thermal energy for a given volume, require less of a temperature gradient, and can be used for both hot and cold thermal energy

storage, depending on the material (this is discussed in section 3.3). A comprehensive review of the various types of systems can be found in Sharma and Sagara (2007) where various applications and PCM innovations are discussed. Briefly, some of these applications include space heating and cooling, solar cooking, greenhouse upkeep, solar water heating and waste recovery systems. However, it is the design, control and analysis of these systems which researchers are most concerned with. As examples, a solar water heating system utilizing encapsulated PCM, an ice-on-coil laboratory unit and an encapsulated ice industrial refrigeration system are presented, as well as past and present methods for system optimization.

Latent solar-water heating systems are a perfect example of the advantage of thermal energy stored in PCMs. Nallusamy *et al*. (2006) study the performance of a solar collector, coupled with a storage tank filled with encapsulated PCMs, which in this case is paraffin. Water is used as the heat transfer fluid, and the inlet temperature to the storage tank was varied to study the effects of bed porosity and flow rate on overall system performance. It was found that the latent storage system drastically reduced the size of the solar heat storage system, and that these systems are best used for intermittent usage where the latent heat can be best used.

Lee and Jones (1996) studied an ice-on-coil TES unit perfect for residential and light commercial conditions. The chiller, a vapor compression refrigeration cycle using Refrigerant R22, freezes the water inside the evaporator tubes during charging, for the purpose of extraction during peak energy times. The unit was tested varying both evaporator and condenser temperatures, and parameters such as the ice-building rate, the compressor power, cooling rate, heating rate, energy efficiency ratio and power consumption factor are studied. The results indicate that, among other things, the energy efficiency increased with a decreased condenser temperature. The energy efficiency is also readily calculable and heat transfer rates are easily obtainable, which is an encouraging aspect of many TES systems when attempting to minimize energy losses.

An encapsulated ice refrigeration system is studied in Cheralathan *et al*. (2007). In thesis, the experimental investigation of a cylindrical storage tank, laden with spherical capsules made of PVC is examined. The heat transfer fluid is a 30% ethylene glycol solution, which is cooled from the evaporator of a vapor compression refrigeration cycle

using refrigerant R134a. The study is focused mainly on the dependence of the average charging rate, stored energy and specific energy consumption on the heat transfer fluid inlet temperature. Experiments are also determined to test the decrease in specific energy consumption without storage. The results are similar to that in Lee and Jones (1996); a decrease in the evaporator temperature and an increase in the condenser temperature both lead to drastically higher specific energy consumption and lower energy efficiency. However, this study furthers others in its area in the sense that it offers a specific range of HTF inlet temperatures and porosity values for optimal performance of the system.

Many other studies have been conducted to attempt to optimize various TES systems. Henze (2003) presents an overview of the control for central cooling plants with ice TES. The control algorithms target the minimization of energy usage and minimizing demand costs, to name a few. Fully optimal control, based on full system knowledge, is also introduced. The main arguments here state that depending on the specific objectives of the system, a control algorithm can be utilized which optimizes the objectives in a concise manner. Henze (2006) furthers this by investigating the relationships between cost savings and energy consumption associated with the conventional control of typical TES systems. Items accounted for in these optimizations include varying fan power consumption, as well as chiller and storage coefficient of performance. The results indicate that buildings can be operated in such a manner as to reduce overall costs, with only a small increase in total energy consumption.

Another interesting application of PCMs is the regulation of indoor temperatures when rapid changes occur in the surrounding outdoor temperature. Khudhair and Farid (2004) discuss, among other latent TES applications, the advantages of PCMs installed in concrete, gypsum, wallboards, ceilings and floors to limit the effects of outdoor temperature swings on indoor temperatures. These PCMs can act as a heat source while solidifying during cooler indoor temperatures, or a heat sink when melting during warmer indoor temperatures, by having a fusion point close to that of room temperature. Latent TES by means of solar energy and peak load shifting by running a refrigeration cycle are also discussed, as are many other advantages and typical drawbacks of these systems.

It has been conventional, as has been done in the above works, to use energy consumption, energy efficiency and cost minimization as the main benchmarks in

determining optimal system configurations. However, in recent years, a new approach has been exercised which simultaneously reduces both energy and cost inputs. These *exergy analyses* have been the preferred method of late to better analyze the performance of these systems, as well as the location and severity of energy losses. Rosen and Dincer (2003) discuss the usefulness of exergy analysis in the performance and optimization of various TES systems. During exergetic analyses of aquifer, stratified storage and cold TES systems, appropriate efficiency measures are introduced, is the increasing importance of temperature, especially during cold TES.

Rosen *et al*. (1999) provide detailed exergy analyses of many types of cold TES systems. They consider full cycles of charging, storage and discharging in both sensible and latent systems. The results indicate that exergy clearly provides a more realistic and accurate measure of the performance of a cold TES system, since it treats "cold" as a valuable commodity. This is in contrast to the energy analysis, which treats cold as an undesirable commodity. In addition, it was summarized that the exergy analysis is substantially more useful than the energy analysis. Furthering this study, Rosen *et al*. (2000) examine an industrial sized encapsulated ice TES unit during full charging, discharging and storage cycles. The results indicate that in addition to energy analyses being incomplete for cold TES, they also achieve misleadingly high efficiency values. For the system in question, the overall energy efficiency was 99.5%, while the exergy efficiency was calculated to be 50.9%. This solidifies the fact that exergy analyses allow for a more complete diagnostic of cold TES systems and the locations of their shortfalls.

## 3.2.0 PCM Materials

The storage of thermal energy depends heavily on the medium on which it is stored. To fully utilize the latent heat release during melting (discharge period), a PCM must meet both the desired melting point and latent heat requirements of the system. For example, a solar collector charging a hot water latent TES system would not use water/ice as the PCM, since water is already in the liquid state at room temperature. Likewise, one could not use heavy metals such as copper or iron as a PCM, since the melting temperature is much too high, and would not be reachable in a solar collector. It is for this reason why a

great number of PCM materials have been studied in the literature. For brevity, however, only paraffin waxes and water will be considered, while a brief outline of the other PCMs in use will be addressed. A detailed review of over 250 PCMs and their characteristics can be found in Sharma and Sagara (2007).

### 3.2.1 Paraffin Waxes

For thermal storage using a higher temperature source, paraffin wax is an excellent solution. In general, paraffin refers to the alkaline hydrocarbons with the formula $C_nH_{2n+2}$. Paraffin waxes refer to the solids where $n$ is between 20 and 40, and are usually a liquid at room temperature with a slightly higher melting point, making them ideal for heat storage. The advantage of these paraffin waxes is that they can be chosen to have specific melting temperatures, while still having a reasonably high latent heat. A list of some paraffin wax properties can be found in Table 3-1.

**Table 3.1: Some common paraffin wax properties.**

| Name | Chemical Formula | Melting Point (°C) | Latent Heat (kJ/kg) |
|---|---|---|---|
| n-Eicosane | $C_{20}H_{42}$ | 37 | 247 |
| n-Docosane | $C_{22}H_{46}$ | 44 | 249 |
| n-Tetracosane | $C_{24}H_{50}$ | 51 | 255 |
| n-Hexacosane | $C_{26}H_{54}$ | 56 | 257 |
| n-Octacosane | $C_{28}H_{58}$ | 61 | 255 |
| n-Triacontane | $C_{30}H_{62}$ | 65 | 252 |

Source: Modified from Sharma and Sagara (2007).

For example, Nallusamy *et al*. (2007) propose a combined sensible and latent heat TES system, integrated with a solar heat source, for heating and cooling purposes. Here, paraffin is stored in spherical capsules, using water as a heat transfer fluid. Water carries solar heat energy to the PCM capsules, while also acting as a sensible heat storage medium. The system is analyzed and compared to a conventional sensible heat storage

system, and the results indicate that the latent storage system is better for intermittent use. For applications such as hot water heating and indoor heating, this is a viable alternative.

Another interesting work regarding the use of paraffin was completed in El-Kotb *et al*. (2006). They proposed an insulated flat plate heat exchanger which contains paraffin as a PCM. The heat transfer fluid in this case is again water, which is fairly common for most paraffin systems due to its high specific heat capacity and low cost. A numerical model is built and solved, which was validated by experimental data. The advantage of such a model is that the inlet and outlet flows are closely monitored, while the heat transfer rates as well as the solid/liquid boundaries can be studied.

### 3.2.2 Water/Ice

A great majority of the cold TES storage systems include water as the storage medium. The benefits of using water as the PCM include; low cost, high specific heat, high latent heat and high volumetric heat capacity. Also, due to its non-volatility and stability, it can be used in a great number of applications: apart from encapsulated ice, a few typical applications include ice-on-coil (Lee and Jones, 1996), ice slurry systems (Wang and Kusumoto, 2001) and finned tube heat exchangers (Kayansayan and Acar, 2006). In lieu of addressing them here, these systems will be further discussed in the next section, "Latent TES Methods". However, a brief comparison of the thermophysical properties of water and some other common PCMs can be found in Table 3.2.

### 3.2.3 Others

The above list is certainly not exhausted; a number of other PCMs have been sought in order to more closely parallel the growing number of TES applications. Small variations in melting temperature and latent heat can give rise to much better system efficiencies in certain applications. As a result, a number of studies have been performed to investigate the thermal performance and characteristics of many other types of PCMs and have been recorded in the literature. For example, Sari and Kaygusuz (2002) experimentally investigate the thermal performance of a lauric acid PCM. In a vertical double-pipe

system, the solidification and melting processes were monitored, and a number of system properties were recorded, including the temperature distribution, melting and solidification times, the nature of heat transfer and the heat transfer rates. Most interestingly, it was found, among other things, that conduction dominates the heat transfer during both solidification and melting. Similar studies were performed by Sari and Kaygusuz (2002, 2005 and 2006) to determine the heat transfer characteristics of various fatty acids and paraffin waxes, and their applications to TES storage. There are indeed a host of other PCMs available for comparison, including hydrated salts and eutectic mixtures, but for the purpose of low temperature-low cost analysis, a list of some of the viable fatty acids and paraffin waxes are seen in Table 3.2, along with a few inorganic PCMs.

**Table 3.2: Some common inorganic, fatty acid and paraffin PCMs for comparison.**

| Name | Chemical Formula | Latent Heat (kJ/kg) | Melting Point (ºC) |
|---|---|---|---|
| Water | $H_2O$ | 333 | 0 |
| Sulfuric Acid | $H_2SO_4$ | 100 | 10.4 |
| Lauric Acid | $C_{12}H_{24}O_2$ | 178 | 42 – 44 |
| n-Pentacosane | $C_{25}H_{52}$ | 238 | 54 |
| Stearic Acid | $C_{18}H_{36}O_2$ | 202.5 | 69 |

## 3.3.0 Latent TES Methods

As mentioned earlier, there are a number of different ways to store thermal energy in a phase change material, depending on the application. Many important factors involving these systems include cost, simplicity of design, efficiency and environmental impact. For these reasons, four specific TES methods have proven to be more viable than others, and have been studied considerably in the literature. These include ice slurry, ice-on-coil, microencapsulated PCMs and packed bed encapsulated PCMs. The first two methods are used for only cold TES, while the others can be used for either warm or cold applications.

### 3.3.1 Ice Slurry

In general, ice slurry refers to a mixture of ice crystals and liquid. The liquid in question is usually an antifreeze solution of water and a freezing point depressant such as ethylene glycol. Wang and Kusumoto (2001) discuss a number of ice slurry TES systems, incorporating a host of ice production methods. Kasza and Hayashi (1999) present a summary of the various ice slurry storage and agglomeration techniques. However, the most widely applied ice making technology is the scraped surface process developed by Sunwell Technologies in Canada (Wang, 2001). It employs a typical vapor compression refrigeration cycle whose evaporator is located on the outside of a tube-in-tube heat exchanger. The inner tube contains the binary antifreeze solution, which freezes on contact with the outer cylinder. A rotating scraper lifts off the ice, and the ice is then transported through the length of the heat exchanger with the heat transfer fluid, thereby increasing the ice content and cooling potential of the heat transfer fluid. A simplified schematic of the cross section of such a system is shown in Figure 3.2.

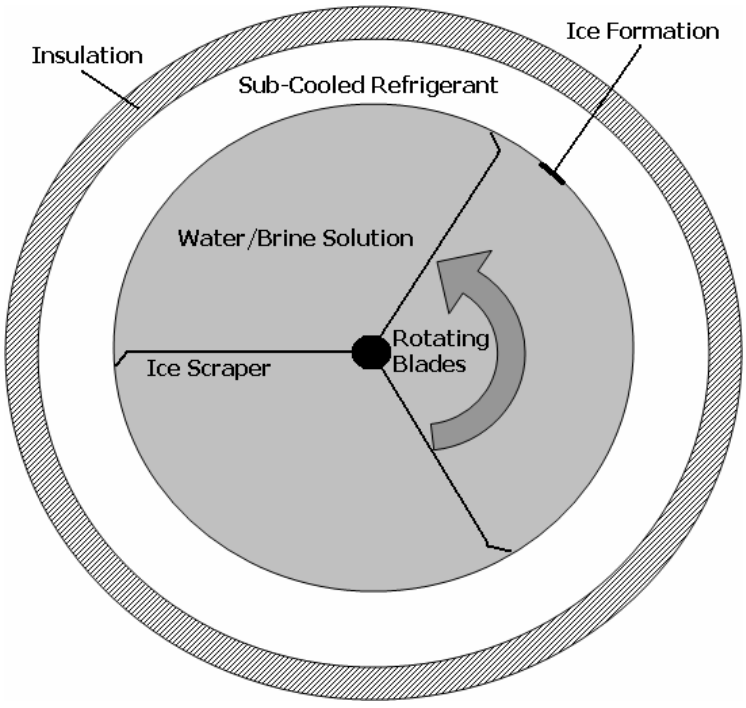


**Figure 3.2: Cross-sectional schematic of a typical ice-slurry generator.**

Many experimental studies in the literature have also been conducted concerning different methods for ice production in slurries. Matsumoto *et al*. (2004) discuss a system where an oil-water mixture is cooled while stirring, creating ice crystals of less

than 3.5 mm diameters. Performance tests were carried out to determine the effects of cooling rate and stirring wing diameter on the size and rate of ice crystal production. Yamada *et al*. (2002) propose an oscillatory rotating cooled tube method to generate ice crystals. Briefly stated, the tube is cooled by a refrigeration cycle, and immersed in a glycol solution. Once the solution reaches its freezing temperature, the tube begins to oscillate and the angular acceleration varies in order to expel ice crystals in the "mushy" zone; a zone where a solid matrix of crystals is mixed with interstitial liquid (Aseev and Alexandrov, 2006). Tests were performed to indicate the dependence of angular acceleration, rotation angle of oscillation and initial composition of the solution, and compared to present models, with varying success. Kozawa *et al*. (2005) propose a numerical method to predict the effects of ice content and mass flow rate on the storing characteristics of the dynamic-type system. Their model agrees well with experimental values, and is considered to be an acceptable design tool when conceptualizing systems such as these.

Though ice-slurry systems are incredibly simplistic in principle, they have the disadvantage of being very costly (Wang, 2001). This leads way to a need for other, more simplistic and cost-effective designs, including ice-on-coil systems and encapsulated (both micro and packed bed) systems, which will be discussed next.

### 3.3.2 Ice-on-Coil

Ice-on-coil systems can effectively solve some of the cost and energy density problems associated with ice storage. In fact, systems like these require very little maintenance and can be successfully operated for years. Chang and Nixon (2001) describe such a system; one which has been operating in an army camp in Arizona for over 12 years. These easy to operate, yet low cost systems typically come in two flavors; internal and external melt. Internal melt systems use a sub-cooled brine solution, most likely a refrigerant running in a vapor-compression refrigeration cycle, which runs through coils immersed in a tub of water. The coolant effectively freezes the water during charging times and during discharge periods, the ice extracts heat from the brine solution, cooling it for use in air conditioning applications. Kiatreungwattana and Krarti (2002) discuss such a system.

External melt systems employ the same procedure for freezing the water, but during discharge periods the water is used directly from the storage tanks.

Though simple in concept, the attempts to predict behavior of such systems through numerical and analytical modeling can prove difficult. Erek and Ezan (2007) undergo a numerical and experimental study of the charging process in an external melt TES system. The numerical procedure was made much simpler by considering a small section of the tank and by considering a few symmetry assumptions. The control volume approach used in this study provided good results into system dynamics, and could accurately predict the effects of HTF flow rate and inlet temperature on the cool storage characteristics of the tank. Such characteristics included heat transfer rate, total stored energy and energy efficiency. For more of a visual description of a typical external melt system used in the industry, refer to Figure 3.3, which shows the HTF coil configuration.

**Figure 3.3: An external melt ice TES system, showing the coils (Sassmore, 2008).**

Various other models, which attempt to predict system behavior and operating modes, are also in the literature. A few analytical models were developed by Lee and Jones (1996) which includes a myriad of assumptions, while Zhu and Zhang (2001) model the melting and solidification processes, accounting for density differences in

ice/water mixtures to correct heat transfer rate approximations. Ihm *et al*. (2004) have used the EnergyPlus software to simulate various systems integrated with cooling applications including ice-on-coil (both internal and external melt) as well as an ice-harvesting system. Control of these systems is addressed, as is the expected input and output predictions.

Though these systems are quite easy to operate and have low maintenance costs, the installation costs can still be quite high, and have limited large-scale applications, due to the immense network of coils which must be constructed for the storage tank. This has led ways to other means of storing the PCMs, where the heat can be stored and retrieved with relative ease and at low manufacturing and operating costs.

### 3.3.3 Microencapsulated PCMs

This broad classification of PCMs can include ice slurries, though it more typically alludes to paraffins for use in both cold and warm TES. The advantages of such systems are many; they have the low maintenance and relatively low cost attributes that ice slurry system share, but since the melting point of the paraffin family of PCMs range from -5ºC to well over 60ºC, the microencapsulated paraffin PCMs have a much wider range of applications. Other materials are possible to microencapsulate for use in these applications - for example Ozonur *et al*. (2005) use a coco fatty acid mixture – but the overwhelming amount of research in the literature is concerned with paraffin encapsulation.

The process of microencapsulating the PCM is not as simple as one would expect; for a detailed explanation of a few typical techniques, see Hawlader *et al*. (2002, 2003). Usually, the coacervation technique is used in order to encapsulate the paraffin in a gelatin-type material. The resulting microencapsulated PCMs have an increased surface area for heat transfer, and are transported through an appropriate HTF medium for more effective use. A scanning electron microscope must be used (See Figure 3.4) to view the microencapsulated PCM, since the mixture appears almost homogenous to the naked eye.

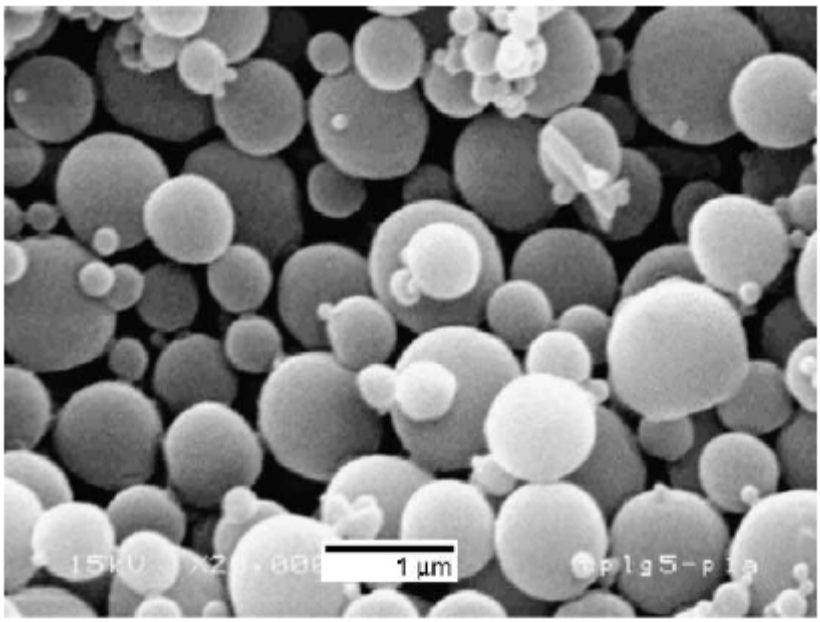


**Figure 3.4: Scanning Electron Microscope images of coacervation particles (Hawlader, 2003).**

The applications of microencapsulated systems are many, and a considerable amount of works exist [Hawlader *et al*. (2000, 2003), Xing *et al*. (2006)] which experimentally produce the microencapsulated paraffins and test them in typical TES applications. Experimental investigations into the cold (Yamagishi and Takeuchi, 1996) and warm (Yamagishi *et al*., 1999) TES applications have also been conducted, with the result that these PCM mixtures can be used in a great deal of situations. For example, Cabeza *et al*. (2007) discuss the usage of microencapsulated PCMs in concrete walls to increase energy savings and comfort levels by improving thermal inertia.

Though the applications and advantages of microencapsulated PCMs are great, there is still the drawback of its volumetric heat capacity and cost. When compared with water, (see Table 3.2) paraffin waxes have a relatively low latent heat, and are much more costly than water. So, for cold TES applications, researchers have focused more on water as a PCM than for paraffins, though there will always be lobbyists on either side. The encapsulated PCM method has gained more attention as of late, due to the low cost of its installation - they are extremely simple and can be scaled to almost any application, making them a viable option for those looking to minimize energy costs.

### 3.3.4 Packed Bed Encapsulated PCMs

In this method of encapsulation, the PCM is packed into capsules, which in turn are packed into a storage tank. A heat transfer fluid can then be run through the storage tank when heat extraction or input is desired. The simplicity in design in this case occurs where the capsules (usually spherical, but can be of any geometry) are mass-produced, and used to fill any sized storage tank to meet any cooling (or heating) load requirements. Typically, the storage tank will be of a cylindrical shape, for the following reasons: the cylinder is a relatively low-cost shape to produce which can withstand high pressures, and the surface area-to-volume ratio is lower than most other geometries, allowing for less heat penetration or leakage from the system. A simplified schematic of the system is included in Figure 3.5.


**Figure 3.5: A simplified schematic of the encapsulated ice storage tank.**

There have been a considerable amount of experimental works in the literature which analyze packed bed encapsulated TES [for example Chen *et al*. (2000)] and most of them consider the storage tank as a whole. In other words, inputs and outputs to the system (flow rate, inlet HTF temperature, void fraction, etc) are monitored to discover their effects on system efficiency, as well as charging and discharging characteristics. In addition to this, a number of numerical and analytical investigations have been undertaken to further understand the thermal phenomena which occur during charging

and discharging processes. These works can typically be divided into two classes; ones which analyze the system as a whole, as described earlier, and ones which take a much closer look at individual capsule behavior. In further understanding both the microscopic and macroscopic characteristics of encapsulated PCM systems, it is hoped that more efficient systems can be realized. The next two sections deal with the macroscopic (packed bed models) and microscopic (individual capsule) investigations, respectively.

## 3.4.0 Packed Bed Models

The wealth of information regarding packed bed investigations is immense, however most are concerned with high velocity gas flowing through a bed with particles of small diameter; for example Wen and Ding (2006) and Dekhtyar *et al*. (2002). These studies, although helpful, usually have applications in reactor beds (Yee and Kamiuto, 2002) or adsorption beds. Due to the small particle diameters, they cannot correctly analyze the important phenomena which are inherent to encapsulated packed bed TES. For these larger capsules, a number of studies have been undertaken in order to analyze thermal dispersion (Nakayama, 2005) and viscous dissipation [Lin (1981), Lee and Kamiuto (2002)]. A critical review of the thermal dispersion in various packed beds was done by Delgado (2006).

There have, also been a number of attempts to predict flow behavior and heat transfer characteristics in beds which do not consider individual capsules, most of which use the porous medium concept. The porous medium model does not require information about the capsules; rather it uses an average heat transfer coefficient between the heat transfer fluid and the PCM capsules, and from this the system can be studied using one, two or three dimensional methods. In more than one dimension, the heat transfer and fluid flow equations can become quite difficult to solve, and for this reason the numerical investigations far outweigh the analytical investigations in this field.

### 3.4.1 Analytical Studies

Investigations using analytical techniques can be used to completely solve for fluid flows and temperature distributions. However, since these techniques can be quite cumbersome to evaluate due to the overwhelming complexity in internal flow fields, a number of assumptions must be made in order to use the analytical techniques. A few such examples will be discussed here.

Yuksel *et al*. (2006) use a purely analytical approach to determine the effects of the fluid flow rate and the capsule material on the charging and solidification times. A homogenous PCM temperature was assumed, as was constant thermophysical properties and negligible heat penetration from the ambient, among other things. However, the results provide accurate predictions to the available experimental studies, despite the macroscopic visualization of the system.

Nakayama *et al*. (2001) present a two-energy equation model to account for both conduction and convection in porous media. The HTF and PCM phases, each with its own second order energy equation, are combined to form a fourth-order differential equation and various geometries and applications are then considered. This procedure employs the porous medium concept, illustrating its importance and effectiveness when evaluating complicated flows analytically. Kuznetsov (1995) undertakes a similar study, but employs the perturbation technique to investigate the temperature waves in a two-dimensional field.

For applications in solar heating, Inalli *et al*. (1996) use the monthly average solar radiation and ambient temperatures to analytically solve for temperatures in a spherical, underground storage tank. This model is then used to demonstrate the importance of seasonal solar energy storage in ground systems.

Laguerre *et al*. (2008) present an elegant analytical technique to simulate flow in a packed bed of spheres. The method, which includes porous medium concepts, takes into consideration fluid-to-capsule convection, conduction and radiation, as well as one-dimensional radial conduction inside particles. They achieve good results when compared to numerical and experimental data when a free-convection heat transfer configuration is employed.

MacPhee and Dincer (2008) propose another porous medium concept packed bed model, this one accounting for heat penetration from the ambient. A cylindrical storage tank is packed with spherical capsules, and using the integral approach assuming a linear transverse temperature profile, a HTF temperature profile is obtained. The resulting energy and exergy efficiencies, along with the exergy destructions, are evaluated, when the flow rates and inlet temperatures are varied during charging. It was found that when using larger flow rates and inlet temperatures close to that of the solidification temperature, the exergy efficiency was maximized and the destroyed exergy was minimized.

Though analytical investigations are often helpful, they become increasingly difficult when looking at extremely complicated flows in three dimensions. This has led the way to more and more numerical investigations, which utilize the powerful computing machines and algorithms developed over the years.

### 3.4.2 Numerical Studies

Numerous experimental investigations regarding packed bed flows have been conducted over the years [for example Singh *et al*. (2006), Bedecarrats *et al*. (1996), Mousavi *et al*. (2006) and Chen and Lin (1997)] to determine the effects of flow rate, void fraction and capsule geometry on the overall performance of packed bed latent TES, but it is usually much easier and cost effective to consider a numerical investigation to simulate flow and heat transfer phenomena. This is because the flow or temperature fields do not need to be solved a priori; the temperature and flow fields are simplified into a finite number of nodes or volumes and relations between them are approximated.

Some of the works in the literature are concerned with modeling existing systems, such as the one presented by Kerslake and Ibrahim (1990). Here, a two-dimensional axisymmetric model is used to discuss the role of free convection on the heat transfer performance of the TES storage tank.

Of the many numerical procedures available in the current literature concerning packed bed, encapsulated TES, most are concerned with warm TES in paraffin waxes. Zukowski (2006) analyses the heat transfer characteristics in a ventilation duct filled with encapsulated paraffin wax in rectangular configurations. They consider a three-

dimensional transient model, which is then used to predict the effect of capsule geometry and configuration on heat storage. It was also found that introducing parallel connectors downstream from the inlet could greatly assist in making the heat storage or retrieval more uniform. Benmansour (2006) provide a two-dimensional transient analysis of a cylindrical storage tank filled with uniformly sized spherical capsules. The paraffin wax in the randomly packed capsules exchanges heat with air, acting as a heat transfer fluid, and the resulting model is found to agree favorably with expected results.

Kouskosou *et al*. (2005) propose a two-dimensional approach to solve for the temperature field in a cylindrical container containing spherical capsules used for ice storage. The porous medium model was used, and along with Churchill (1983), who proposed the average Nusselt number for such flows, the entire charging and discharging processes could be evaluated. Density variations within the HTF were considered, and the system was run in both the vertical and horizontal positions. It was determined that the optimal case occurred with the tank in the vertical position, when the natural convective currents coincide with forced convection currents.

Though both the numerical and analytical techniques are sufficient when analyzing charging and discharging rates when compared to existing systems (usually, a packed bed of spheres), they do not sufficiently describe the inner flow networks and thus, comparisons of various capsule sizes, configurations and orientations cannot be accurately assessed, which has led the way to a more microscopic assessment of the individual capsules.

## 3.5.0 Single Capsule Analyses

There are many works in the literature which analyze solidification and melting in various geometries. These works typically come in one of three formats; experimental, analytical or numerical investigations.

### 3.5.1 Experimental Studies

Typically, experimental investigations into single capsule dynamics involve a capsule suspended in a fluid, exposed to a working heat transfer fluid. Ettouney *et al*. (2005)

investigate copper spheres exposed to air as a HTF. Four different diameters of capsule, each with slightly different thicknesses, were exposed to warm air to melt the enclosed paraffin, and cool air to solidify it. Thermocouples were placed in strategic locations about the PCM, so that the temperature distributions could be assessed. Nussult correlations between melting and solidification were also discovered, as were the solid/liquid interfaces. Chan *et al*. (2006) present a similar study, but instead of a cross flow HTF, a constant surface temperature is used. Initial superheat and wall temperatures are varied in order to determine the effects on the solidification of the n-hexadecane, which is used as the PCM in the spherical capsule. It was found, naturally, that with the constant wall temperature, the solidification/melting fronts propagate uniformly toward and away from the center during charging and discharging, respectively.

Eames (2002) and Adref (2002), present very similar experiments to determine the characteristics of freezing and melting of water in glass spheres. A glycol solution is used as the heat transfer fluid, and the purpose of the study is to investigate the solid/liquid interface during this process. A simple equation was also developed to describe discharging and charging rates.

A series of experiments was performed by Cho and Choi (2000) to determine the thermal characteristics of multiple paraffins, their mixtures, and water as a phase change material for latent encapsulated TES. They constructed a full bed of spherical capsules, and monitored various capsules during solidification and melting periods. The effect of bed placement, inlet temperature, inlet flow velocity and initial temperature was studied to determine their effects on solidification and melting times.

The above experimental works, although helpful when looking qualitatively at latent encapsulated TES systems, have a few drawbacks: they are of high cost (relative to computational costs in numerical and analytical techniques) and they do not allow for a global knowledge of the temperature and flow fields. This is why the following analytical and numerical techniques have been undertaken in order to more fully understand the latent aspects of TES at the capsule level.

### 3.5.2 Numerical Studies

Although a great deal of information can be learned from analytical studies of the solidification process in capsules, there is not a great deal of recent growth in this field. This is most likely due to the increasing availability of cheap computing power, coupled with the development of new, more sophisticated algorithms used for convergence of the energy and momentum equations with higher efficiency. Although there are a few instances where analytical solutions are reasonable [Barba and Spiga (2003), Lamberg and Siren (2003)], the overwhelming amount of current research is directed into numerical modeling; usually using either the finite difference or the finite volume model. Briefly explained, in both cases, the computational domain is divided into sections, called "cells" or "nodes", and flow or temperature data can be stored in these sections. The finite difference model uses approximations across the nodes, or points in the domain, while the finite volume model uses different approximations across surfaces joining adjacent cells. These two techniques have been used almost extensively in the literature, and there are a host of works which will be examined.

Zhang *et al*. (2001) consider a general model, which can be applied with varying success to all geometries. If the convective heat transfer coefficient is known, and all thermophysical properties remain constant, among other more minor assumptions, then this model may be used to find the instantaneous temperature distributions, heat transfer rates and thermal storage capacity of the system. The model was validated by experimental data using a spherical capsule, but it can be applied to many other geometries. Ismail *et al*. (2003) propose a finite difference method to simulate the solidification of water in a spherical capsule. A moving grid scheme is used – one where the computational cells can change locations transiently – to enhance the accuracy of the algorithm. The effects of shell size, as well as PCM internal and exterior temperatures are studied as related to liquid fraction and solidification times. The natural convection correlation by Churchill (1983) is also used as a heat transfer correlation.

Other geometries besides spheres have been considered for numerical analysis. De Souza and Vielmo (2005) investigate the freezing and melting of water in the interior of tubes. This analysis is applicable to cylindrical capsule geometries, as it accounts for natural convection and density changes during phase change. Wei *et al*. (2005) provide

numerical and experimental simulations for each of the spherical, cylindrical, plate and tube geometries, using the finite volume approach. The capsules in this case are constructed of stainless steel, and contain a paraffin wax, are packed into a bed-like geometry and are exposed to a cross-flow heat transfer fluid. The model achieves good results with the experimental results when looking at heat transfer rates.

Many other similar works exist for numerical simulations; a cylinder, containing paraffin, is exposed to natural convection and solved with the finite difference model in Regin *et al* (2006). Bilir and Ilken (2005) use the control volume approach for the solidification of spherical and cylindrical capsules, while Casano and Piva (2002) provide numerical and experimental data for slab geometries exposed to periodic heating. In both cases, a control volume approach is used, and the results agree well with the experiments.

Some studies rely on commercially available computer algorithms to solve numerically for fluid flows, temperature distributions and so on. These codes have the advantages that they use algorithms and solution procedures which have been proven to be more efficient and faster than most other codes. As a result, more complicated and realistic problems can be undertaken with greater accuracy than ever before. Where most codes rely on many assumptions to simplify the problem, commercial codes can solve almost any heat transfer and/or fluid mechanics simulation, given a sufficient amount of computing power and time.

Pinelli and Piva (2003) use the FLUENT software (a computational heat transfer and fluid mechanics simulation code) to investigate a cylindrical cavity heated from above. In this study, the cylinder is in an upright position, with the top and bottom kept at temperatures higher and lower, respectively, than the solidification temperature of the PCM (n-octadecane, a paraffin wax). The sides of the cylinder have a convective heat transfer relationship with the atmosphere, and thus the boundary conditions are enough so that the numerical code can accurately solve the problem. The flow fields, temperature distributions and total energy stored are examined. Experimentally, the numerical simulation is duplicated with a heating system and cooling system controlling the upper and lower parts of the cylinder, and a Styrofoam belt across the sides. The two data sets agree with each other reasonably well in terms of the temperature distributions.

Assis *et al*. (2007) present an excellent application of the accuracy of FLUENT software when analyzing complicated flows. In this study, a sphere is monitored during melting, again with commercially available paraffin as the PCM. The outer shell of the sphere is kept at a constant temperature, warmer than the solidification temperature, and the process is monitored qualitatively and quantitatively. The change in density from solid to liquid is accounted for, as is the slight density differences in the liquid state due to temperature variations, which forces naturally convective flows. The diameters of the sphere are varied, as are the wall temperatures, and the simulation is validated in large part by visual studies of the moving solid/liquid interface as time progressed. A detailed study of the relationships of various dimensionless parameters is then conducted, and the model is tested for grid size and time step independence, with good results.

Over the years, and with the help of commercially available numerical code, the study of solidification and melting in various geometries has progressed significantly. However, computational time can get very costly when tackling more difficult problems. For example, Assis *et al*. (2007) investigate only a single sphere, with a uniform (simple) boundary condition on the wall, and the computational time to real time ratio was found to be over 300:1 – meaning that 300 seconds of computational time is required for one second of real flow time. Thus, a typical run took a few days – with an extremely powerful computer, even by today's standards.

It is for this reason that MacPhee and Dincer (2008) undertake a similar study using FLUENT 6.0 software. The model presented does not take into account the density changes and convective flows inside the PCM, but still monitors energy storage rates, PCM temperature fields and HTF temperature fields during solidification. A number of single capsule sizes, containing water as the PCM, are exposed to a glycol-based heat transfer fluid to induce solidification. The capsules, which are of spherical, cylindrical and rectangular configuration, and of varying aspect ratio, are analyzed during a complete solidification period, while the temperature fields and liquid fractions are monitored. The resulting energy efficiency, exergy efficiency and destroyed exergy are analyzed for each capsule, and the results indicate that the spherical geometry is the most efficient one. This paper stands out from others in the sense that is not only analyzes energy stored and temperature variations, but also the thermal efficiencies of the charging process.

It is hoped that the present study will further the above analysis, by considering multiple capsules with a more realistic wall condition. The results should indicate which capsule geometry is better, and for what reasons, while varying such aspects as inlet HTF flow rate, temperature and dead-state temperatures.

# 4.0 Analysis

In this chapter, the problem specifications, including the assumptions used in the analysis, are outlined. The heat transfer and fluid flow equations and analysis are addressed, which include the differential equations and boundary conditions needed to solve the problems. Afterwards, an overview of the complex solution techniques that FLUENT 6.0 uses to solve this transient problem is considered. Once this groundwork has been laid, a thermodynamic analysis of the system in both the energy and exergy sense will be introduced.

However, before continuing on to the results of the simulations, the domain descriptions, including the finite volume grids, are presented. Lastly, the domains used in this study must pass a number of independence tests including grid size, time step and far-field boundary conditions, in order to be considered a reasonable computational model. The notion of grid orientation independence, though important in all numerical simulations, will not be considered in this thesis, due to the structured grids inherent in GAMBIT software. Since the grids obtained by using this software are inherently irregular, the grid density changes used to validate the grid size independence will suffice to prove grid orientation independence as well.

## 4.1 Problem Specification

Before specifying the intrinsic aspects of the simulations, it is necessary to define the scope of the present study. In most encapsulated ice storage tanks, the capsules are either of the spherical, cylindrical or rectangular (slab) geometry. The spherical geometry is far more common in industrial applications, due to its ease of manufacturing and the random assortment which can be achieved in a storage tank, eliminating the need for an internal structure to orient the capsules with the heat transfer fluid. There are other geometries which have been used, but for the purpose of this analysis, only the spherical, slab and cylindrical capsules are considered. For a better understanding of the storage tank and capsule relationship for the three geometries, see Figure 4.1.

a)

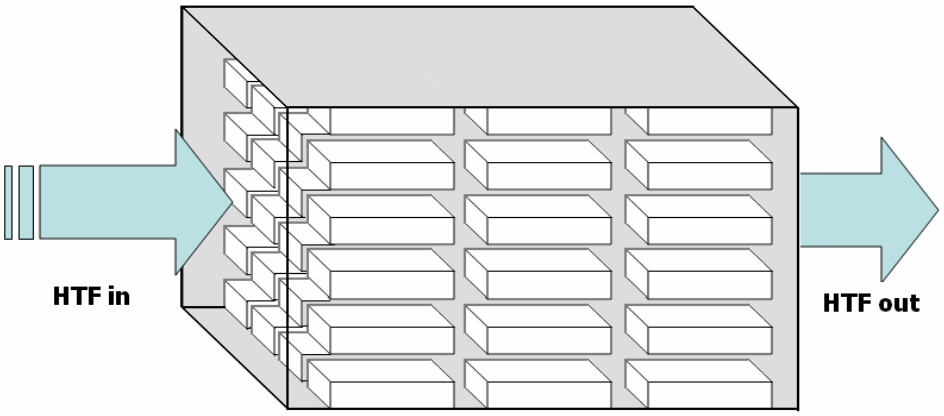


b)

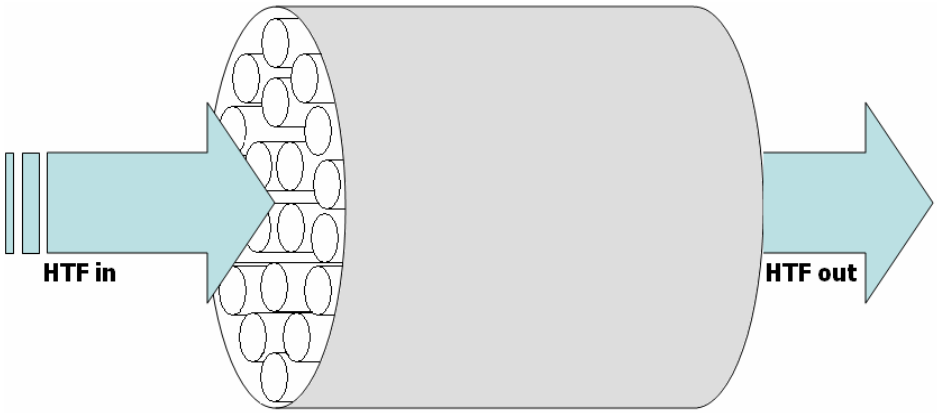


c)

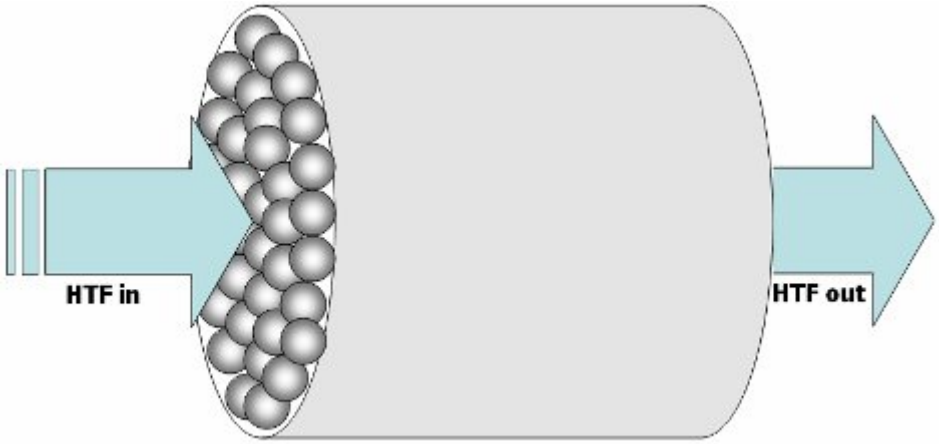


**Figure 4.1: Storage tank schematic for: a) slab capsules b) cylindrical capsules c) spherical capsules.**

The present analysis will consider one capsule of each type, and simulate its solidification and melting processes when positioned in a bed of similar capsules. The spherical capsule will be compared to the cylindrical capsules and slab capsules of

various aspect ratios. The spherical capsule will be modeled so that it comes into contact with six other capsules, and the cylindrical capsules, four. The slab capsules will have a heat transfer fluid stream thickness equal to half the slab thickness. Each capsule will have a polyvinyl chloride (PVC) shell, with a thickness of 5mm. This material is chosen due to its durability and flexibility, and should provide a good approximation to the various plastics used for capsule shells in the industry.

Before continuing any further, the assumptions used in this analysis are as follows:

- Negligible radiation effects;
- Constant thermophysical properties for the HTF and PVC;
- Piecewise constant thermophysical properties for the PCM;
- All materials are incompressible with constant density;
- Negligible storage tank wall effect;
- Negligible heat penetration into storage tank;
- Negligible potential (gravitational) energy effects;

The material thermophysical properties used in the analysis are given in Table 4.1. The properties for water and ice are taken constant at temperatures of 275K and 269K, respectively, since this is an acceptable mean temperature at which these substances will be experiencing. The properties of the glycol solution (30% by mass) are obtained from the ASHRAE refrigeration handbook [AHRAE (1997)].

**Table 4.1: Material properties used in the analysis.**

| **Substance** | **C** $\left[\frac{J}{kg \cdot K}\right]$ | **ρ** $\left[\frac{kg}{m^3}\right]$ | **k** $\left[\frac{W}{m \cdot K}\right]$ | **μ** $\left[\frac{kg}{m \cdot s}\right]$ |
|---|---|---|---|---|
| Water (liquid) | 4200 | 1000 | 0.5576 | 0.001519 |
| Water (solid) | 2106 | 917.4 | 2.108 | N/A |
| Ethylene Glycol 30% | 3574 | 1053.1 | 0.4220 | 0.00503 |
| PVC | 900 | 1380 | 0.16 | N/A |

## 4.2.0 Heat Transfer and Fluid Flow Analysis

To correctly evaluate the complicated phenomena which will be simulated in this thesis, the heat transfer and fluid flow analysis will be divided into segments. Firstly, the governing equations will be outlined, with attention directed at the separate mediums; the heat transfer fluid, water/ice PCM and the PVC capsule shell. Next, the computational procedure used in the FLUENT 6.0 software will be explained in broad terms, and some of the processing techniques will addressed.

### 4.2.1.0 Governing Equations

The equations governing the energy and fluid flow throughout the computational grid will be divided into three sections: the heat transfer fluid (HTF), the PVC capsule shell (PVC) and the water/ice medium, or phase change material (PCM). Once all governing, initial and boundary conditions are known, the solver is able to begin solving the problem over time, and the computational procedure can be discussed in more detail. For all geometries, FLUENT and GAMBIT both use rectangular co-ordinates for their domains, meaning that all governing equations and boundary conditions are three-dimensional in the *x*, *y*, and *z* directions.

#### 4.2.1.1 Phase Change Material

Due to the aforementioned assumptions, the phase change material will be conduction-dominated and contains no flow terms. The energy equation for the phase change material is then as follows:

$$\rho_{pcm} \frac{DH_{pcm}}{Dt} = k_{pcm} \nabla^2 T \tag{4.1}$$

The substantial derivative, seen in the first term of the above equation, for any variable $\gamma$, is defined as:

$$\frac{D\gamma}{Dt} = \frac{d\gamma}{dt} + u\frac{d\gamma}{dx} + v\frac{d\gamma}{dy} + w\frac{d\gamma}{dz} \tag{4.2}$$

Here, *u*, *v*, and *w* are the *x*, *y*, and *z* components of the velocity vector.

$$\vec{V} = u\vec{i} + v\vec{j} + w\vec{k}$$

In addition, $\vec{i}$ , $\vec{j}$ and $\vec{k}$ are the unit vectors in the *x*, *y*, and *z* directions, respectively.

The *del* ($\nabla$) operator, seen in the last term of the energy equation above, is a vector quantity, though in this case due to its multiplication it becomes a scalar. Nonetheless, it is used throughout the analysis, and it is shown below:

$$\nabla = \left( \frac{\partial}{\partial x}\vec{i} + \frac{\partial}{\partial y}\vec{j} + \frac{\partial}{\partial z}\vec{k} \right) \tag{4.3}$$

Continuing on with the energy equation, it is known that a phase change will occur in this medium. Therefore, the enthalpy of the PCM, *H*, will be computed as the sum of the sensible enthalpy, *h*, and the latent heat portion, $H_l$.

$$H_{pcm} = h_{pcm} + H_l \tag{4.4}$$

Due to the assumption of constant thermophysical properties, the sensible enthalpy of the phase change material can be defined as defined as:

$$h_{pcm}(T) = h_{pcm,o} + C_{pcm}(T - T_o) \tag{4.5}$$

$h_{pcm,o}$ and $T_o$ are the arbitrary reference enthalpy value and temperature; since only the change in enthalpy is required for analysis, these values will drop out in all calculations.

There are many methods of numerically simulating the process of solidification, however FLUENT uses the enthalpy/porosity method [Voller *et al*, 1987(a,b,c)]. In lieu of a solver which produces a specific melt interface position, this method is often chosen to solve problems in more complex geometries. Instead of tracking this interface position explicitly, a quantity called the liquid fraction is solved, which computes the fraction of the cell which is in liquid form. The liquid fraction is then solved each iteration in order to correctly define the temperature field. This liquid fraction, $\beta$, is defined to vary between $\beta = 0$ if $T < T_{sf}$ (melting temperature) and $\beta = 1$ if $T > T_{sf}$. Any cells which have a liquid fraction between 0 and 1 will have a temperature of $T = T_{sf}$ and the liquid fraction will depend on the amount of latent heat stored. Once the cell has received or expelled all of its latent heat, it will continue to cool as either a solid or liquid, depending on the process.

The latent heat portion, $H_l$, will now be written in terms of the latent heat of the material, *L*, in order to continue with the governing equations.

$$H_l = \beta L \tag{4.6}$$

The PCM temperature field and liquid fraction, defined by the above equations, can only be solved once one the initial and boundary conditions are specified. The first condition is the initialization temperature; at time *t = 0* the PCM is set at a temperature of 275K for the charging processes and 271K for the discharging processes. That is,

$$T_{ini,ch} = 275K \tag{4.7}$$

$$T_{ini,dis} = 271K \tag{4.8}$$

The second condition required for the solution to proceed is the wall boundary condition, which is satisfied by the temperature condition at the PVC/PCM interface. Since there should be no discontinuities in the temperature field, the temperatures should be equal at both sides of the interface. In other words, for adjacent cells on the interface,

$$T_{pcm}\left(f \in W_{pcm}\right) = T_{pvc}\left(f \in W_{pvc}\right) \tag{4.9}$$

where *f* denotes the facet which is part of the wall, *W*, which in turn is part of the PVC/PCM interface. The wall temperatures on the facets are automatically interpolated linearly by FLUENT software.

#### 4.2.1.2 PVC Capsule Shell

The PVC capsule is a solid structure, and since the PCM density changes and gravity effects were neglected, the energy equation is similar in the PVC medium to the PCM medium. Thus, the energy equation in the PVC medium is as follows:

$$\rho_{pvc} \frac{Dh_{pvc}}{Dt} = k_{pvc} \nabla^2 T \tag{4.10}$$

Where the specific enthalpy, *h*, is defined as was done in equation (4.5). Again, in order to successfully solve the above equation, boundary conditions on both the inner and outer surfaces of the PVC are required. The inner boundary condition was already satisfied in equation (4.9); thus the outer boundary condition must now be addressed. This boundary condition is similar to the one in equation (4.9). In order to keep a more continuous temperature profile, the temperatures at the outer PVC wall and the HTF next to the PVC

wall must be equal. The result is displayed in equation (4.11) below, for adjacent cells along the PVC/HTF interface.

$$T_{pvc}\left(f \in W_{pvc}\right) = T_{htf}\left(f \in W_{htf}\right) \tag{4.11}$$

As with the PCM domain, the PVC domain will be initialized at the same temperature, so that equations (4.7) and (4.8) apply here as well.

The PVC and PCM domains now need only the heat transfer fluid temperature distributions to be fully solved; and this is done in the next section concerning the heat transfer fluid domain; which is the most complicated of all three.

#### 4.2.1.3 Heat Transfer Fluid

The heat transfer fluid will need to satisfy a number of governing equations, due to the complex flow conditions within the domain. To begin with, since there is moving fluid, the energy equation for the heat transfer fluid becomes more complex due to viscous dissipation. A number of new variables must be introduced, and the energy equation is shown below.

$$\rho_{htf}\frac{Dh_{htf}}{Dt} = \frac{Dp}{Dt} + k_{htf}\nabla^2 T + \Phi \tag{4.12}$$

The last term on the right hand side of the above equation involves viscous stresses, and is customarily called the dissipation function. By the governing assumptions, we obtain the following for the dissipation function, Φ:

$$\Phi = \mu\left[2\left(\frac{\partial u}{\partial x}\right)^2 + 2\left(\frac{\partial v}{\partial y}\right)^2 + 2\left(\frac{\partial w}{\partial z}\right)^2 + \left(\frac{\partial v}{\partial x} + \frac{\partial u}{\partial y}\right)^2 + \left(\frac{\partial w}{\partial y} + \frac{\partial v}{\partial z}\right)^2 + \left(\frac{\partial u}{\partial z} + \frac{\partial w}{\partial x}\right)^2\right] \tag{4.13}$$

This term, when inserted into the energy equation, becomes the viscous stress term. It is simply addressing the energy transformed into heat due to the shear stress in the fluid.

Since the above equation now must be solved to include pressure and velocity terms, many more equations must be introduced, along with their boundary conditions, before transient solutions can take place. Firstly, the continuity equation (otherwise

known as the conservation of mass) must be fulfilled, and since the heat transfer fluid is assumed incompressible, the continuity equation becomes:

$$\nabla \cdot \vec{V} = 0 \tag{4.14}$$

The above equation, put simply, ensures that the mass fluxes across adjacent cells are conserved. Next, the momentum equations, known as the Navier-Stokes equations, must also be conserved:

$$\rho_{htf} \frac{D\vec{V}}{Dt} = -\nabla p + \mu \nabla^2 \vec{V} \tag{4.15}$$

So, the momentum conservation equations depend primarily on the velocity vectors and pressure differential within the velocity field. The change in velocity at any point in the fluid depends on the pressure gradient at that point, $\nabla p$ as well as the viscous dampening effects, denoted by $\mu \nabla^2 \vec{v}$.

Since there are some new equations introduced here with many more variables, in order to fully solve for the flow fields there will need to be a few more initial and boundary conditions. To begin with, when the solution is initialized (i.e. at time *t = 0*), the PCM and PVC are set to the initialization temperature, which is 275K for the charging process and 271K for the discharging process.

$$T_{pcm}(t = 0) = T_{pvc}(t = 0) = T_{ini} \tag{4.16}$$

The temperature of the heat transfer fluid is then patched into the domain, so that the heat transfer fluid has a temperature equal to its inlet temperature:

$$T_{htf}(t = 0) = T_{in} \tag{4.17}$$

The velocity of the heat transfer fluid is set to zero before transient solutions, but is instantaneously switched to a specified velocity, uniform over the inlet, afterwards. Since the flow direction is in the *z*-direction, these conditions are expressed as:

$$V(t = 0) = 0 \tag{4.18}$$

$$V_{in}(t > 0) = w_{in} \tag{4.19}$$

For the geometries which have a non-PCM bounded wall, for example the spherical and slab capsule geometries, there will be a boundary type which can be set as a zero shear

stress wall. This is done in order to more precisely model a real-world scenario; there will be an axis of symmetry between capsule bunches, and the following attempts to model these:

$$\frac{d\vec{V}}{d\vec{n}}\left(\vec{f} \in W_{ns}\right) = 0 \tag{4.20}$$

The above equation is explained as such; for the wall facets, $\vec{f}$, which are part of the "no shear" symmetric wall points, $W_{ns}$, the derivative of the velocity with respect to the vector normal to the wall facet, $\vec{n}$, will be zero. This ensures that no viscous dissipation is encountered in these zones and is an important proponent to the solution if the flow fields are to be solved far away from the capsule tank wall. Conversely, for the wall facets not on the no shear facets (in other words, all other "real" walls), there is a no-slip condition:

$$\vec{V}\left(\vec{f} \notin W_{ns}\right) = 0 \tag{4.21}$$

So, the velocity vectors on all wall facets not in the "no slip" regime are set to zero for all cases.

For the outflow zones, there is no need to define any conditions at these boundaries, since FLUENT extrapolates the required information from the interior of the domain. There are, however, a few aspects of this boundary condition type to note before proceeding; firstly, FLUENT assumes a zero diffusion flux for all flow variables at the outlet. In other words,

$$\frac{d\gamma}{dz}\left(\vec{f} \in W_{out}\right) = 0 \tag{4.22}$$

The symbol $\gamma$ can be any of the velocity, temperature or temperature vectors, and the above equation simply states that the flow is fully developed at the outlet in the *z* direction, which is stream-wise and normal to the outlet. The reader should note that the accuracy of the above assumption is entirely dependent on the far-field boundary condition and the placement of the outlet. This is why there must be some consideration taken when building the computational zones and placing the outlet boundaries, which will be discussed in section 4.3.

The second outlet consideration which must be highlighted is the overall continuity correction. Since the continuity equation (4.14) must be conserved, the mass flow inlet and mass flow outlet must carry the same amount of mass:

$$\left[\rho\sum_{k=1}^{n} w|A_k|\right]_{inlet} = \left[\rho\sum_{k=1}^{n} w|A_k|\right]_{outlet} \tag{4.23}$$

So, the density, which is constant, multiplied by the summation of all stream-wise velocities at each facet *k*, multiplied by the area of each facet, will equal the mass flow rate at the inlet/outlet. These two values must be conserved to ensure that the continuity equation is fulfilled.

Now that the governing equations, though quite complicated, have been addressed, the computational procedure for solving these equations can be examined, as will be done in the next section.

### 4.2.2.0 Computational Procedure

The computational procedures used in FLUENT are quite complex – in fact, many Ph. D. and post-doctoral projects have dealt with developing the many algorithms used to solve the differential equations in complex fluid flow and heat transfer problems in FLUENT. It is not the intention here to claim these computational techniques as original to this thesis; rather the importance of the solution techniques and its usefulness to the present problem will be discussed here in terms which the reader should find reasonable.

To begin with, FLUENT uses a finite-volume approach to solve for domain data. The domains discussed here have been split up into a finite number of volumes (or cells) and the relationships between adjacent cells are computed over their joining faces (or facets). The actual solver used in this analysis is a pressure-based solver; since all of the materials used in this problem are assumed incompressible, the flow is governed solely by pressure differentials. In this case, the pressure-based solver employs an algorithm which belongs to a general class of methods called projection methods (Chorin, 1968). In this method, the conservation of mass, or continuity, is achieved by solving a pressure correction equation. This equation is derived from the continuity and momentum equations, outlined earlier, in such a way that the pressure/velocity field satisfies the continuity equation. Since the differential equations which must be satisfied are

nonlinear by nature, and coupled, the solution must be iterated in a closed loop until the solution converges within the required tolerances. A schematic of the solution process is included below in Figure 4.2, taken from the FLUENT 6.3 user's guide.

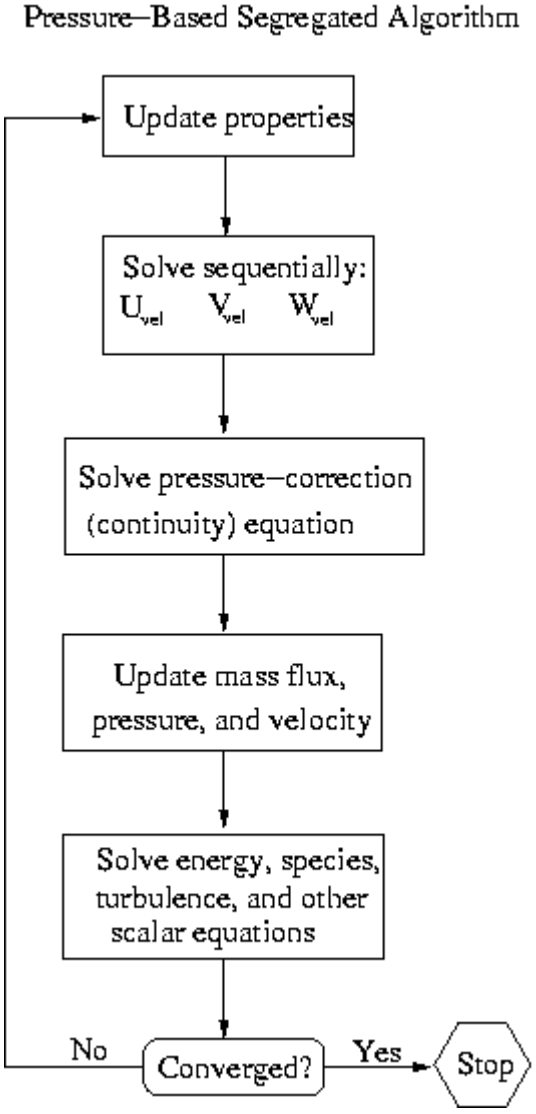


**Figure 4.2: Solution procedure flow chart for the coupled pressure based solution algorithm [Source: FLUENT 6.3 user's guide].**

The premise of the segregated pressure based algorithm is that the variables (for example, *u*, *v*, *w*, *p*, etc.) are solved sequentially (segregated). Though this is somewhat computationally tiresome, the recent advance in computer speed and memory capacity makes it an excellent choice for the problem in question. To accomplish this, a special algorithm, called the SIMPLE algorithm for pressure based segregated solvers, is used.

#### 4.2.2.1 SIMPLE Algorithm

The SIMPLE (Semi-Implicit Method for Pressure-Linked Equations) algorithm, despite its name, is far from simple to those who are not familiar with numerical analysis and discretization. This algorithm follows the basic outline of the flow diagram in Figure 4.2, but each step is somewhat more complicated. Due to the complexity of the algorithm when applied to discrete cell volumes, the general outline of the model will be discussed in lieu of supplying many complicated equations.

Before getting into the SIMPLE algorithm, it should be noted that all numerical solution techniques do not solve for flow variables *everywhere* in the flow. Rather, they use a discretization technique, which splits up the computational domain into sections. In the centroid of each cell, the pertinent information is stored, which includes velocity vectors, temperature, density, and any other properties deemed acceptable to monitor by the user or the numeric solver. However, since the governing equations, outlined in the previous section, are all continuous, they need to be *discretized* in order to be used in the numerical procedure. In other words, since the pertinent information is stored in the centroid of each cell, the mass and continuity equations, which must solve the flow field, must be applied at cell facets (walls), and not through the centroids. To do this, both the momentum and continuity equations are discretized using projected face values from the centers of adjacent cells. The Green-Gauss method is used to accomplish this.

$$\gamma_f = \frac{\gamma_{c,0} + \gamma_{c,1}}{2} \tag{4.24}$$

In other words, the face (facet) values of all variables are taken as the average of the adjoining two cells. So, in reality, all variables in the solution can be seen as piecewise-linear at any time. However, since the number of cells in the solution is quite vast compared to the total volume, the overall solution will appear continuous, not discrete, which is the overall goal of the numerical algorithm.

Now, the first step in the SIMPLE algorithm is to solve the momentum equations, sequentially, by guessing the pressure field, say $p^*$. Since the pressure field, $p^*$, is rarely guessed correctly, it will have to be re-adjusted, and the bulk proportion of this algorithm is devoted to just that. As the solution loop progresses, the algorithm updates this pressure field continuously until the solutions is achieved within tolerances.

If the pressure field, $p^*$, is not initially correct (which is most often the case), the continuity equation, which is evaluated next, is not satisfied. A correction factor is then introduced in order to correct the face fluxes, so that continuity can be achieved. The corrected face fluxes for each cell are then substituted back into the discrete continuity equation, which then produces a discrete equation for the pressure correction in each cell. The purpose of this step is to solve for the pressure correction equation, and it is achieved by solving this discrete pressure correction equation using the algebraic multigrid method (AMG). While the intrinsic nature of this method will not be discussed due to its complexity, it should be noted that it was chosen due to the fact that it does not depend on the problem geometry whatsoever, and as such can be used for more complicated problems like the ones presented here.

Once the pressure correction equation has been solved, it is used, along with a host of under-relaxation factors, which can be defined by the user, to correct all cell pressure values and face fluxes.

The next to last step in the algorithm is to use the corrected continuity and momentum equations to solve the energy equations, which are important in any heat transfer application. Once these energy equations, which differ from zone to zone, are solved, the last step in the algorithm checks the residual error of the conservation equations.

The residual error is simply the total summed differences in the governing equations from cell to cell. Since the cells in the computational domain cannot possibly solve the equations with infinite precision, there will always be errors when updating solutions. So, in this case, the error for each of the $x$, $y$, and $z$ velocities, along with the continuity and energy equation errors are summed separately over the domain. If the result is below tolerance, the solution is converged. If the result is above the convergence criteria, the solution is not converged. In this case the corrected pressure field becomes the new guessed pressure field $p^*$, in the first step of the algorithm, and the whole process repeats itself iteratively.

It should be noted that the residual values are dependent on the scale of the problem. For example, a rather large system, with many computational domains and a fast moving flow, would have a much larger residual error than say a very small system

with very little flow. If the total residual error tolerance is the same in both cases, the simpler problem would lose much more information per cell on these differences. This is why the residual values are actually a scaled value, based on the cell values themselves. A simplification of the residual can be seen below, for any flow parameter $\gamma$ in a computational domain of $n$ cells:

$$\mathrm{Re}\, s^{\gamma} = \sum_{i=i}^{n} \frac{\gamma_{in} - \gamma_{out} - \gamma_{source}}{\gamma_{in}} \tag{4.25}$$

In other words, the scaled residual for each variable is simply the difference between the inlet and outlet flows, minus the source term, divided by the flow in. These flow terms are applicable to the momentum, continuity and energy equations, while the source term is most applicable to the energy equation, since energy values of cell change with time. This allows for a more complete residual tolerance selection, which is scalable to all problems of computational fluid dynamics and heat transfer.

For the problem in question, the residual tolerances for the $x$, $y$, and $z$ velocity values, as well as the overall continuity equation, were set at $1e^{-3}$. For the energy equation, the tolerances were set at $1e^{-6}$.

#### 4.2.2.2 Numerical Solution

Once the solution is attained at each time step, certain monitors can be put in place to track system parameters as time progresses. Such parameters include inlet and outlet pressures, velocities, temperatures, liquid fractions, as well as average volumetric temperatures within the zones. After careful consideration of the gradients these values attain transiently, it was decided that the cell parameters should be written to files at most every 0.5 seconds. This ensured that most of the required information could be captured, while keeping the solution as time efficient as possible.

For all capsule geometries, the time steps and grid sizes were chosen to find a suitable agreement between solution precision and computational effort. If an infinitely powerful computer was available, each cell volume would be infinitesimally small, and the solution could converge to a tolerance of zero. However, since this is not possible, a middle ground must be attained where the computational time is reduced, while still

retaining most of the information in the computational domain. The grid size and time step independences, which are very important when studying computational heat transfer and fluid mechanics, are discussed in detail in sections 4.5 – 4.7.

The solutions obtained in this study were done so using 20 hp workstation xw8000 computers in a computing laboratory at UOIT. Each workstation computer featured one 3.20 GHz Intel Xeon processor, equipped with 4.0 Gb of PC2100 DDR SD RAM. Though these computers are quite powerful, the computational times for the various trials were considerable, and can be seen in Table 4.2 for all geometries.

**Table 4.2: Computational times for flow simulations in each geometry.**

| Geometry | Computational time for 1 s of flow time (s) | Total simulation time for geometry (s) |
|---|---|---|
| Sphere | 15.4 | 680,000 |
| Cylinder, AR2 | 5.5 | 245,000 |
| Cylinder, AR5 | 6.5 | 197,000 |
| Cylinder, AR8 | 12.7 | 307,000 |
| Slab, AR2 | 6.2 | 325,000 |
| Slab, AR5 | 13.3 | 270,000 |
| Slab, AR8 | 12.6 | 341,000 |

In inspection of Table 4.2, it can be inferred that the spherical geometry was by far the most computationally tiresome to evaluate. This is most likely due to the small time step required. And, since the flow field in the spherical geometry is the most complicated, it is not surprising that the computational times are quite high.

Even though the simulations were run on 20 separate computers, the actual time required to obtain solutions was still quite high, at around 33 hours per computer. However, this represents only a portion of the overall simulation time, since the majority of computing time was spent trying to determine the optimal grid sizes and time steps for the computational domain. With this in mind, the computational time was more likely around 70 hours per computer, with an overall computational time of over 50 days if completed on a single computer.

Before continuing on to the grid size, time step and far-field independence, the solution monitors which were in place for the duration of the simulations should be addressed.

Though the inlet and outlet extended flow channels are interesting from a fluid mechanics perspective, they are unattractive when using thermodynamic analyses, as is done in section 4.3. The reason for the extended channels is to negate the effects of a lengthened flow channel on solution progress, and since this is shown to be true in section 4.7, the area under analysis can be simplified to the flow channel just before and just after the capsule area. To do this, two virtual surfaces were created, and placed at the inlet and outlets to the capsule areas. This creates a control volume which is just large enough to contain the capsules, along with the adjacent flowing heat transfer fluid, which can be used in the thermodynamic analysis. For a more detailed explanation of the thermodynamic analysis, please see section 4.3.

Once this control volume was created, it was noticed that all thermodynamic information could be ascertained by monitoring 5 separate items: the average temperature of the HTV, PVC and PCM, as well as the inlet and outlet average pressures. It is not so easy to simply create a monitor which tracks the above items, so great care was taken to ensure the correct values were met. For the average temperature $\overline{T}$ in any of the HTF, PCM or PVC mediums, the values were met by performing a volume weighted average over the zone which the medium was contained. This is a valid technique, since all materials are assumed incompressible and have constant specific heats. The average temperature in any volume made up of *n* cells is then:

$$\overline{T} = \frac{1}{V}\int T dV = \frac{1}{V}\sum_{i=1}^{n} T_i |V_i| \tag{4.26}$$

So, the average temperature is attained by multiplying the temperature and volume of each cell, summing these values over the volume of *n* cells, and dividing by the overall cell volume.

Though the calculations for the average temperatures of the various zones are quite simplistic in nature, it is much more difficult to evaluate the inlet and outlet average pressure values, due to variations in velocity over the flow field. For example, if an area-weighted average was taken, the cells in the domain which carry very little mass flow rate

(and thus, very little pressure energy) would have the same effect on the average pressure as the cells which carry a large amount of pressure energy. This is not the correct procedure when determining average pressure drop along a duct, which is why the mass-weighted average pressure was monitored.

In essence the mass weighted average pressure is obtained by taking the density of each cell which flows into the surface boundary, and multiplying this by the absolute dot product of the facet area vector and the velocity vector. This gives the mass flux entering the surface. When the mass flux is multiplied by the pressure at the adjoining cells, and summed over the *n* cells which are adjacent to the surface, and divided by the total mass flux entering the surface, the mass weighted average pressure is obtained:

$$P = \frac{\sum_{i=1}^{n} P_i \rho_i \left| \vec{V} \cdot \vec{A} \right|}{\sum_{i=1}^{n} \rho_i \left| \vec{V} \cdot \vec{A} \right|} \tag{4.27}$$

This ensures that the correct average pressure drop along the flow duct can be used in calculations.

The average pressure drop monitors, along with the volume averaged temperatures of the three mediums are paramount to the thermodynamic analysis of the numerical solutions, and the thermodynamic analysis is next to follow.

## 4.3.0 Thermodynamic Analysis

In addition to the heat transfer and fluid flow computational analyses, the thermodynamic aspects of the solidification and melting processes must be examined. Thermodynamic analyses are very helpful in determining system performance, including efficiency values and losses. In addition to the mass balance equations, introduced in section 4.2 as the continuity equation, there are two main criteria usually used for thermal analysis. These are the exergy and energy analyses, and will be introduced and discussed next.

### 4.3.1 Energy Analysis

An energy balance on either the solidification or melting process results in the following:

$$\Delta E_{sys} = E_{in} - E_{out} \tag{4.28}$$

In other words, the total energy change in the computational domain during the entire process must balance the difference between the inlet and outlet energy flows. This is known as the conservation of energy principle, or the first law of thermodynamics. By the assumptions of negligible kinetic and potential effects, as well as constant densities, the flow energy difference can be re-written as follows:

$$E_{in} - E_{out} = U_{in} - U_{out} = H_{in} - H_{out} + V\left(P_{in} - P_{out}\right) \tag{4.29}$$

Here, $U$ denotes the internal energy, $H$ represents the enthalpy, $V$ is the total volume of the heat transfer fluid used in the process, and $P$ is the average total pressure of the heat transfer fluid.

The change in energy of the system is defined as the energy change in each of the components of the system:

$$\Delta E_{sys} = \Delta E_{htf} + \Delta E_{pcm} + \Delta E_{pvc} \tag{4.30}$$

Here, the HTF and PVC zones undergo a change in sensible enthalpy only, while the PCM undergoes a change in sensible enthalpy in both the solid and liquid phases, along with a change in enthalpy associated with phase change:

$$\Delta E_{htf} = m_{htf} C_{htf} \left(\Delta \overline{T}_{htf}\right) \tag{4.31}$$

$$\Delta E_{pvc} = m_{pvc} C_{pvc} \left(\Delta \overline{T}_{pvc}\right) \tag{4.32}$$

$$\Delta E_{pcm} = m_{pcm} \left[\pm L + C_w \left(\Delta \overline{T}_{pcm,w}\right) + C_i \left(\Delta \overline{T}_{pcm,i}\right)\right] \tag{4.33}$$

Note that the latent heat, $L$, can be positive or negative, depending on whether the process is solidification or melting.

It was noticed, during solution processing, that the computing of the enthalpy flows into and out of the capsule control volume were extremely taxing computationally, and it was decided that since all system properties could be ascertained using the above energy equations, the enthalpy flows should not be tracked. This does not in any way alter the validity of the results, since the enthalpy flows can easily be solved using the aforementioned equations.

Now that the proper energy balance equations have been addressed, it is necessary to introduce the energy efficiency; the ratio of the desired energy output to the total energy input.

$$\eta = \frac{\text{Desired Energy Output}}{\text{Total Energy Input}} = \frac{E_{des}}{E_{tot}} \tag{4.34}$$

The desired energy output for the charging process is the change in energy for the control volume, since the goal of the charging process is to store the cool energy in the control volume. Please note that even though the term "cold energy" is somewhat contradictory, all subsequent terms have been altered to give a positive value, both because it is the cold energy which is desirable, and to somewhat facilitate calculations..

$$\begin{aligned} E_{des,ch} = \quad & m_{pcm}\left[L + C_w\left(\overline{T}_{ini,pcm} - T_{sf}\right) + C_i\left(T_{sf} - \overline{T}_{f,pcm}\right)\right] \\ & + m_{pvc}C_{pvc}\left(\overline{T}_{ini,pvc} - \overline{T}_{f,pvc}\right) + m_{htf}C_{htf}\left(\overline{T}_{f,htf} - \overline{T}_{ini,htf}\right) \end{aligned} \tag{4.35}$$

Since the purpose of the discharging process is to obtain the cool energy back from the control volume, the desired energy output for the discharging process is defined as the change in enthalpy for the flows between the inlet and outlet.

$$E_{des,dis} = H_{in} - H_{out} \tag{4.36}$$

When combining equations 4.1 to 4.6, the enthalpy can be re-written in terms of the other variables, and the resulting desired energy output during the discharge process is as follows:

$$\begin{aligned} E_{des,dis} = \quad & m_{pcm}\left[L + C_w\left(\overline{T}_{f,pcm} - T_{sf}\right) + C_i\left(T_{sf} - \overline{T}_{ini,pcm}\right)\right] + V\left(P_{out} - P_{in}\right)_{dis} \\ & + m_{pvc}C_{pvc}\left(\overline{T}_{f,pvc} - \overline{T}_{ini,pvc}\right) + m_{htf}C_{htf}\left(\overline{T}_{ini,htf} - \overline{T}_{f,htf}\right) \end{aligned} \tag{4.37}$$

The total energy input is given by the required energy needed for a process to occur. For the charging process, the required energy is simply the difference between the inlet and outlet energies.

$$E_{tot,ch} = E_{in} - E_{out} \tag{4.38}$$

And, once again by using equations 4.28 to 4.33, and re-arranging, the result is as follows.

$$E_{tot,ch} = m_{pcm}\left[L + C_w\left(\overline{T}_{ini,pcm} - T_{sf}\right) + C_i\left(T_{sf} - \overline{T}_{f,pcm}\right)\right] + V\left(P_{in} - P_{out}\right)_{ch} + m_{pvc}C_{pvc}\left(\overline{T}_{f,pvc} - \overline{T}_{ini,pvc}\right) + m_{htf}C_{htf}\left(\overline{T}_{f,htf} - \overline{T}_{ini,htf}\right) \quad (4.39)$$

In the same way, the energy required in the case of discharging is the amount of cool energy stored in the control volume:

$$E_{tot,dis} = m_{pcm}\left[L + C_i\left(T_{sf} - \overline{T}_{ini,pcm}\right) + C_w\left(\overline{T}_{f,pcm} - T_{sf}\right)\right] + m_{pvc}C_{pvc}\left(\overline{T}_{f,pvc} - \overline{T}_{ini,pvc}\right) + m_{htf}C_{htf}\left(\overline{T}_{ini,htf} - \overline{T}_{f,htf}\right) \quad (4.40)$$

Now that the proper required and desired energy contents have been identified, the energy efficiencies for the charging and discharging processes can be evaluated.

$$\eta_{ch} = \frac{E_{des,ch}}{E_{tot,ch}} \times 100\% \quad (4.41)$$

$$\eta_{dis} = \frac{E_{des,dis}}{E_{tot,dis}} \times 100\% \quad (4.42)$$

### 4.3.2 Exergy Analysis

An exergy balance on any system undergoing any process is as follows:

$$\Delta\Xi_{sys} = \Xi_{in} - \Xi_{out} - \Xi_d \quad (4.43)$$

The above exergy balance is quite similar to the energy case, but it contains one extra term; the exergy destroyed term $\Xi_d$. The exergy destroyed results from irreversibilities within the system, and represent the exergy which becomes unrecoverable during the process.

As with the energy case, the exergy change in the system is a result of the exergy changes associated with each material within the system:

$$\Delta\Xi_{sys} = \Delta\Xi_{htf} + \Delta\Xi_{pvc} + \Delta\Xi_{pcm} \quad (4.44)$$

Here, the change in exergy for the HTF and the PVC are easily obtained, due to the incompressibility assumption:

$$\Delta\Xi_{htf} = m_{htf} C_{htf} \left[ \overline{T}_{f,htf} - \overline{T}_{ini,htf} - T_\infty \ln\left( \frac{\overline{T}_{f,htf}}{\overline{T}_{ini,htf}} \right) \right] \tag{4.45}$$

$$\Delta\Xi_{pvc} = m_{pvc} C_{pvc} \left[ \overline{T}_{f,pvc} - \overline{T}_{ini,pvc} - T_\infty \ln\left( \frac{\overline{T}_{f,pvc}}{\overline{T}_{ini,pvc}} \right) \right] \tag{4.46}$$

However, for the PCM, the exergy change is not as straightforward as in the energy case. Since there is both a sensible and latent exergy change within the PCM, the total change in exergy will be the sum of the exergy change in the water and ice states, which are evaluated similar to above, plus the exergy change due to the solidification of the PCM. So, for the charging and discharging states, this becomes:

$$\begin{aligned} \Delta\Xi_{pcm,ch} = \quad & m_{pcm} C_w \left[ T_{sf} - \overline{T}_{ini,pcm} - T_\infty \ln\left( \frac{T_{sf}}{\overline{T}_{ini,pcm}} \right) \right] \\ & + m_{pcm} C_i \left[ \overline{T}_{f,pcm} - T_{sf} - T_\infty \ln\left( \frac{\overline{T}_{f,pcm}}{T_{sf}} \right) \right] + m_{pcm} L \left( \left( \frac{T_\infty}{T_{sf}} \right) - 1 \right) \end{aligned} \tag{4.47}$$

$$\begin{aligned} \Delta\Xi_{pcm,dis} = \quad & m_{pcm} C_i \left[ T_{sf} - \overline{T}_{ini,pcm} - T_\infty \ln\left( \frac{T_{sf}}{\overline{T}_{ini,pcm}} \right) \right] \\ & + m_{pcm} C_w \left[ \overline{T}_{f,pcm} - T_{sf} - T_\infty \ln\left( \frac{T_{f,pcm}}{T_{sf}} \right) \right] + m_{pcm} L \left( 1 - \left( \frac{T_\infty}{T_{sf}} \right) \right) \end{aligned} \tag{4.48}$$

In the above equations, the latent exergy term was arrived at by noticing that, for any incompressible substance,

$$\Delta\Xi_{sys} = \Delta E_{sys} - T_\infty \Delta S \tag{4.49}$$

And, the change in entropy for the solidification process is determined by the *entropy of fusion* equation:

$$\Delta S_{fus} = m_{pcm} \frac{L}{T_{sf}} \tag{4.50}$$

So, by using the above two equations, the exergy change in equations 4.47 and 4.48 can be calculated.

Now that the system energy change over the process has been evaluated, the inlet, outlet and destroyed exergy terms must be addressed. Before continuing, please note that since it was noticed that the problem was made very much easier computationally by monitoring the exergy destroyed, as is done next. Once the exergy destroyed has been evaluated, the exergy flow difference is easily solved. The destroyed exergy equation is as follows:

$$\Xi_d = T_\infty S_{gen} \tag{4.51}$$

As mentioned earlier, this is a result of irreversibilities or losses within the system. Since the exergy destroyed depends on the entropy generation, an entropy balance must now be performed on the system:

$$\Delta S_{sys} = S_{in} - S_{out} + S_{gen} \tag{4.52}$$

The entropy, *S*, is a measurement of the degree of randomness of a substance. It is always increasing due to irreversibilities in the system. This is a corollary of the second law of thermodynamics. However, if the system is taken as the capsule region *plus* the total amount of HTF, and since there is no heat loss to/from the system, the generated entropy occurs as a result of two separate phenomena; viscous dissipation losses, and entropy generation from heat transfer to the capsules.

$$S_{gen} = S_{gen,diss} + S_{gen,trans} \tag{4.53}$$

The entropy generated from viscous dissipation (from Sahin, 1999) will depend on the bulk fluid temperature of the HTF, the total mass of heat transfer fluid in the process, and the average pressure drop within the HTF:

$$S_{gen,diss} = \frac{M_{htf}\left(P_{in} - P_{out}\right)}{\rho_{htf}\overline{T}_{b,htf}} \tag{4.54}$$

Here, the bulk heat transfer fluid temperature $\overline{T}_{b,htf}$ is the temperature at which viscous heat is added to the flow. It is estimated to be the average between the initial and final states. Since the heat transfer fluid, on average, does not undergo a large temperature change, this assumption should be regarded as accurate to within at least a few hundredths of a percentile:

$$\overline{T}_{b,htf} = \frac{\overline{T}_{ini,htf} + \overline{T}_{f,htf}}{2} \tag{4.55}$$

In addition to the viscous dissipation, entropy is also generated from heat transfer to the capsules. The equation for this mode of generation is given by the summation of all entropy changes within the insulated system, which arises as a result of pure heat transfer (and not viscous dissipation):

$$S_{gen,trans} = M_{htf} C_{htf} \ln\left(\frac{T_{in} + \Delta T}{T_{in}}\right) + \Delta S_{pvc} + \Delta S_{pcm} \tag{4.56}$$

where $\Delta T$ is the change in temperature which is brought about by heat transfer which changes the total system energy:

$$\Delta T = \frac{\Delta E_{sys}}{M_{htf} C_{htf}} \tag{4.57}$$

and $\Delta S$, for both the PVC and PVC, is the change in entropy of each medium:

$$\Delta S_{pvc} = m_{pvc} C_{pvc} \ln\left(\frac{\overline{T}_{f,pvc}}{\overline{T}_{ini,pvc}}\right) \tag{4.58}$$

$$\Delta S_{pcm,ch} = m_{pcm}\left[\frac{L}{T_{sf}} + C_w \ln\left(\frac{\overline{T}_{ini,pcm}}{T_{sf}}\right) + C_i \ln\left(\frac{T_{sf}}{\overline{T}_{f,pcm}}\right)\right] \tag{4.59}$$

$$\Delta S_{pcm,dis} = m_{pcm}\left[-\frac{L}{T_{sf}} + C_i \ln\left(\frac{\overline{T}_{ini,pcm}}{T_{sf}}\right) + C_w \ln\left(\frac{T_{sf}}{\overline{T}_{f,pcm}}\right)\right] \tag{4.60}$$

So, the above equations, in conjunction with equation 4.51, finally allow the destroyed exergy to be calculated. However, in equations 4.56 and 4.54, the total mass of heat transfer must now be evaluated. To do this, the overall solidification time for each process $\Delta t$ must be multiplied by the mass flow rate of the entering heat transfer fluid. Since the inlet velocity of the fluid is specified, the total mass of heat transfer fluid used in each trial is very easily calculated under the constant density assumption:

$$M_{htf} = \rho_{htf} V_{in} A_{cross} \Delta t \tag{4.61}$$

Here, $A_{cross}$ is the cross-sectional area of the inlet.

The exergy balance equation can now be solved in full. The intention for the current analysis is to define the exergy efficiency, which is similar to the energy case, and it is given as follows:

$$\psi = \frac{\text{Desired Exergy Output}}{\text{Total Exergy Input}} = \frac{\Xi_{des}}{\Xi_{tot}} \tag{4.62}$$

So, once again, the exergy efficiency for either process is simply the ratio of the desired exergy output to the required exergy input. The desired and total required exergy contents for both the charging and discharging processes are analogous to the energy case, and are listed next. To avoid duplication; these equations will depend on the equations already outlined in this section.

$$\Xi_{des,ch} = \Delta\Xi_{htf} + \Delta\Xi_{pcm,ch} + \Delta\Xi_{pvc} \tag{4.63}$$

$$\Xi_{des,dis} = \Delta\Xi_{htf} + \Delta\Xi_{pcm,dis} + \Delta\Xi_{pvc} - \Xi_{d} \tag{4.64}$$

$$\Xi_{tot,ch} = \Delta\Xi_{htf} + \Delta\Xi_{pcm,ch} + \Delta\Xi_{pvc} + \Xi_{d} \tag{4.65}$$

$$\Xi_{tot,dis} = \Delta\Xi_{htf} + \Delta\Xi_{pcm,dis} + \Delta\Xi_{pvc} \tag{4.66}$$

So, finally, the exergy efficiencies for both the charging and discharging processes can be evaluated, and depend on the host of equations set forth previously in this analysis:

$$\psi_{ch} = \frac{\Xi_{des,ch}}{\Xi_{tot,ch}} \times 100\% \tag{4.67}$$

$$\psi_{dis} = \frac{\Xi_{des,dis}}{\Xi_{tot,dis}} \times 100\% \tag{4.68}$$

After analyzing the systems, however, it became apparent that the energy efficiencies were very high, all of which being over 99% efficient. While these phenomena will be addressed in the discussion of the results, it should be noted that a more readily observable, normalized energy efficiency will be put forth, which will make it easier to inspect the efficiency ranges from 99% to 100%. This normalized energy efficiency is defined as follows:

$$\overline{\eta} = \left( \frac{\eta - 99}{0.01} \right) \tag{4.69}$$

where $\eta$ refers to the energy or exergy efficiencies in either the charging or the discharging processes. This will greatly help in the presentation of the results in later sections.

Now that the thermodynamic analysis of the system have been attended to, the charge for the remainder of the analysis is to see what effect the inlet heat transfer

velocity and temperature, capsule geometry, as well as the dead-state temperature have on the following system performance criteria:

- solidification and melting times
- energy efficiency
- exergy efficiency
- exergy destruction

However, before these criteria can be calculated, the various cases studied must be outlined, including the domain descriptions and grid structuring procedures for each.

### 4.4.0 Domain Descriptions

The capsules which will be considered here will be of spherical, cylindrical and slab shape, and each will contain an equal amount of phase change material. For the cases investigated here, the volume is set at 268.1 $cm^3$, a value which was chosen to be quite close to capsule sizes used in the industry today (Cristopia, 2003). In addition to this, each capsule will be enclosed by a PVC shell with wall thickness 0.5cm. This is again chosen to be close to the industry standard, though most companies keep shell material and dimensions a secret.

The capsules will then be tested according to aspect ratio. For the spherical capsules, this point is moot, but for the cylindrical and rectangular capsules, the aspect ratios are defined as:

$$AR_c = Le_c / D_c \tag{4.70}$$

$$AR_S = Le_S / Ht_S \tag{4.71}$$

So, for the cylindrical capsules, the aspect ratio is defined as the (stream-wise) length to diameter ratio. Likewise, for the slab capsule, the aspect ratio is defined as the (stream-wise) length to thickness ratio. For the slab capsule, the cross-stream length is assumed to be equal to the stream-wise length, so the slab capsules are essentially a square-topped capsule with side length $Le_S$ and thickness $Ht_S$. Note that for all geometries, the aspect ratios are defined according to the inner boundaries of the PVC, not the outer.

The spherical capsules can now be compared to the cylindrical and rectangular capsules, with the latter two varying the aspect ratio from 2 to 5 to 8. Therefore, there are

7 separate geometries to be investigated, and the dimensions of all capsules can be found below in Table 4.3.

**Table 4.3: Geometric dimensions - note that "AR" denotes aspect ratio.**

| | **Sphere** | | |
|---|---|---|---|
| **Inner Radius** ($R_i$) [cm] | 4.0 cm | | |
| **Outer Radius** ($R_o$) [cm] | 4.5 cm | | |
| | **Slab** | | |
| | AR2 | AR5 | AR8 |
| **Length** ($Le_s$) [cm] | 8.124 cm | 11.025 cm | 1.612 cm |
| **Inner Height** ($Ht_{s,i}$) [cm] | 4.062 cm | 2.205 cm | 12.896 cm |
| **Outer Height** ($Ht_{s,o}$) [cm] | 5.062 cm | 3.205 cm | 13.896 cm |
| | **Cylinder** | | |
| | AR2 | AR5 | AR8 |
| **Length** ($Le_c$) [cm] | 11.094 cm | 20.435 cm | 27.952 cm |
| **Inner Diameter** ($D_i$) [cm] | 5.547 cm | 4.087 cm | 3.494 cm |
| **Outer Diameter** ($D_o$) [cm] | 6.547 cm | 5.087 cm | 4.494 cm |

Now that the physical characteristics of each capsule have been outlined, the computational domains can be addressed next, starting with the spherical geometry.

### 4.4.1 Spherical Capsules

The spherical capsule domain, as seen in Figure 4.3, will be defined as a square cylinder, containing parts of four adjacent and touching PCM capsules. This is done to more correctly model the interactions between spheres stacked in a large storage tank. The eight corners of the square cylinder will be located at the centers of eight far-field capsules to ensure far-field considerations are minimal. In other words, the outer shells of extra capsules are added in order to more correctly simulate the flow field and to achieve a semi-developed flow. So, the velocity inlet will be located at the space between adjacent capsules as seen below. The velocity outlet is analogously defined.

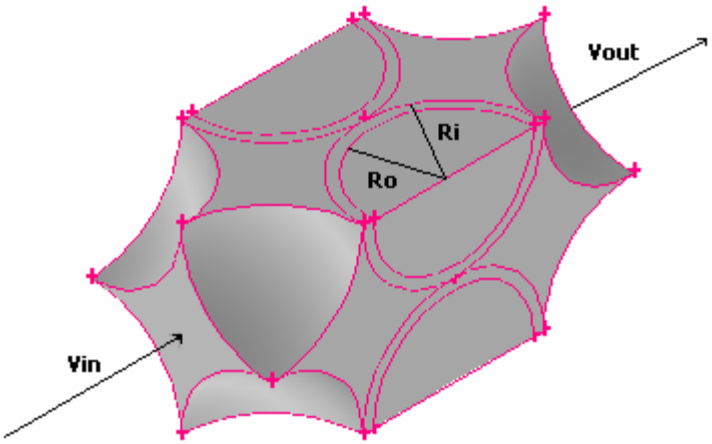


**Figure 4.3: Geometry layout for the spherical capsule computational domain.**

The front, side and auxiliary views for the spherical domain are shown in Figure 4.4.

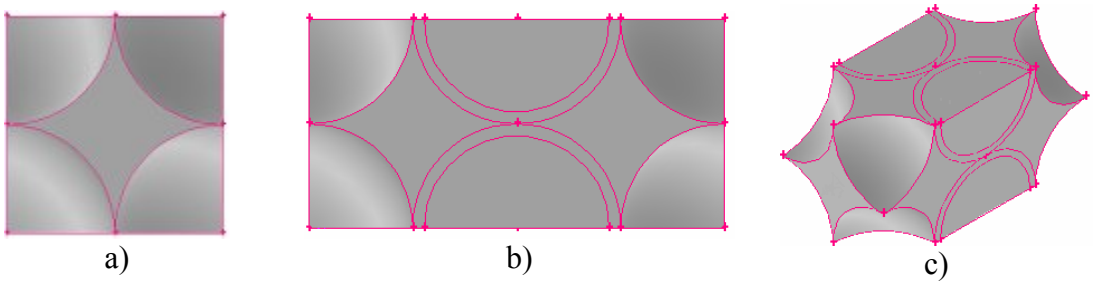


**Figure 4.4: Front view (a), side view (b) and auxiliary view (c) of the spherical capsule domain.**

The above geometry was constructed using GAMBIT software, and special consideration was taken when creating the grids. Firstly, since the gradients are usually strongest along the no-slip walls of a surface, the heat transfer fluid grids were created first, with special care taken on the boundaries of the outer PCM walls. A tetrahedral/hybrid element type was used for all elements in the domain, including the heat transfer fluid due to the spherical nature of the PCM capsules. The PCM and PVC zones were made with a much more even distribution of volumes, due in part to the negating of convection within the PCM and to the unknown liquid-solid interface location.

### 4.4.2 Cylindrical Capsules

For the cylindrical capsules, the computational domain will be similarly defined. The domain will again be a square cylinder, but in this case it will contain one quarter of four adjoining cylindrical capsules. This is again done to more precisely model a packed-bed of touching cylindrical PCM capsules. The heat transfer fluid inlet and outlet is then defined to be the area between capsules. The geometric layouts for each aspect ratio can be seen below in Figure 4.5. Notice that similar to the spherical capsule case, the inlet flow channel has been elongated in order to determine far-field boundary effects, which will be discussed in more detail in section 4.5.3.

The cylindrical capsule domains again were constructed using GAMBIT software, and once again special care had to be taken in order to simulate the real flow fields. As was done in the spherical capsule case, the front, side and auxiliary views of the domains can be seen in Figure 4.6.

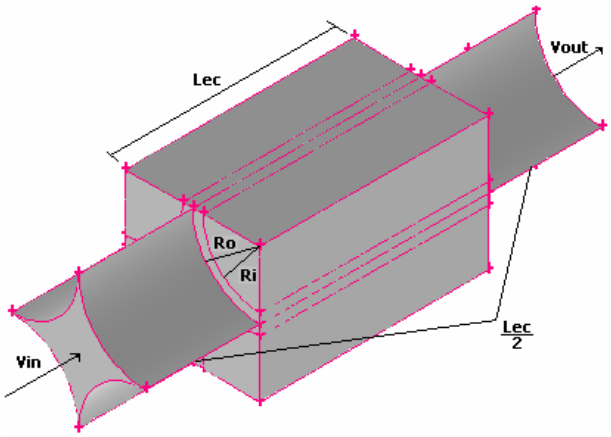


a)

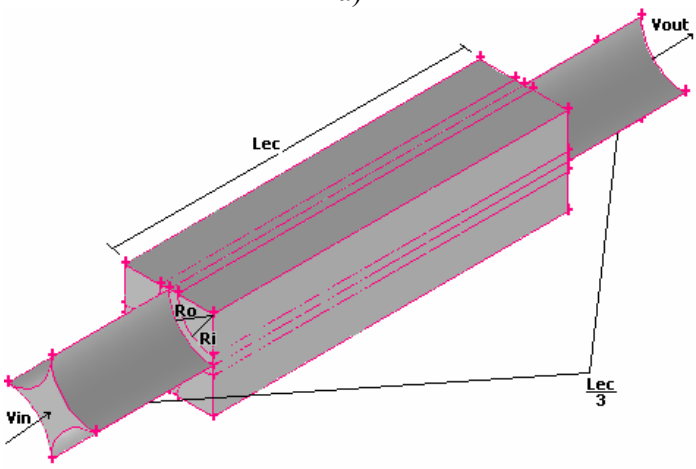


b)

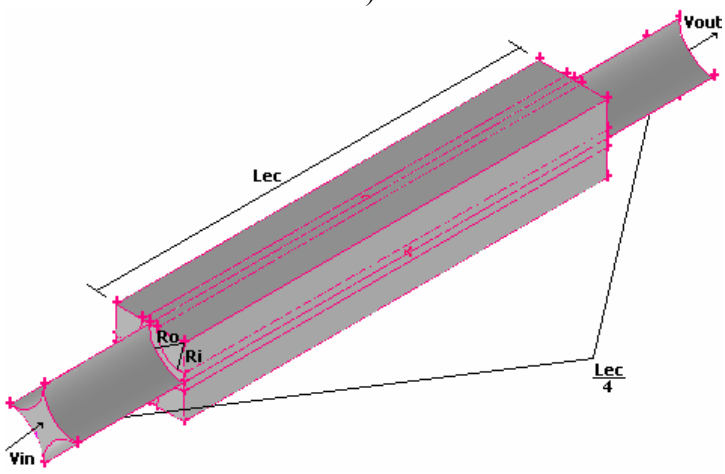


c)

**Figure 4.5: Layouts for the cylindrical capsule domains with aspect ratios of 2 (a), 5 (b) and 8 (c).**

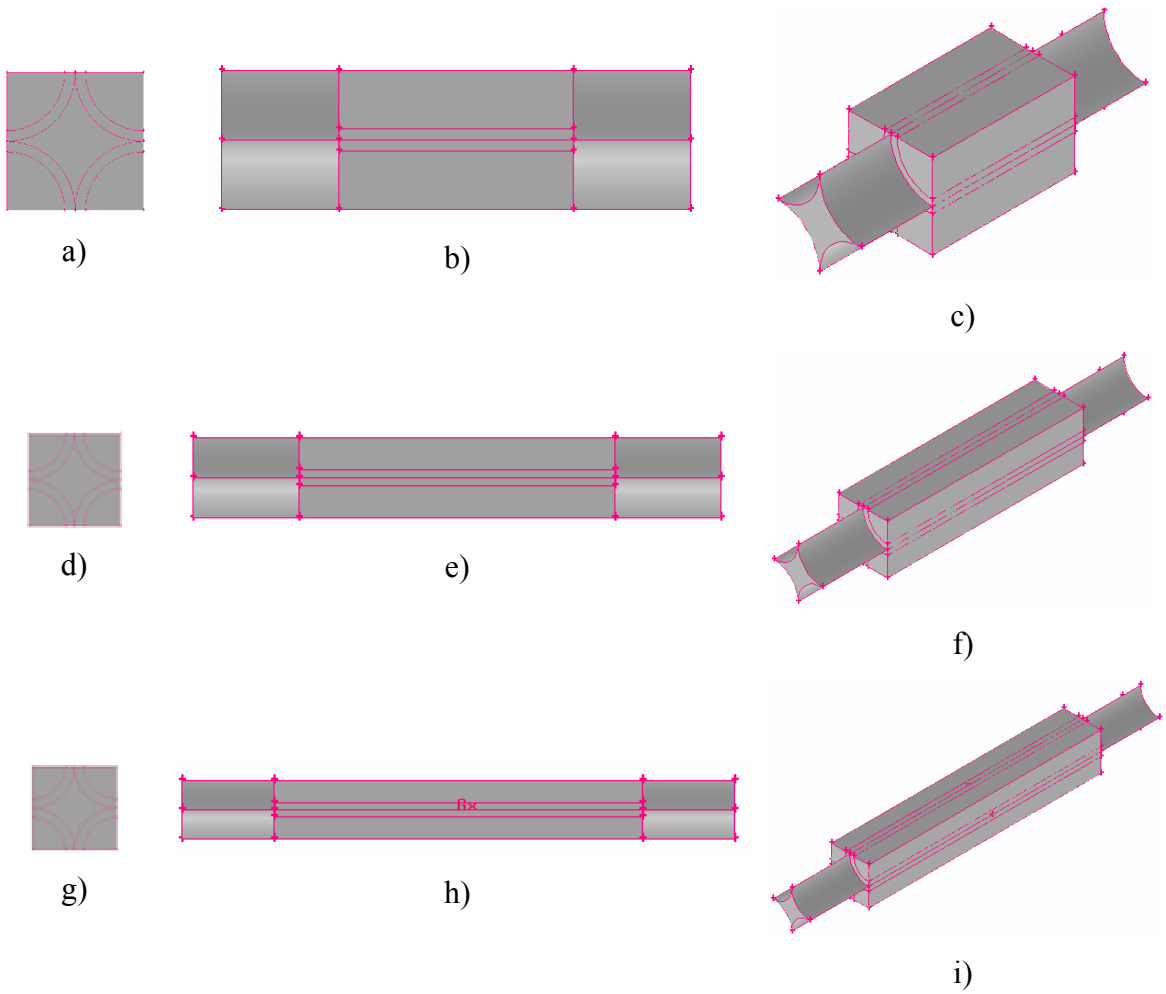


**Figure 4.6: Geometry layouts for the various cylindrical capsule domains. Front, side and auxiliary views, from left to right, are shown of the cylindrical capsule with aspect ratios of 2 (a,b,c), 5 (d,e,f) and 8 (g,h,i).**

In these cylindrical domains, a higher density of cell volumes was placed on the outer PVC walls, in order to solve for the boundary layer flows more precisely. The heat transfer fluid grid was created first, using hexahedron elements. Next, the PVC grid was created, with a larger spacing due to the same reasons as in the spherical case, and lastly the PCM grids were made using hexahedron and wedge elements, due to the corner wedges needed in each edge. Again, a more detailed look at the construction of the grid volumes can be seen in section 4.5.1. After the above were carefully constructed, the slab capsule domains were created next.

### 4.4.3 Slab Capsules

The slab capsules were somewhat more difficult to envision, since there is no universally accepted gap thickness between capsules for the heat transfer fluid to flow. However, since thinner capsules will need less heat flux through their surfaces to achieve solidification, it was decided that the spacing should be proportional to the thickness of the capsule itself. It was then decided that the gap spacing would be half that of the outer capsule thickness for two main reasons. One, it was noticed that this thickness was large enough not to affect the boundary layers of the smallest gap size (aspect ratio of 8) and two, it keeps geometric considerations constant when comparing the aspect ratios. As with the previous geometries, the geometry layouts for the three aspect ratios for the slab capsules are shown below in Figure 4.7.

Once again, the grid construction procedures were done so while taking attention to the PVC walls surrounding the heat transfer fluid. As a result, the boundary layers were created with a significant cell density in the boundary layer area of the flow field. The heat transfer fluid grids were made with a hexahedron type cell, as were all other zones, due to their rectangular prism shape. The inlet flow channel, as seen in the above figure, varies according to aspect ratio, but this will be addressed further in section 4.5.3.

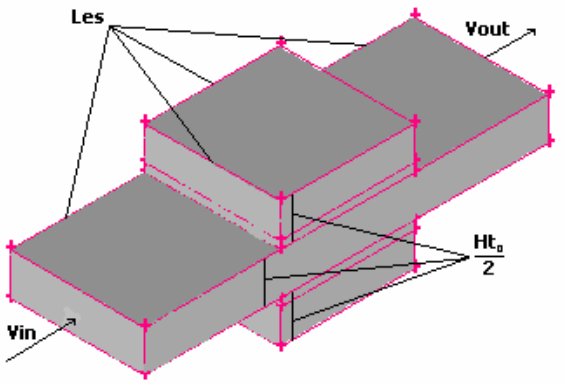


a)

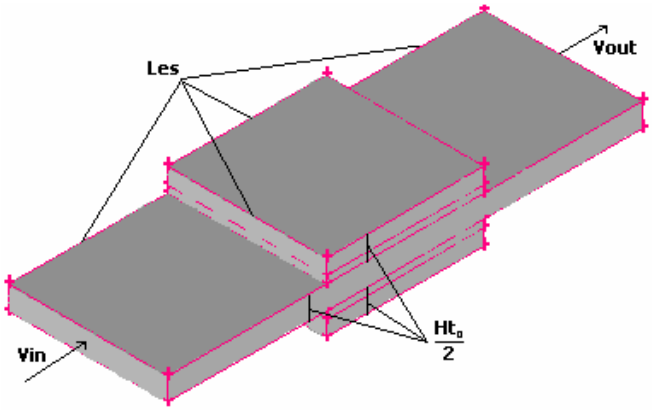


b)

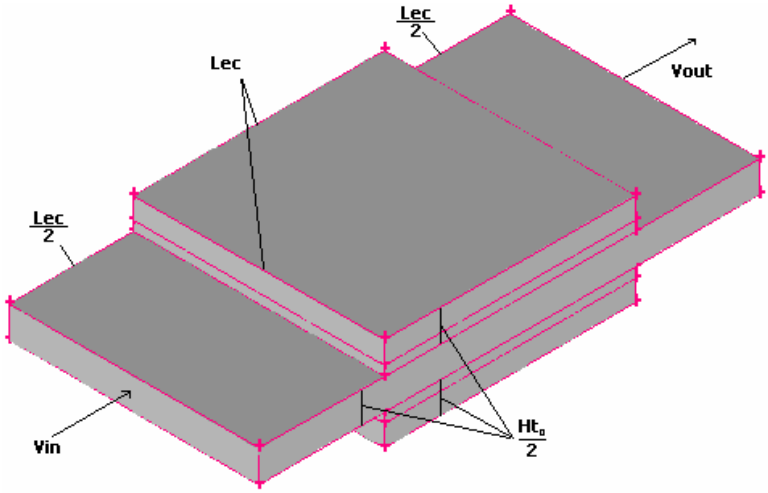


c)

**Figure 4.7: Layouts for the slab capsule domains with aspect ratios of 2 (a), 5 (b) and 8 (c).**

For a more visual interpretation of the various slab geometries used, please refer to Figure 4.8 below.

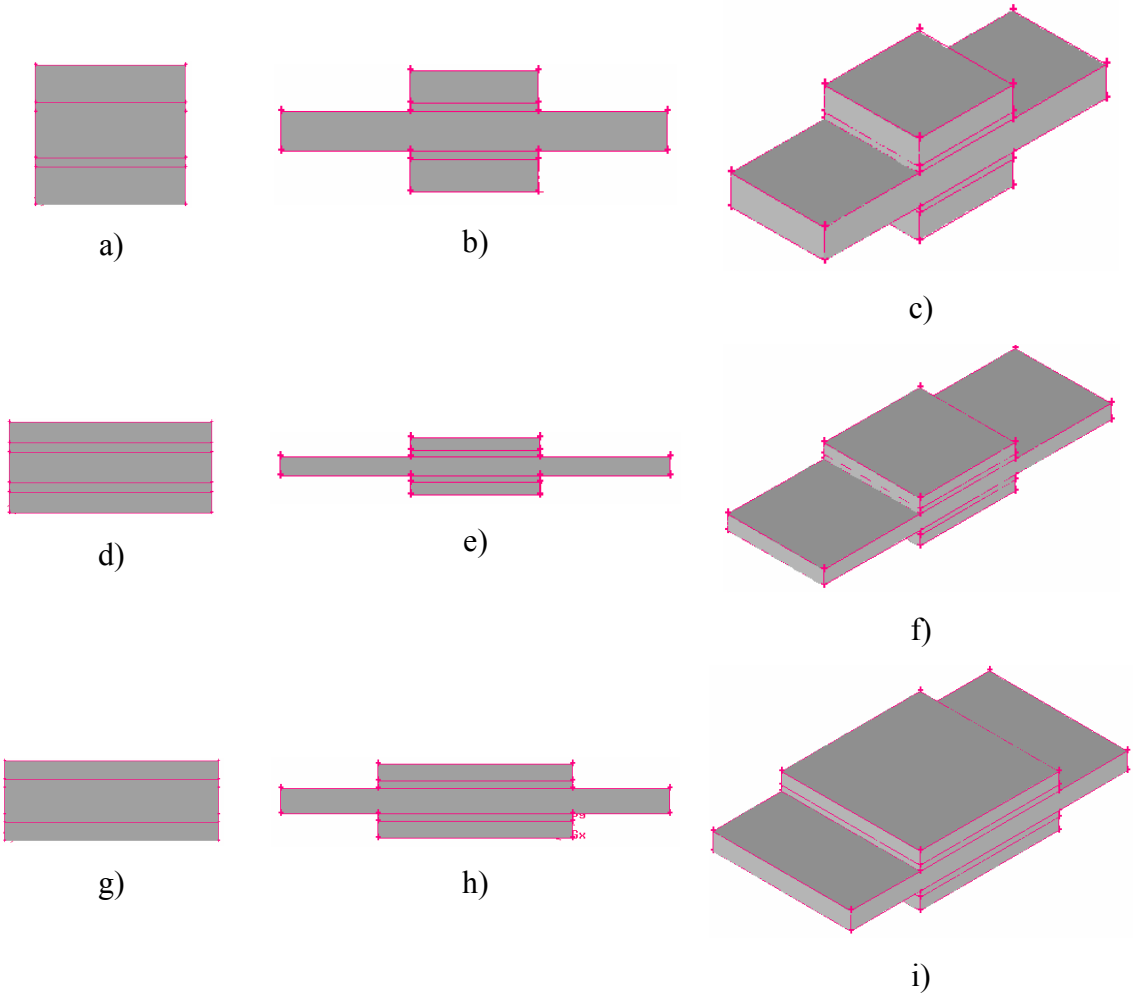


**Figure 4.8: Geometry layouts for the various slab capsule domains. Front, side and auxiliary views, from left to right, are shown of the slab capsules with aspect ratios of 2 (a,b,c), 5 (d,e,f) and 8 (g,h,i).**

## 4.5.0 Model Independence Tests

As noted earlier, before the results of the simulations can be taken seriously, a careful investigation of the dynamics of the model must be undertaken. Sensitivity tests, including grid sensitivity, time step independence and far field boundary independence tests must be completed and the model must perform in a satisfactory way for the results to be meaningful. The next few sections prove the independence of the model to these three criteria.

### 4.5.1 Grid Size Independence

When creating control volume domains for numerical procedures, one of the most important keys to the accuracy of the results is the grid size independence. When splitting the computational domains into volumes, there must be care taken to ensure that enough volumes are in place to keep the solutions accurate. On the other hand, if too many volumes are present, the computational times can increase significantly, making the process a lengthy one. So, there must be a middle ground between computational complexity and ease of solution, and this is done by performing a grid size sensitivity analysis. For all geometries constructed, the grid domains were created using the procedures outlined in section 4.4, but the cell densities in each region were allowed to vary to see the solution's dependence on the grid size.

As mentioned earlier, the grid orientation and size independence can be proved simultaneously; due to the irregular shapes used in the grid construction as well as the dependence of the grid structure on overall grid size. Therefore, it is assumed that the grid size independence tests will prove both size independence and orientation independence at the same time.

The grid size independence tests were performed by simulating the solidification of the water inside the capsules. The tests were also performed during the melting process, but since the results are quite similar, only the solidification case will be shown. It should be noted that for all geometries, the grid sizes which were used in the eventual solutions were arrived at only by careful consideration and a considerable amount of testing to ensure that the correct balance between grid size and computational time could be met.

To prove the grid size independence, all of the grids in question were restructured to contain more volumes, which increases the precision of the solution, and the liquid fraction was observed as time progressed. In the same manner, the grid was restructured again to contain fewer volumes, and the liquid fractions were again observed as time progressed.

The tests were performed by setting the following inlet and boundary conditions:

- $T_{in} = 269K$
- $Q_{in} = 2.68\text{e}^{-5}\text{m}^3/\text{s}$
- $\overline{T}_{htf,ini} = 269K$
- $\overline{T}_{pvc,ini} = \overline{T}_{pcm,ini} = 275K$

It should be noted that only the inlet flow rate is specified, while in the solution procedures the inlet velocity must be specified. This is done with the following equation, with the subscript *n* referring to the *n* different geometries:

$$V_n = \frac{Q}{A_n} \tag{4.72}$$

The resulting grid size independence for all geometries on the liquid fractions of the capsules was then recorded at intervals of 0.5s, and can be seen in Figures 4.9 – 4.15. It should be noted that since the liquid fraction is a great indicator of the heat transfer characteristics to and from the capsules, it serves as a sufficient gauge to the overall grid performance.

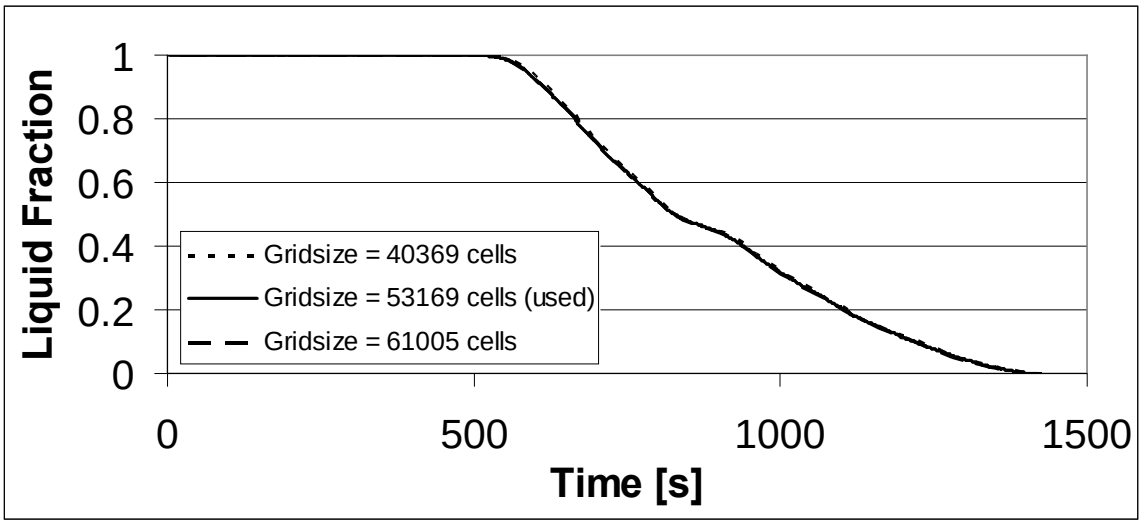


**Figure 4.9: Grid size independence of the spherical capsule domain.**

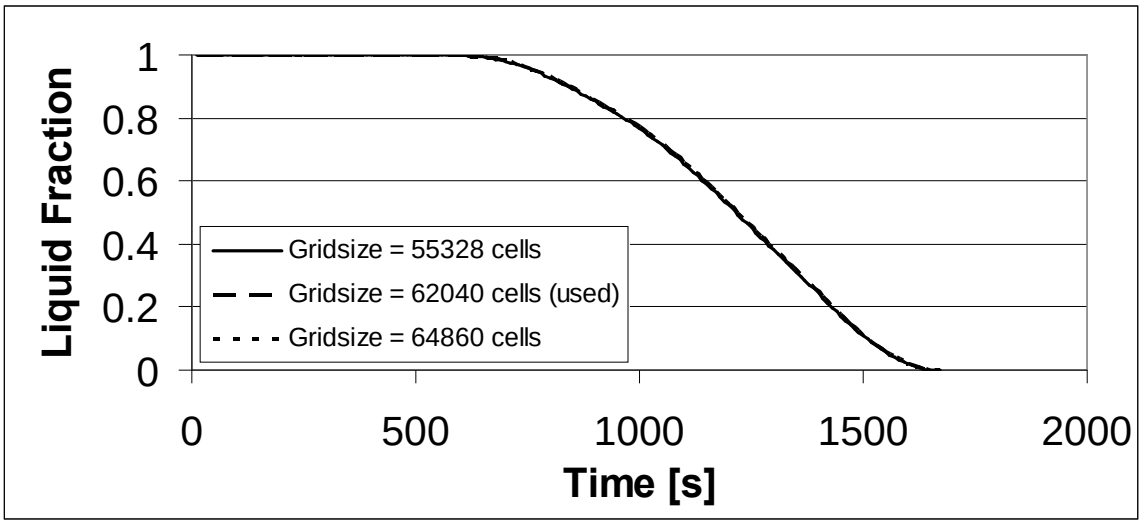


**Figure 4.10: Grid size independence of the cylindrical capsule domain (aspect ratio of 2).**

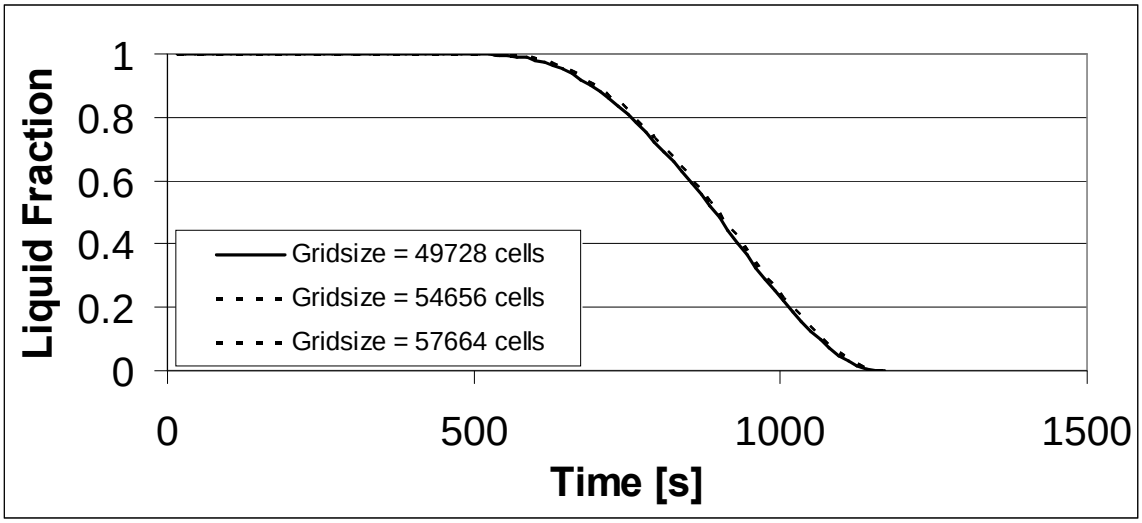


**Figure 4.11: Grid size independence of the cylindrical capsule domain (aspect ratio of 5).**

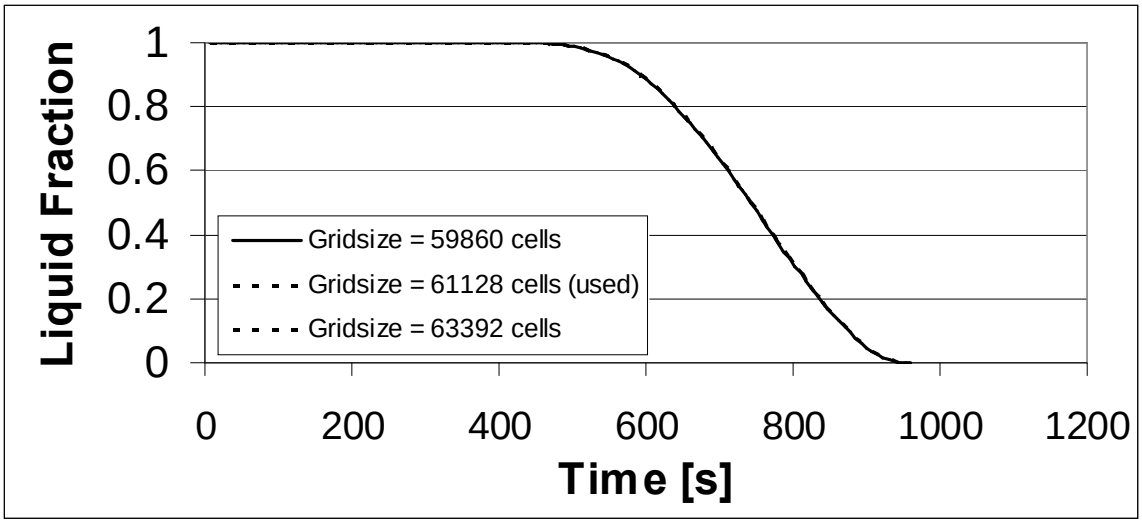


**Figure 4.12: Grid size independence of the cylindrical capsule domain (aspect ratio of 8).**

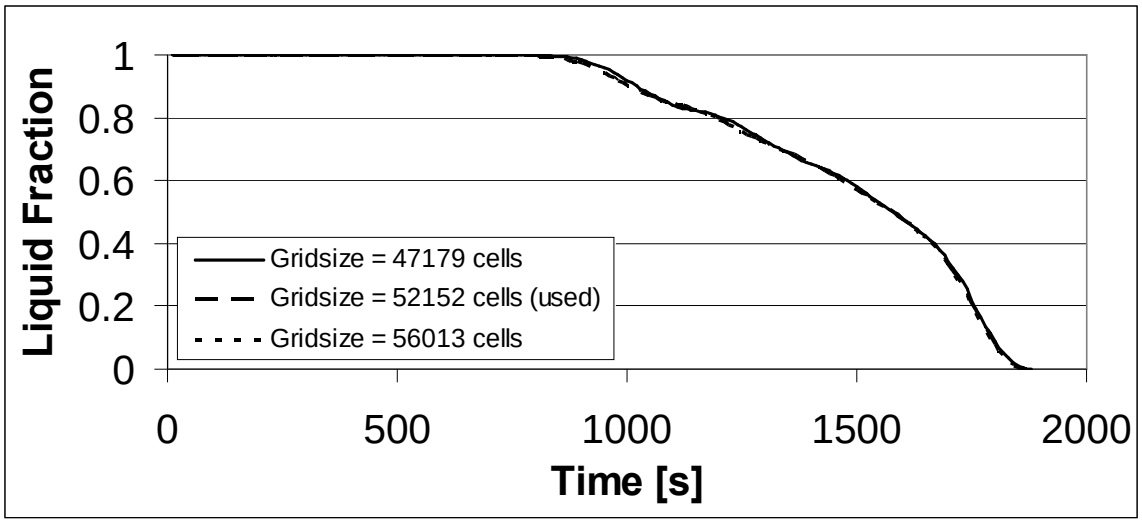


**Figure 4.13: Grid size independence of the slab capsule domain (aspect ratio of 2).**

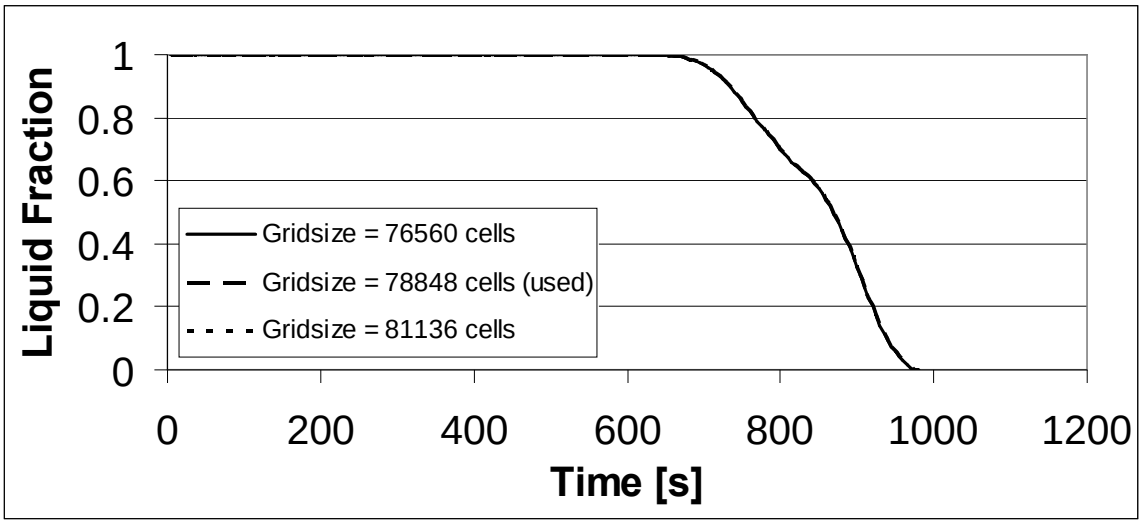


**Figure 4.14: Grid size independence of the slab capsule domain (aspect ratio of 5).**

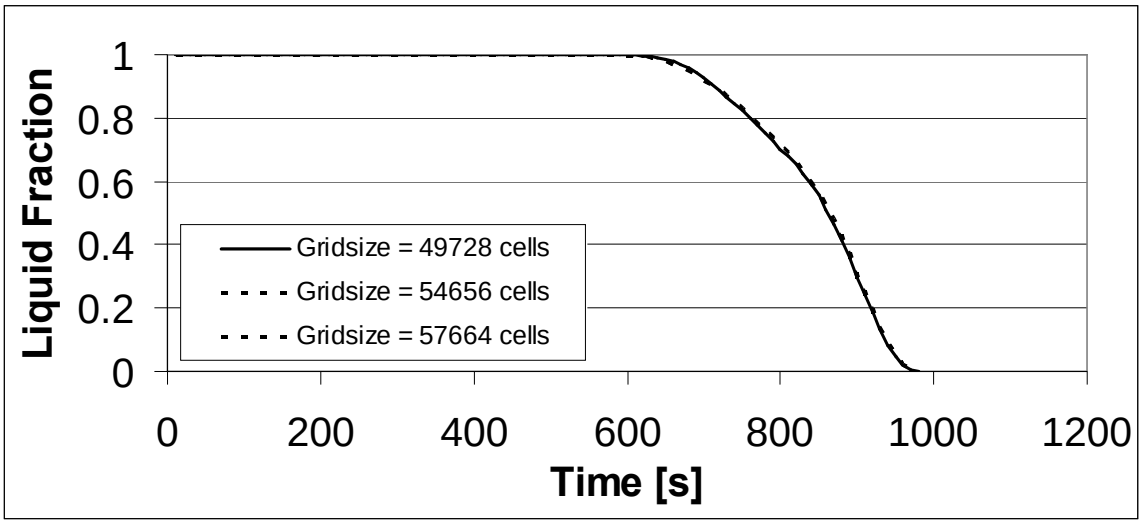


**Figure 4.15: Grid size independence of the slab capsule domain (aspect ratio of 8).**

When analyzing the above figures, it is quite apparent that the changes in grid size make little impact on the overall solutions. It is for this reason why these grid sizes were selected.

### 4.5.1 Time Step Independence

When validating numerical solvers, the time step independence is just as important as the grid size independence. In the same way that a larger grid size may not allow for the proper retention of information, a larger time step can produce the same effect. Conversely, if the time step is too small, computation times can become extremely large. A balance must be met between the two: the algorithm must solve the problem in a relatively short period of time, and at the same time retain most of the flow field information. It can be quite cumbersome searching for the most acceptable time step for each case, but its discovery is worthwhile in the end with less tiresome solutions and more precise results. Again, as with the case of the grid size structuring, a great deal of consideration was taken to choose the most efficient time steps for the various geometries. The chosen time steps for all geometries are compared to other time steps, both below and above the chosen values, to graphically view the effect on the liquid fraction, as was done previously. The resulting time step independences for all geometries are shown in Figures 4.16-4.22.

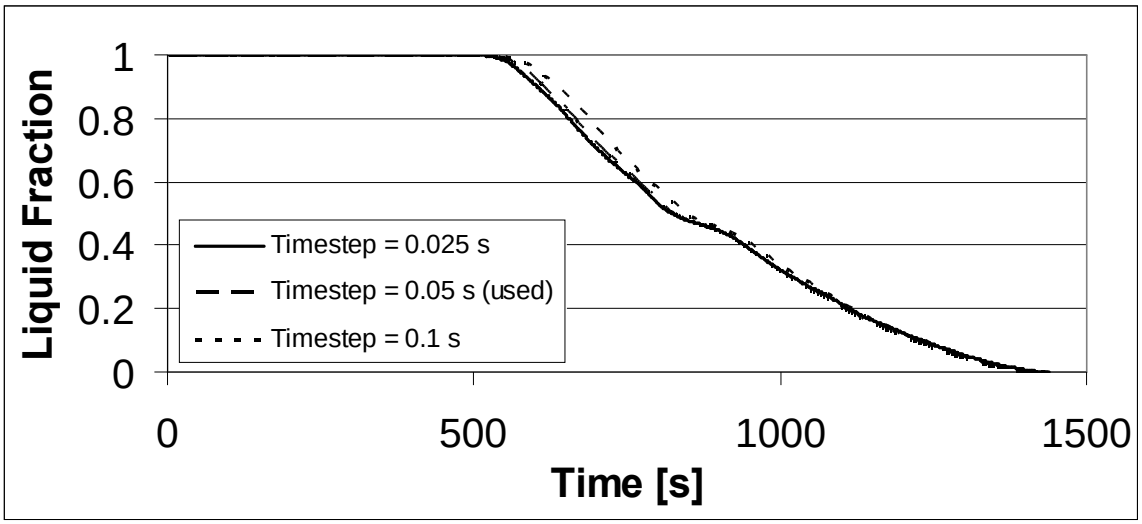


**Figure 4.16: Time step independence of the spherical geometry.**

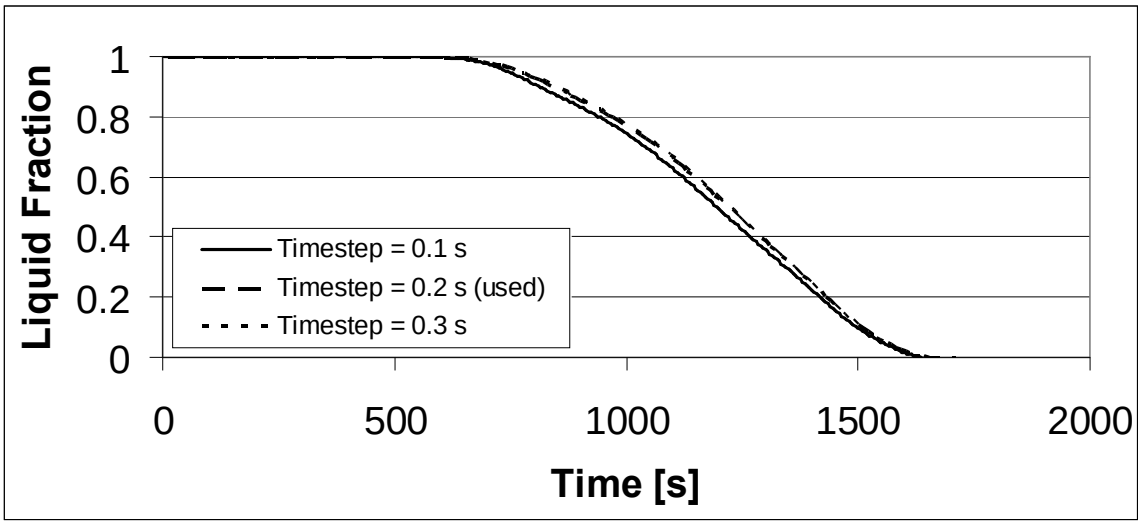


**Figure 4.17: Time step independence for the cylindrical geometry (aspect ratio of 2).**

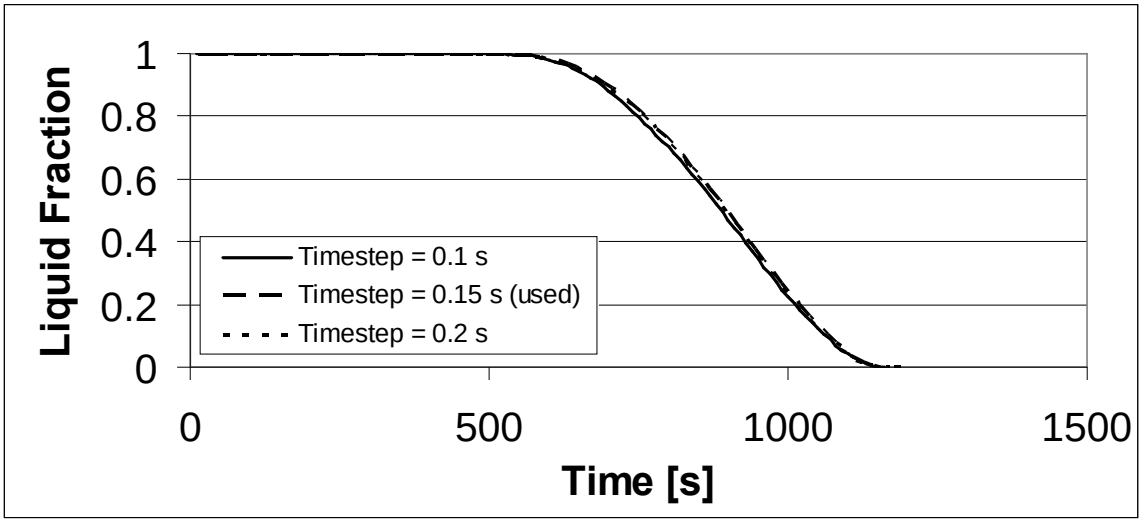


**Figure 4.18: Time step independence for the cylindrical geometry (aspect ratio of 5).**

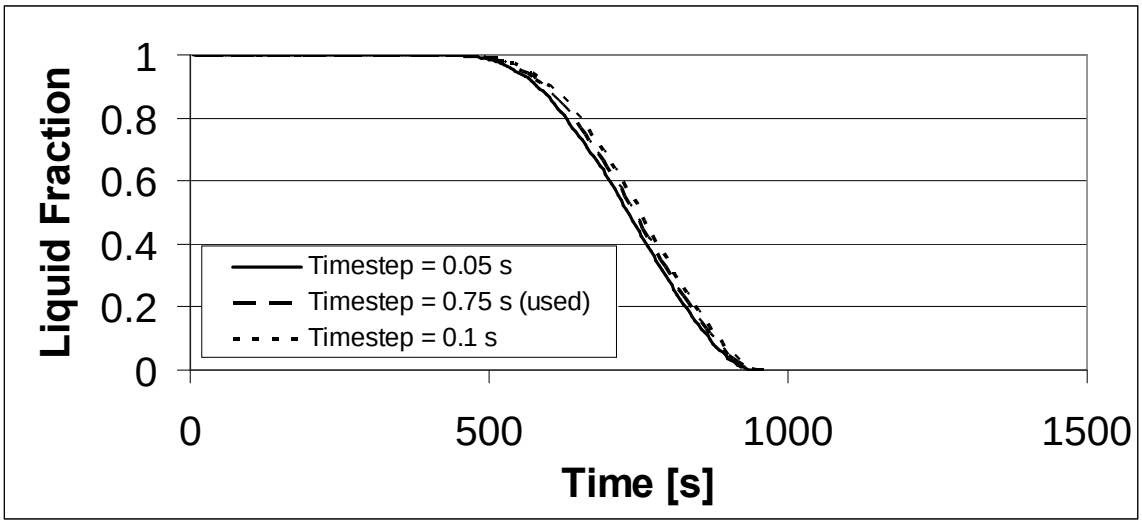


**Figure 4.19: Time step independence for the cylindrical geometry (aspect ratio of 8).**

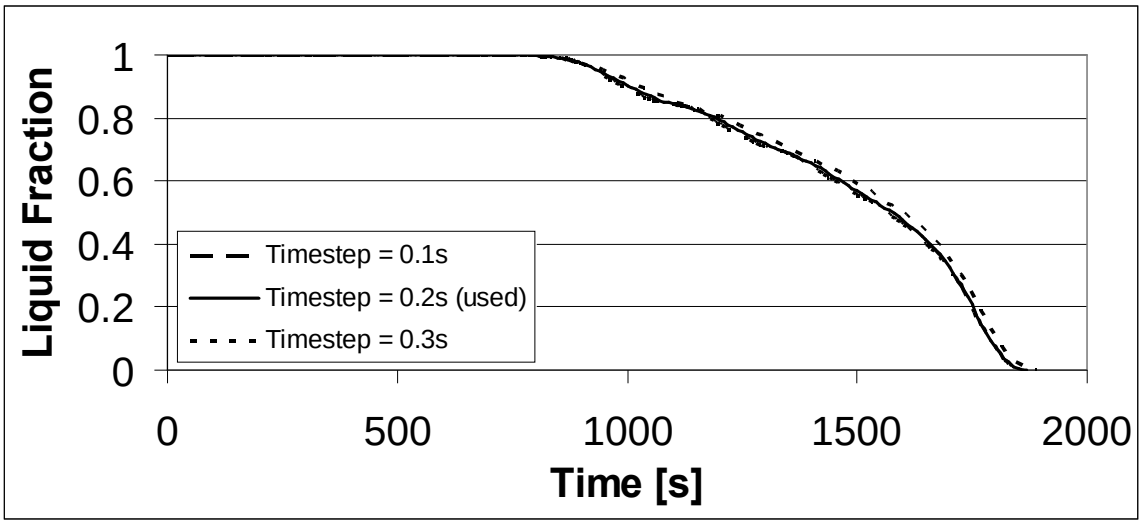


**Figure 4.20: Time step independence for the slab geometry (aspect ratio of 2).**

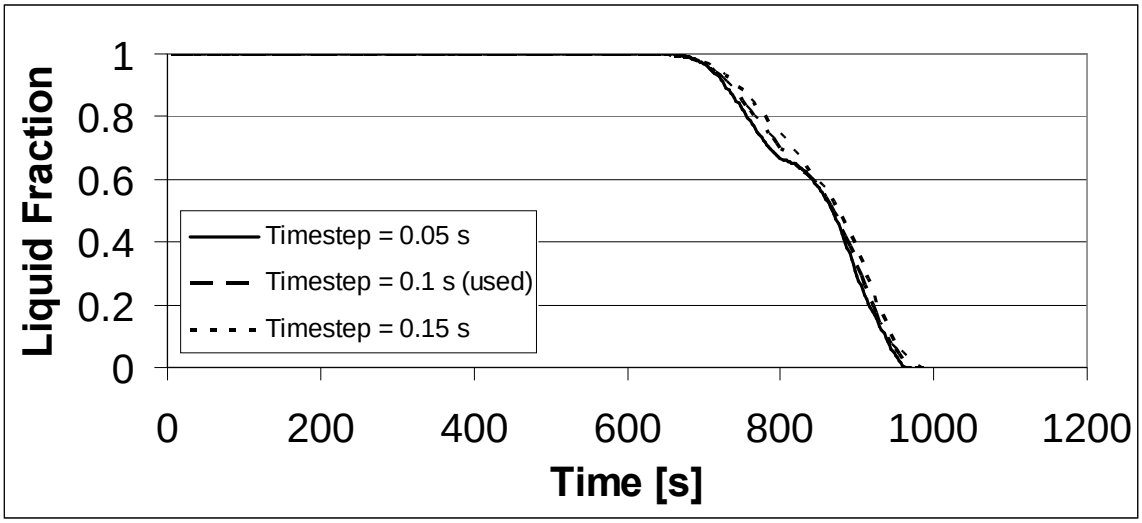


**Figure 4.21: Time step independence for the slab geometry (aspect ratio of 5).**

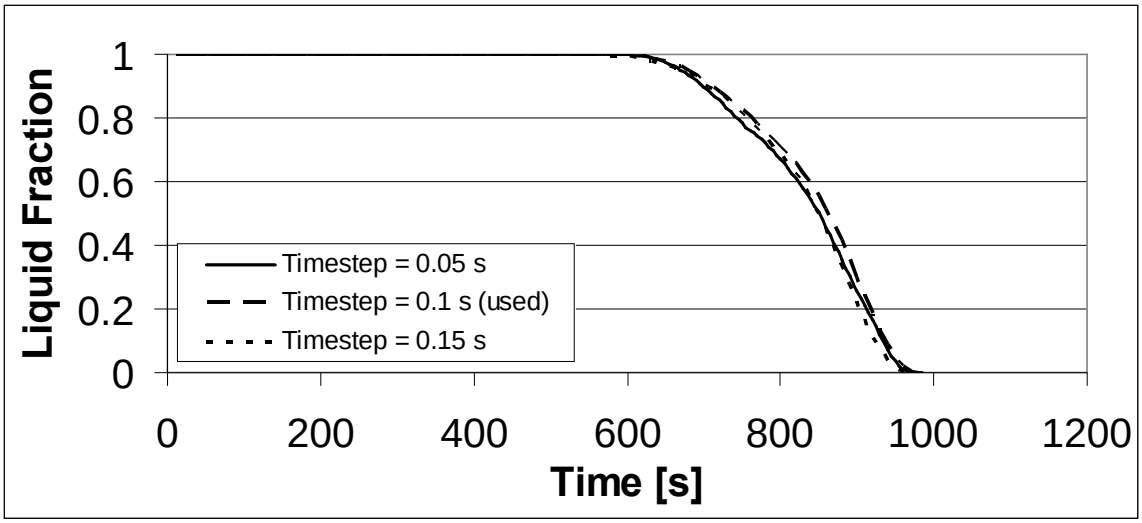


**Figure 4.22: Time step independence for the slab geometry (aspect ratio of 8).**

When viewing the above figures, one can see that the time step does have a small effect on the overall solution. Still, the small variations in the liquid fraction as time progresses is quite small, and since the solidification times are extremely close, the above time steps should be more than adequate.

Since the time step and grid size independence of the solutions have now been addressed, the far field boundary conditions must be briefly dealt with for completeness of the independence criteria.

### 4.5.3 Far-Field Boundary Condition Independence

There is one more step to conclude the independence of the numeric solution in regards to the constructed parameters; the far-field boundary condition independence. Although FLUENT uses an overall continuity correction and a zero diffusion flux for outflows, some of the geometries (namely, the spherical capsules) do not allow for a fully developed flow to be achieved. For this reason, the inlet flow channels in Figures 4.2, 4.4 and 4.6 are constructed as illustrated. The goal of these elongated flow channels is to determine by how much the development of the HTF flow will affect solutions. If the flow is not independent of these far-field inlet and outlet conditions, the solutions will not be similar and they will not achieve independence of far-field boundaries. To prove independence of the above geometric models from the far-field conditions, each grid was elongated considerably to include a larger inlet and outlet flow channel. The grid construction and time steps were completed with the same optimal parameters as chosen for the grid size and time step independence tests. The solution was also allowed to proceed with the same boundary and initial conditions as for the grid and time step independence cases. A more visual interpretation of the auxiliary views of the domains with the elongated flow channels can be seen in Figure 4.23, and comparisons can be made with Figures 4.2, 4.4 and 4.6.

For the cylindrical and slab capsules, the question of the existence of fully developed flow is moot, since the heat transfer fluid boundary remains constant along the length of the flow channel, and the flow will at some point become fully developed. In the case of the spherical capsules, however, the notion of “fully developed” can not be understood in the same way.

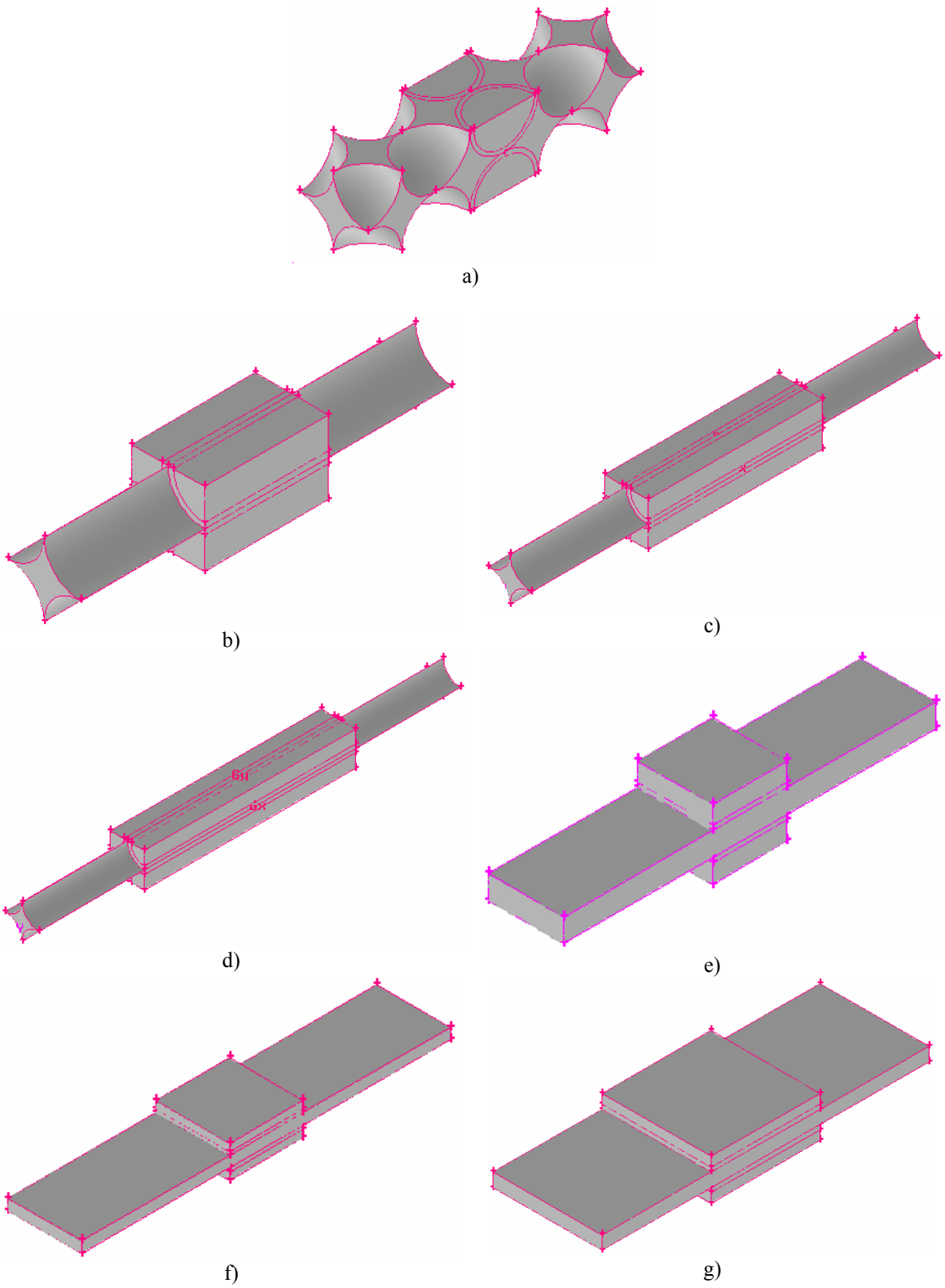


**Figure 4.23: Elongated flow field channel domains to illustrate the effect of far-field boundary conditions. The elongated spherical capsules (a) is shown along with the cylindrical capsules of aspect ratio 2 (b) 5 (c) and 8 (d), along with the slab capsule of aspect ratio 2 (e) 5 (f) and 8 (g).**

This reason explains why the diffusion layers along the inner walls were not sought explicitly; rather the dependence on the length of the inlet and outlet channels on overall solutions were the main investigations. For example, in the case of the spherical capsules, the flow would never really become fully developed, since the boundaries surrounding the heat transfer fluid are always changing. It is for this reason why the notion of *fully developed* is not investigated, so that all geometries may be compared similarly. For the case of the spherical capsules, an extra set of capsules were added to determine the effect of this far-field boundary, as can be seen in Figure 4.23a.

For the other geometries, the flow inlet and outlet channels were simply doubled to determine the effects of this far-field boundary on the solution progress. As with the other independence tests, the results were tabulated by monitoring the liquid fractions, and the results are shown in Figures 4.24 – 4.30.

As can clearly be seen from these figures, the flow channels used in the simulations are clearly adequate for the far-field boundary conditions to be satisfied. It should also be noted that some geometries do not experience as smooth a transition while freezing as others do. This is due to the piecewise – linear nature of the thermophysical properties of the system. Since, at the freezing point of 273K, the PCM conductivity and specific heat jump suddenly, the rate of change of freezing slows somewhat, but this does not affect the overall validity of the results, which is discussed in section 5.1.

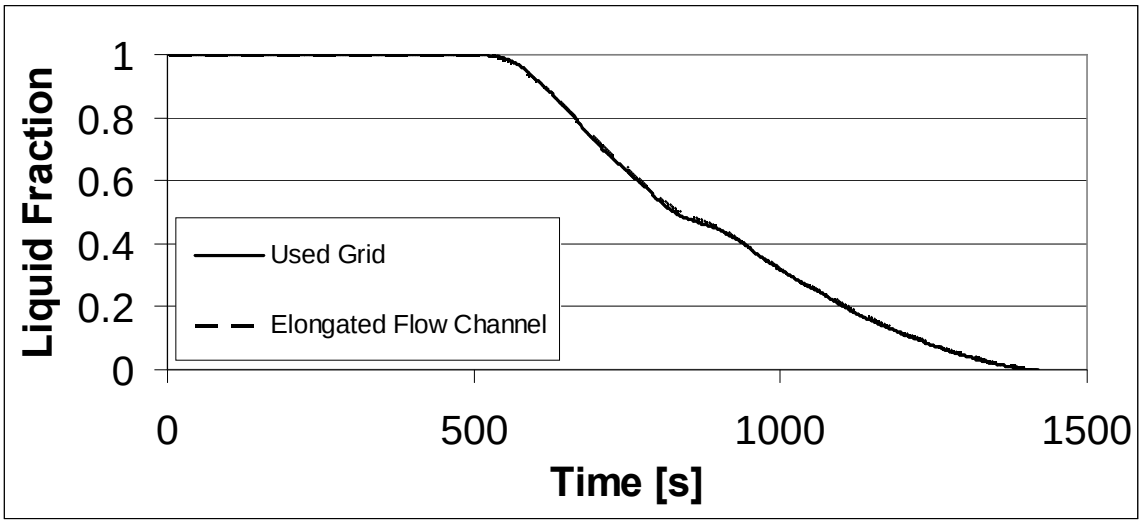


**Figure 4.24: Far-field boundary independence of the spherical domain.**

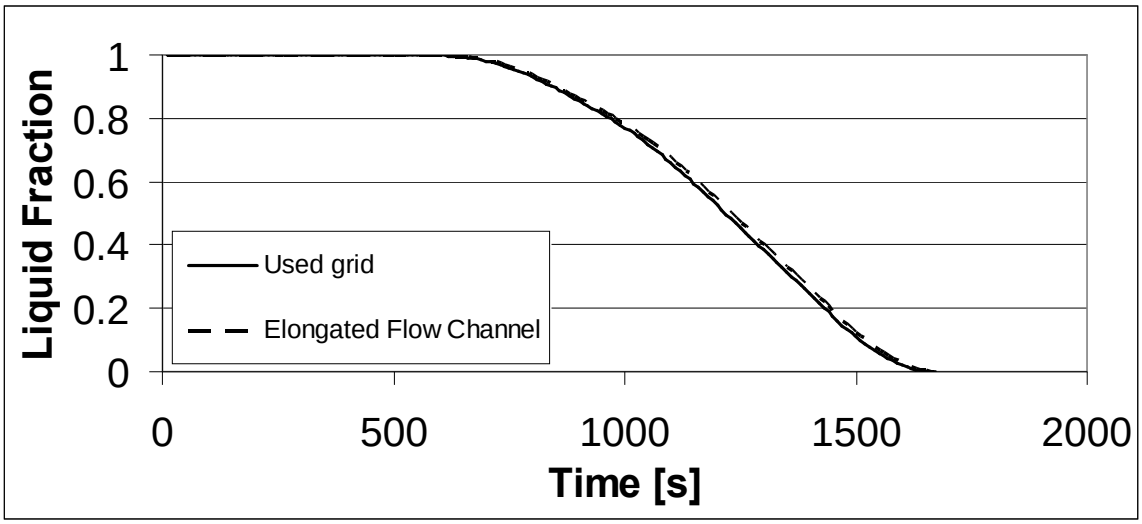


**Figure 4.25: Far-field boundary independence of the cylindrical domain (aspect ratio of 2).**

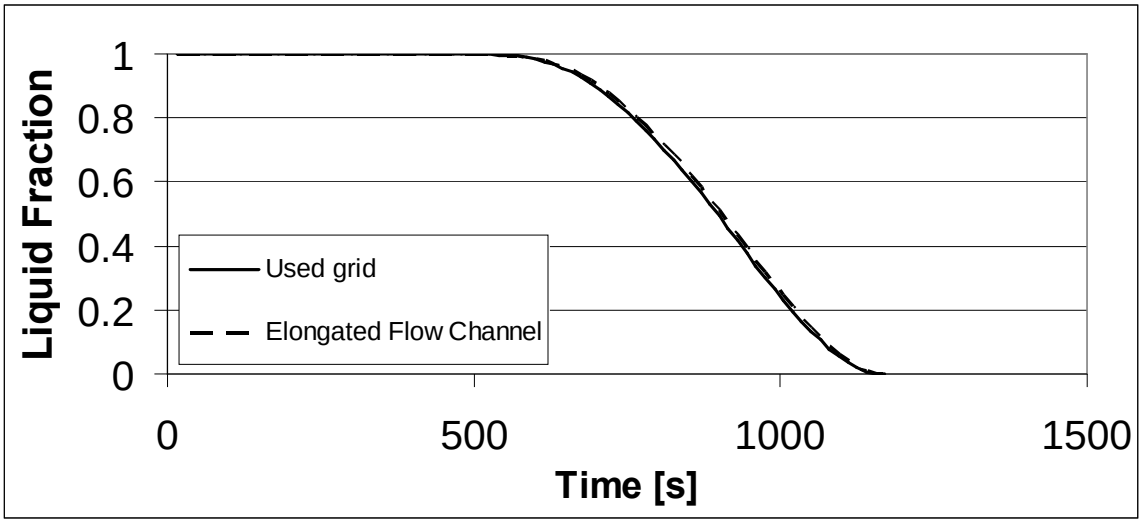


**Figure 4.26: Far-field boundary independence of the cylindrical domain (aspect ratio of 5).**

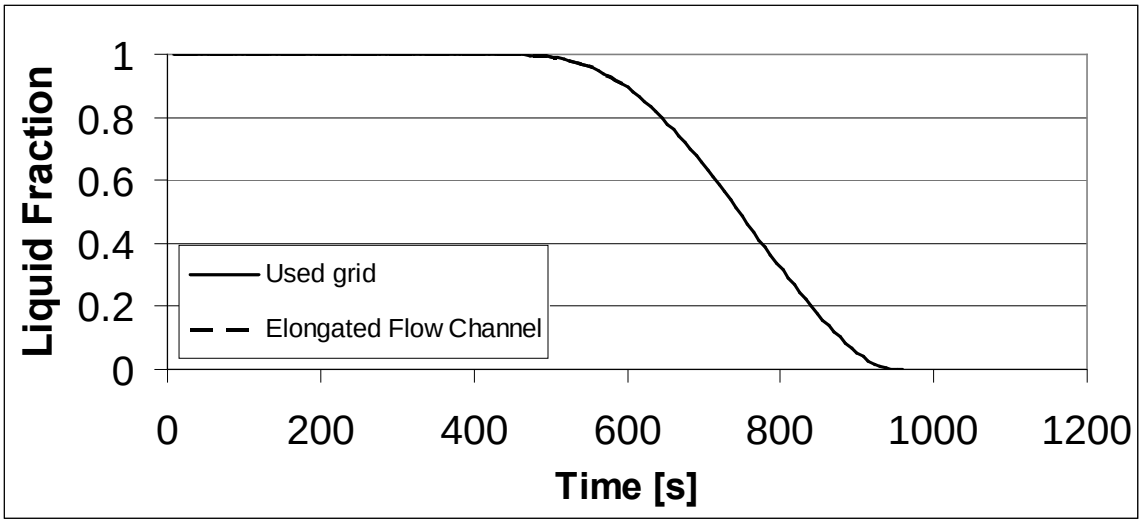


**Figure 4.27: Far-field boundary independence of the cylindrical domain (aspect ratio of 8).**

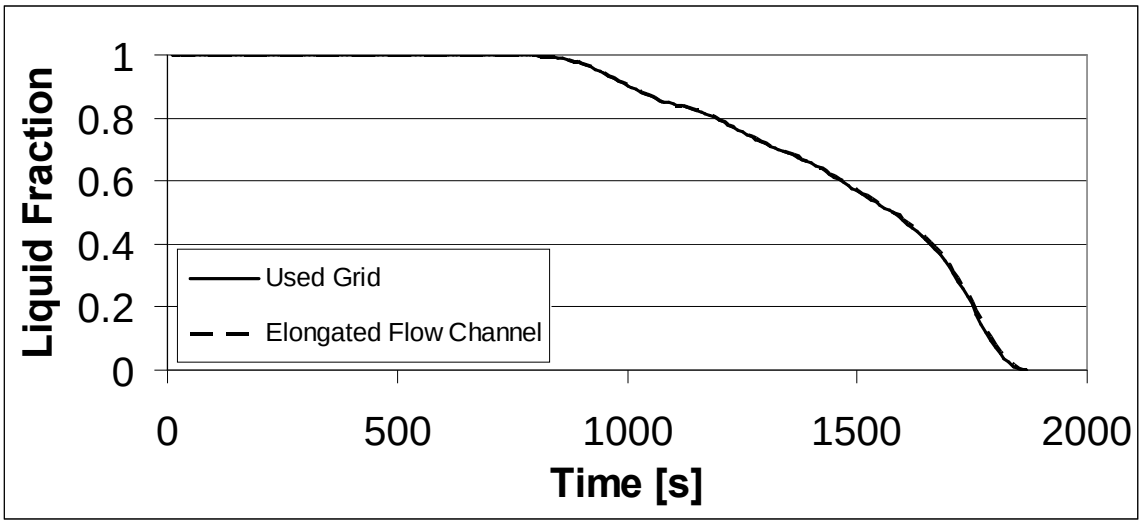


**Figure 4.28: Far-field boundary independence of the slab capsule domain (aspect ratio of 2).**

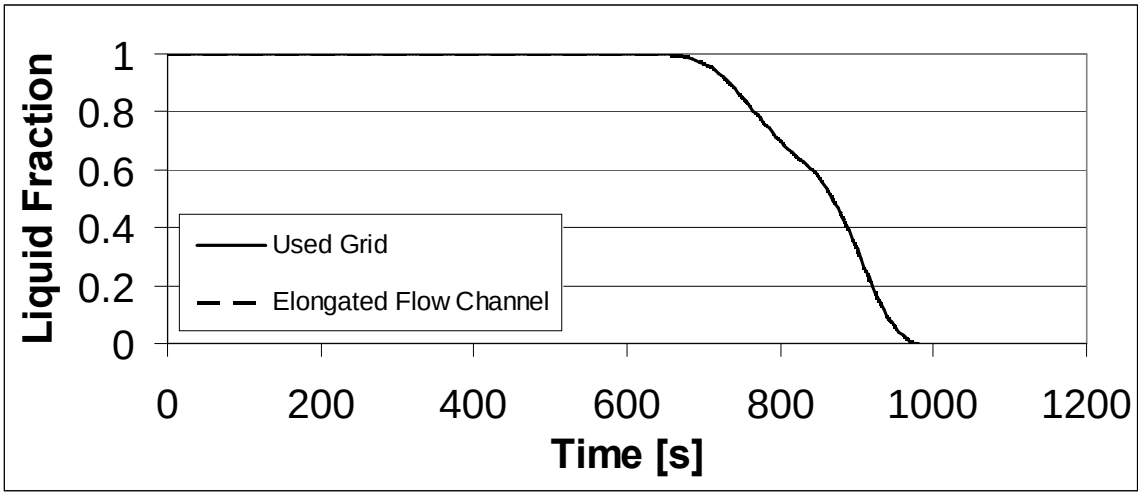


**Figure 4.29: Far-field boundary independence of the slab capsule domain (aspect ratio of 5).**

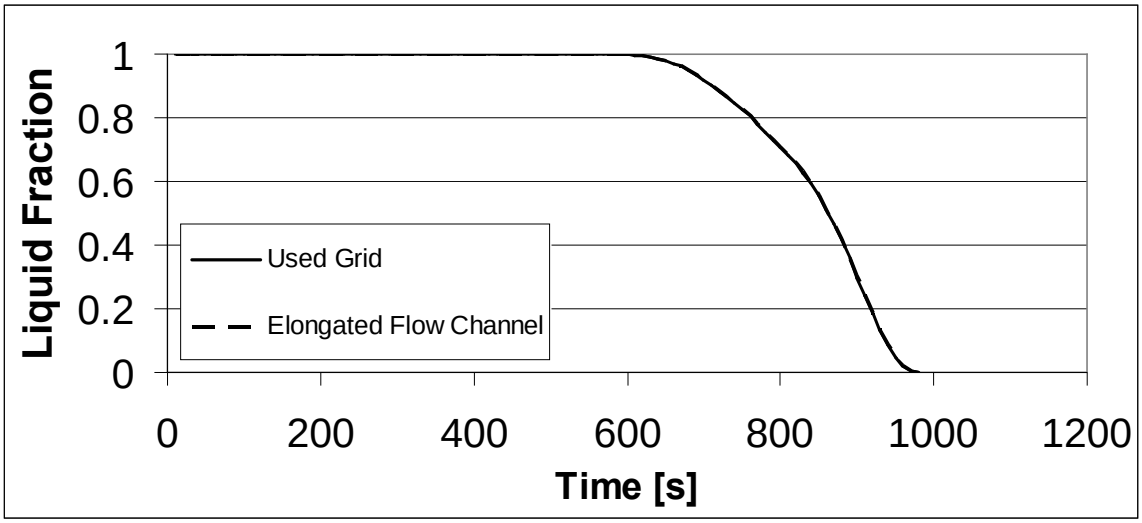


**Figure 4.30: Far-field boundary independence of the slab capsule domain (aspect ratio of 8).**

# 5.0 Results and Discussion

This chapter deals with the main findings and applications of the numerical results. The process of solidification is investigated first, and the effect of the inlet heat transfer flow rate, the inlet heat transfer temperature, and the geometry of the capsules on various system performance criteria is investigated. These criteria include the normalized energy efficiency, exergy efficiency and exergy destroyed within the system. Afterwards, the solidification process is examined in the same accord. Finally, the effect of the dead-state temperature on the above criteria will also be investigated and other comparisons between the charging and discharging processes can be made.

However, before charging into the results, a model validation must be performed to ensure the model is a viable simulation of real-world processes. This validation is done in the next section, and the results follow shortly thereafter.

## 5.1 Model Validation

As previously mentioned, before the results of the present study are to be taken seriously, a validation of the current model must be performed. A similar experiment to the one here has been performed by Ettouney *et al*. (2005). In this study, the process of both solidification and melting is observed in a small copper sphere. The experiment was run with air as the HTF and paraffin wax as the PCM. The properties of the paraffin wax given in this study are outlined in Table 5.1. It should be noted that, since density effects are assumed negligible, the average density was again taken as the PCM density in the numerical solutions. However, to show the dependence on this assumption, another trial was conducted, this one including density change effects in the capsule.

The experimental process in this study occurs as follows: the air enters a cylindrical duct, initially at 296K, which contains a small copper sphere with an inner diameter of 3cm. The capsule has a wall thickness of 1.2 mm and contains the paraffin wax PCM. The air has an inlet temperature of 333K and an inlet velocity of 10 m/s. Thermocouples are placed at different angles with respect to the inlet flow direction

along the inner diameter of the sphere, and the transient temperature profiles are recorded. A small opening is left on the top of the sphere to allow for PCM expansion.

**Table 5.1: Thermophysical properties of the paraffin used in the model validation.**

| | |
|---|---|
| Solidification Temperature $[K]$ | 321.51 |
| Latent Heat $L$ $\left[ {kJ}/{kg} \right]$ | 210 |
| Solid Density $\rho$ $\left[ {kg}/{m^3} \right]$ | 860 |
| Liquid Density $\rho \left[ {kg}/{m^3} \right]$ | 780 |
| Solid Specific Heat $C \left[ {kJ}/{kgK} \right]$ | 2.9 |
| Liquid Specific Heat $C$ $\left[ {kJ}/{kgK} \right]$ | 2.1 |
| Dynamic Viscosity $\mu$ $\left[ {kg}/{ms} \right]$ | 0.15 |

Once total melting of the PCM has occurred, and the temperatures are close enough to the flow temperature (at $t$ = 1120s), the inlet temperature is changed abruptly back to 296K until complete re-solidification is observed. The results can be seen in Figures 5.1 – 5.3 for angles of 0º, 90º and 180º, respectively, for the experimental and both numerical solutions.

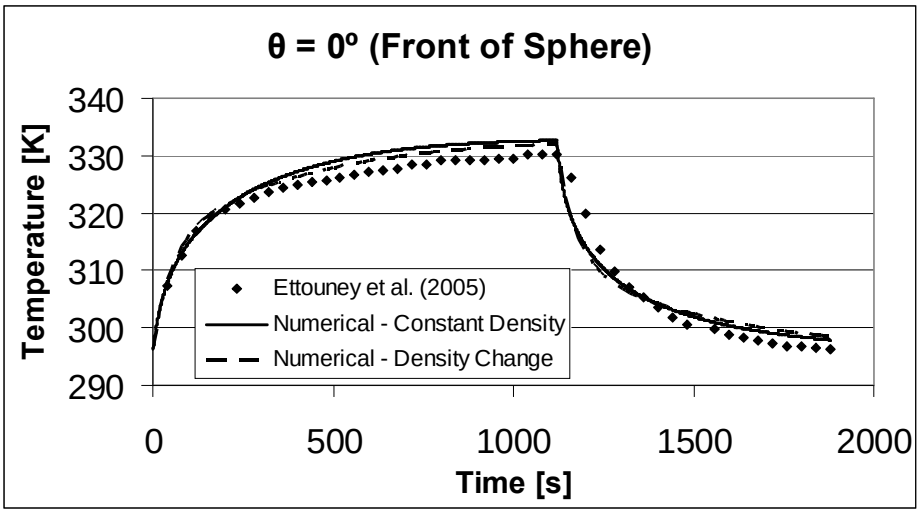


**Figure 5.1: Numerical and experimental temperature profiles at the front of the sphere (θ =0º).**

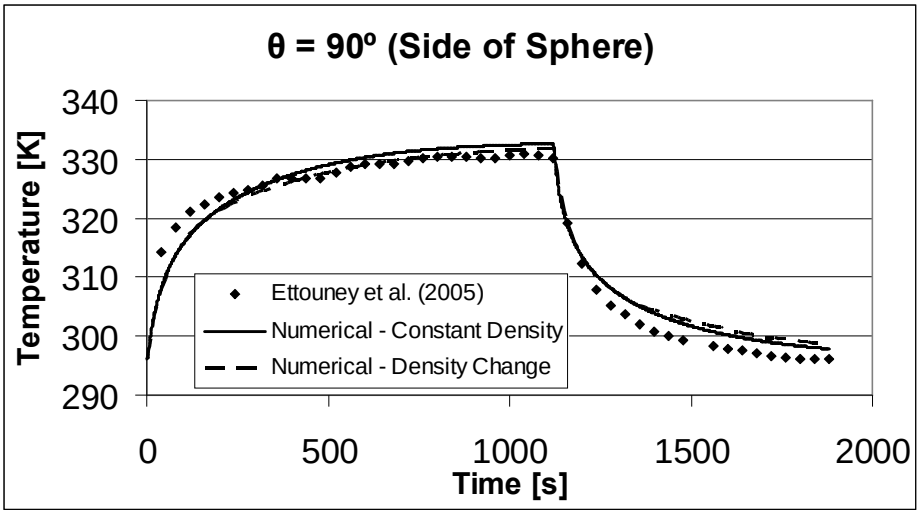


**Figure 5.2: Numerical and experimental temperature profiles at the side of the sphere (θ = 90º).**

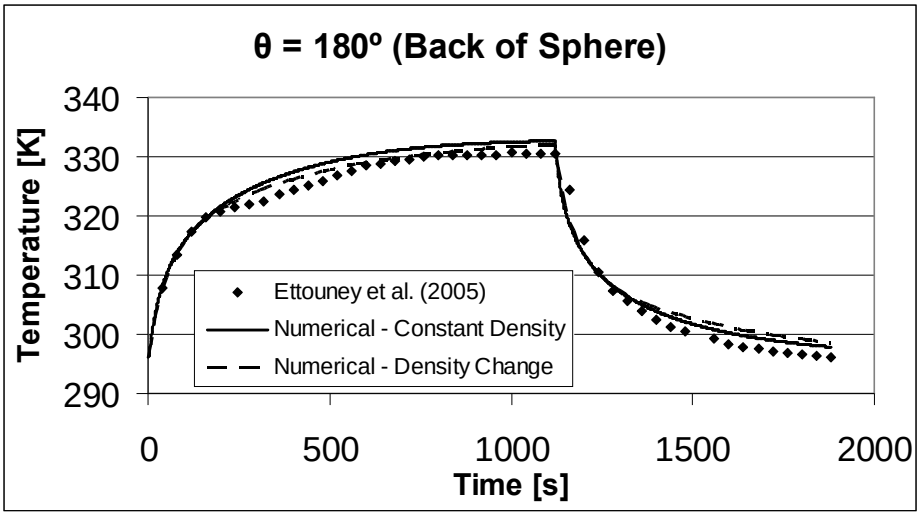


**Figure 5.3: Numerical and experimental temperature profiles at the back of the sphere (θ = 180º).**

It can be observed that the numerical and experimental temperature profiles do not exactly match, and that the numerical solutions that incorporated a change in density with phase transition were slightly more accurate. However, both numerical results can be assessed as more than satisfactory. Due to the long computational time required to incorporate this change in density (over 100 hours for just *one* trial), the numerical results using the average density should be deemed sufficiently accurate, while requiring only 3-4 hours of computational time to solve.

The differences between the numerical and experimental temperature profiles are most likely due to a number of factors, including contact resistance, small effects produced by the thermocouples embedded in the PCM, and possibly convection effects in

the PCM. However, the solidification and melting times, as well as the overall heat transfer rates, were of utmost importance to inspect, and the following results can be summarized.

- The time required for the PCM to completely melt was very close in both the experimental and numerical cases. Complete melting was reached in 600 seconds experimentally, while in the numerical solutions complete melting took 615 seconds, which is within 99.6% of the expected melting time.
- Once solidification was initiated in the experimental unit, an additional 280 seconds was required to complete solidification. This is again very close to the numerical value of 285 seconds, to within 98.5%.

These similarities between numerical and experimental results are encouraging, since the purpose of this paper is not to inspect the melt front, but to simulate the heat transfer and viscous forces between the PCM capsule and the flowing HTF.

Though there are no experimental validations known to the author which track the solidification and melting times in cylindrical and rectangular capsules in a cross flow, the other geometries cannot be similarly validated. However, since the numeric procedures in all cases are identical, and since the experimental and numerical solution temperatures, solidification times and melting times are very close, the model should be assumed accurate for all geometries explored in this study.

With the above in mind, and now that the model has been properly validated, the results of the solutions for the charging and discharging processes can now be examined.

## 5.2.0 Charging

For the charging process, the algorithm was run until the liquid fraction $\beta = 0$ everywhere in the PCM. Note that the reference temperature $T_\infty$ is set at 298K to simulate cold storage in a warmer region. While the reference temperature will remain constant at this value for the bulk of the analysis, the effect of varying this reference temperature on the performance of the charging and discharging processes will be discussed in section 5.4.

The charging (referring to solidification) process was run with three separate flow rates:

- $Q_1 = 8.7\times10^{-4}$ m$^3$/s
- $Q_2 = 1.74\times10^{-3}$ m$^3$/s
- $Q_3 = 2.61\times10^{-3}$ m$^3$/s

These flow rates were chosen to be small enough so that they could easily be attained in a storage tank of like capsules. If the algorithm's flow rates were too high, they would not be a reasonable estimate of the pumping requirements of a real world storage system. It is summarized that these three flow rates, when set into rows of a hundred capsules or so, would generated a required pumping flow rate of around 8.7 to 26.1 liters/s, which is not unreasonable for large pump flow rates with relatively small pressure heads.

Aside from the flow rates, the inlet temperatures are also varied. For the charging process, the inlet HTF temperatures were chosen to vary between 267K and 271K. Since heat transfer will be transferring to the HTF during this process, there will inevitably be a large variation in the HTF temperature, and the heat transfer fluid is likely to vary within these ranges at some point in the storage tank. The temperatures used here are attempting to duplicate real scenarios, since at the storage tank outlet, the HTF temperature will most likely be much warmer, a result of the heat transfer to the HTF from the PCM.

Since the remainder of the inlet and boundary conditions has been met, the results of the charging process for all flow rates, inlet HTF temperatures and geometries were simulated. With three flow rates, seven geometries and five inlet temperatures, this amounts to 105 total simulations for each of the charging and discharging cases.

### 5.2.1 Charging Times

The easiest and most explainable observations of the processes are the charging times. For each simulation, the total time taken for the liquid fraction to drop to zero was monitored, and is displayed in Figures 5.4, 5.5 and 5.6 for the flow rates $Q_1$, $Q_2$ and $Q_3$, respectively. Please note that "CYL" denotes the cylindrical capsules, while "AR" denotes the aspect ratio - these abbreviations will be used throughout the rest of the analysis.

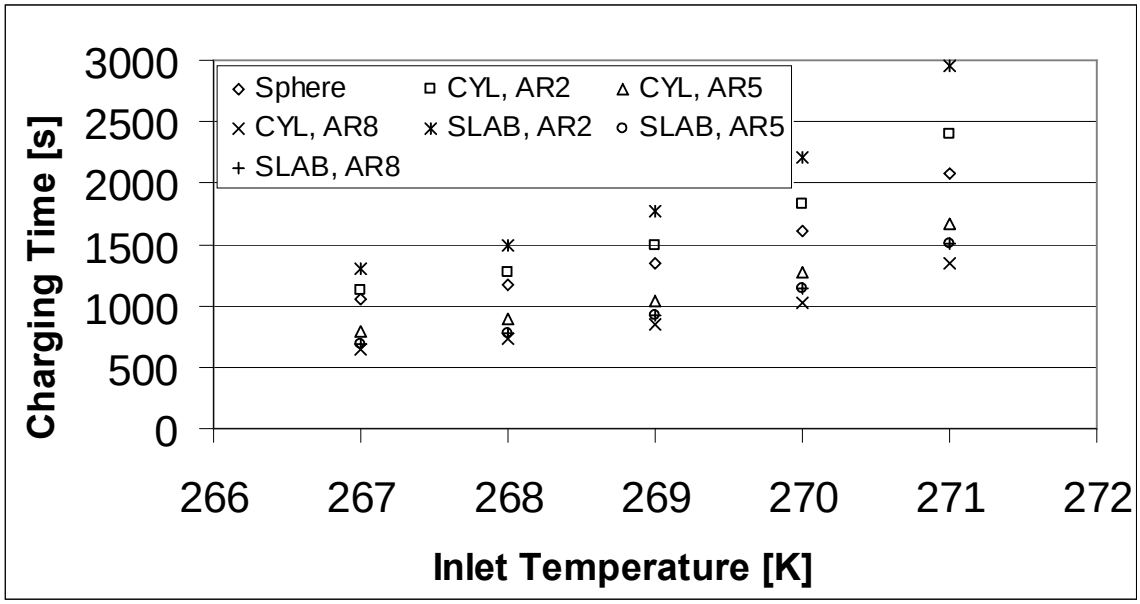


**Figure 5.4: Charging times for all geometries, with flow rate $Q_1 = 8.7\times10^{-4}$ m$^3$/s.**

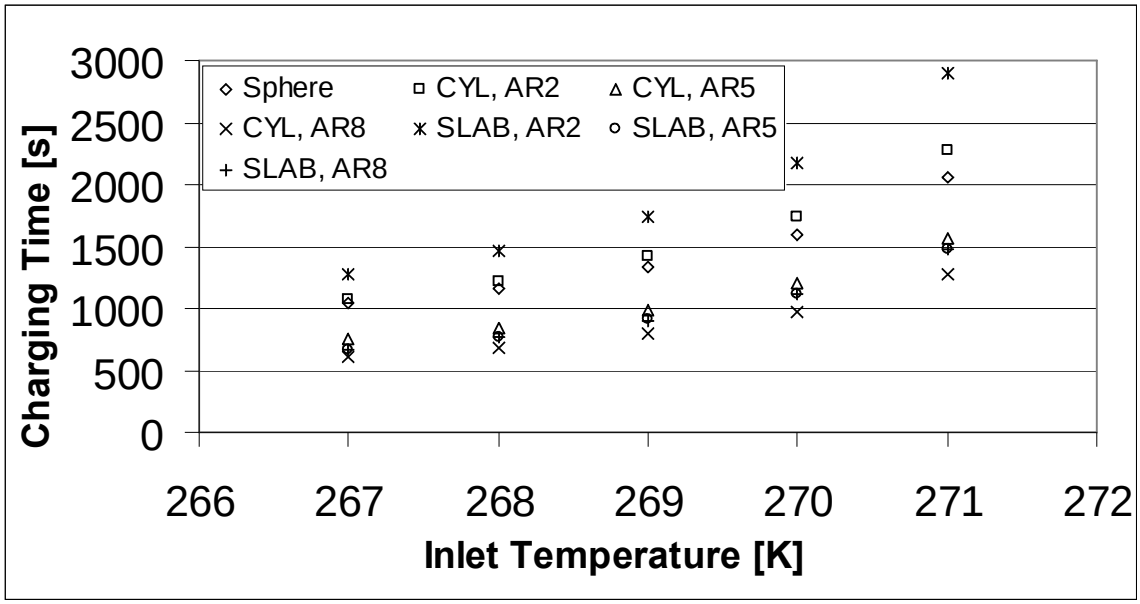


**Figure 5.5: Charging times for all geometries, with flow rate $Q_2 = 1.74\times10^{-3}$ m$^3$/s.**

Upon inspection of these figures, three main findings may be addressed. The first is the impact of inlet temperature on solidification time; as the inlet temperature decreases, the solidification time also decreases. This is due to the larger temperature gradients which exist between the capsule and the HTF when the inlet temperature is lowered.

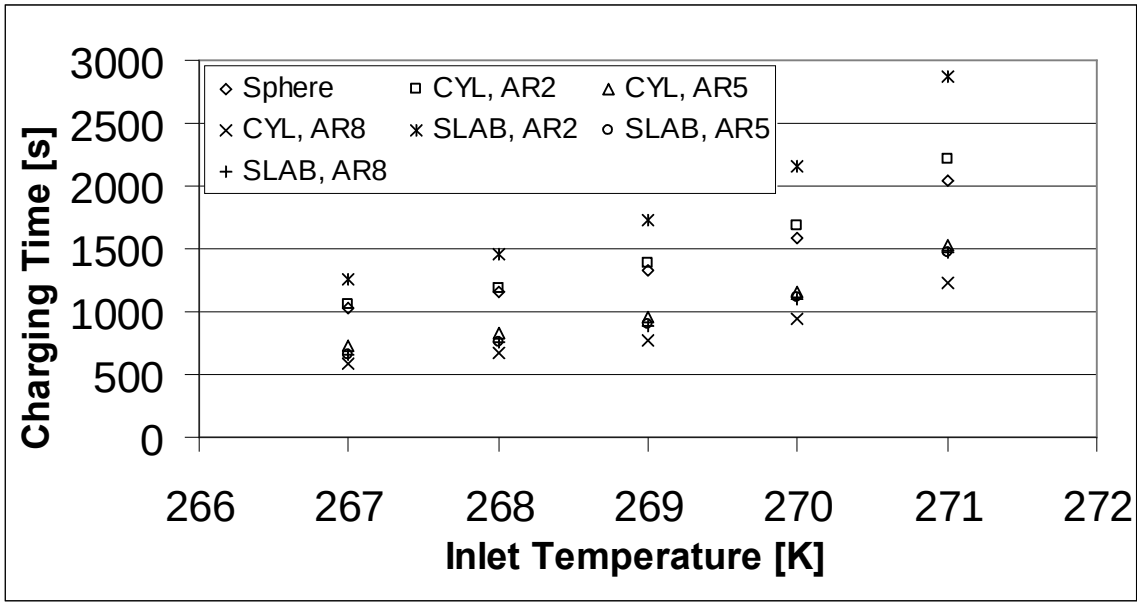


**Figure 5.6: Charging times for all geometries, with flow rate $Q_3 = 2.61\times10^{-3}$ m$^3$/s.**

Since Newton's Law of Cooling points out that the rate of heat transfer between an object and a convective flow is proportional to the difference between the surface temperature and the flow temperature, there should be no surprise in finding that there is more heat transferred to the HTF when it is at a much colder temperature than the capsules. When the inlet temperature is increased, there is much less temperature difference between the capsules and the surrounding HTF, so for the same reasoning, the charging times are increased.

The second main finding is the fact that the flow rate, $Q$, has little effect on the charging times. It was expected that, when increasing the flow rate, the convective heat transfer co-efficient between the HTF and the ice capsules would greatly increase. However, even after doubling and tripling the flow rate from $Q_1$ to $Q_2$ and $Q_3$, the overall charging times lowered, but not by any significant amount. This suggests that the convective heat transfer coefficient between the capsules and the surrounding HTF is relatively unaffected by changes in flow rates. The effects of flow rate on other system properties, including efficiency and destroyed exergy, will be more apparent, but will be discussed in more detail in the next few sections.

The last note to discuss when assessing the charging times is the effect of geometry. It can be seen above that the fastest solidification times occurred with the

cylinder with aspect ratio of 8, followed by the slab capsules with aspect ratios of 8 and 5, the cylinder with aspect ratio of 5, the spherical capsule, and lastly the cylindrical and slab capsules with aspect ratios of 2. This effect points out an important note about surface area when dealing with convective heat transfer. The capsules which have the least amount of surface area – namely the cylindrical and slab capsules with low aspect ratios – have the least desirable heat transfer characteristics. Since the heat transfer between any two bodies depends on the temperature difference (addressed above) and the area connecting the two bodies, it is expected that this phenomena occur. The capsules which have the higher aspect ratios, including the spherical capsules, have a much higher amount of surface area for the heat energy to transfer into the HTF, and this results in the lower charging times.

### 5.2.2 Energy Efficiency

One of the more important articles to be addressed following numerical computations is the overall energy efficiency. However, before assessing their values, a few remarks must be made. Firstly, it was noticed that the energy efficiencies are extremely high; all efficiency values, regardless of geometry, inlet HTF temperature or flow rate, are well above 99%. Though these values are indeed quite high, they are certainly not unexpected. The energy efficiency is, by definition, the ratio of the desired to the required energy amounts. However, the difference between these two values is a sole result of the viscous dissipation in the fluid. This value, which is analogous to a pressure loss within the fluid, is certainly important when designing systems like these; however it is quite insignificant when compared to the thermal energy stored in the water and in the PCM, which is why the energy efficiency values are as such. This is the reason why the efficiencies were normalized; so that a closer inspection of the energy efficiency differences can be observed.

It is also important to note that though real-world systems may have a lower efficiency value, due to heat leakage into the storage tank from the ambient. However, the flow fields inside the system, and the resulting head loss due to interior flows, are equally important to designers. This is why the comparisons are made in this study; to

determine the best possible conditions for storage and retrieval of latent thermal energy when the capsule tank is sufficiently insulated. Keeping this in mind, the normalized energy efficiencies of each charging case can be seen in Figures 5.7 to 5.9 for the flow rates of $Q_1$, to $Q_3$, respectively.

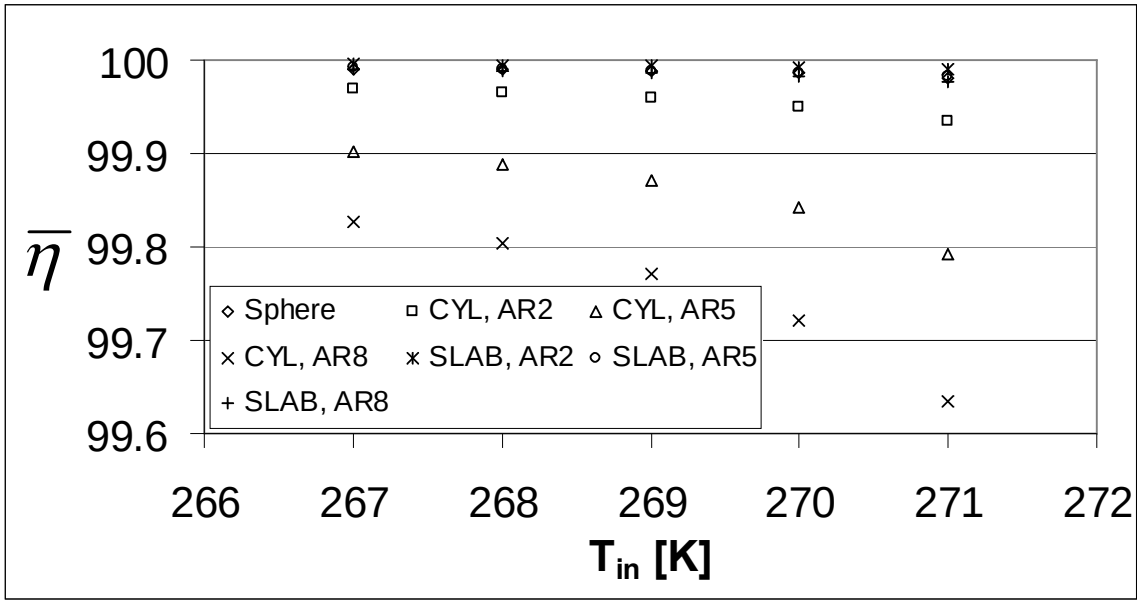


**Figure 5.7: Charging normalized energy efficiencies; flow rate $Q_1 = 8.7\times10^{-4}$ $m^3/s$.**

Other than the very high efficiencies resulting from these solutions, it should be apparent that the flow inlet temperature has a relatively large effect on the normalized energy efficiency. Since, as explained earlier, the energy difference depends completely upon the viscous heating attained in the fluid, it should be expected that the geometries with the fastest moving fluid should experience the most pressure energy loss. To better understand these phenomena, Table 5.2 lists the inlet velocities according to geometry and flow rate. From these values, it is immediately apparent that the geometries and flow rates which give the highest velocity values will give rise to the lowest energy efficiencies. This is due to the viscous heating effect.

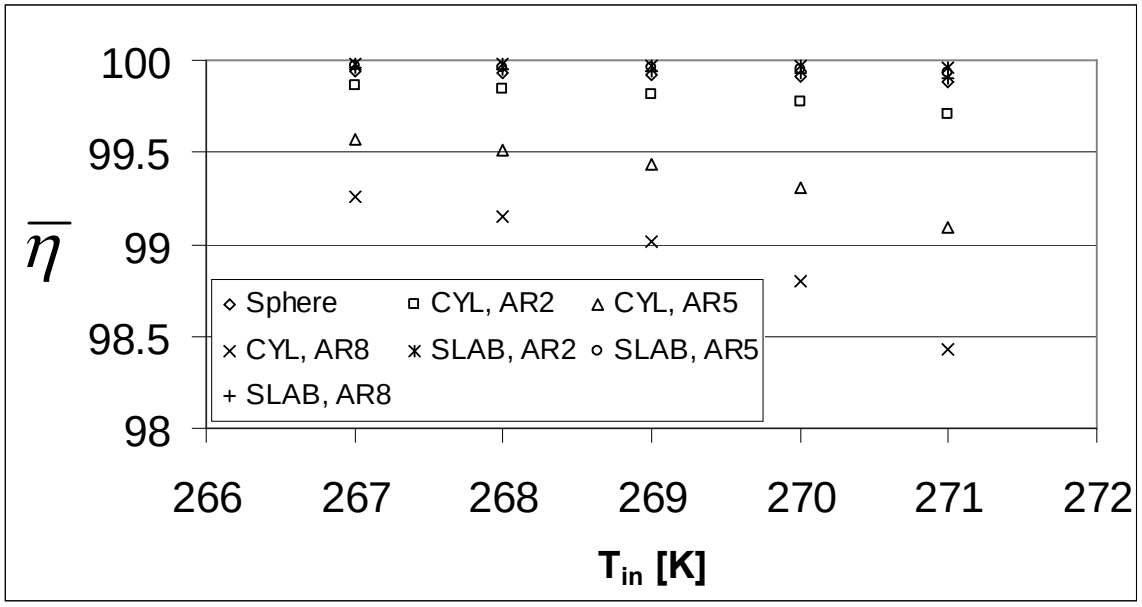


**Figure 5.8: Charging normalized energy efficiencies; flow rate $Q_2 = 1.74\times10^{-4}$ m$^3$/s.**

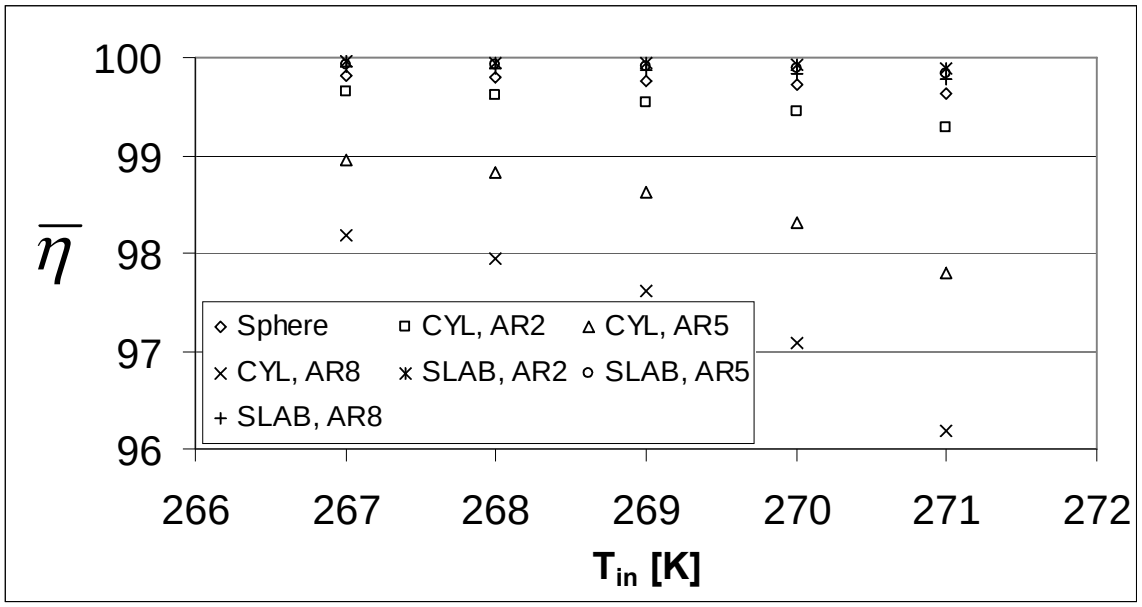


**Figure 5.9: Charging normalized energy efficiencies; flow rate $Q_3 = 2.61\times10^{-4}$ m$^3$/s.**

The viscous heating effect, sometimes called viscous dissipation, is a result of shear stresses in the fluid domain. When there are velocity differences in a fluid, there will always be friction between adjacent molecules traveling at different speeds, which give rise to heat generation. However, due to the first law of thermodynamics, heat cannot simply be generated without an energy transfer across system boundaries; it must be transferred from existing energy sources. This is why the pressure decreases along any duct or pipe flow. To account for the (however minute) rise in temperature of the

flowing fluid, pressure energy must be sacrificed. In the same way, pressure energy cannot simply be "lost", since the energy balance equations must be conserved.

**Table 5.2: Inlet velocities for the various geometries, according to flow rate.**

| | $Q_1$ Velocity (m/s) | $Q_2$ Velocity (m/s) | $Q_3$ Velocity (m/s) |
|---|---|---|---|
| Sphere | 0.05 | 0.1 | 0.15 |
| Slab2 | 0.042269 | 0.084539 | 0.126808 |
| Slab5 | 0.049194 | 0.098388 | 0.147582 |
| Slab8 | 0.051605 | 0.10321 | 0.154814 |
| Cyl2 | 0.094487 | 0.188973 | 0.28346 |
| Cyl5 | 0.156506 | 0.313012 | 0.469519 |
| Cyl8 | 0.200534 | 0.401069 | 0.601603 |

So, the pressure energy must be converted into heat energy. For faster moving flows, this shear stress becomes much larger, just as brake pads on an automobile develop more frictional heat during high-speed stops. It should be noted that the frictional heating does depend somewhat on the geometry of the flow as well; for ducts or flow channels which are highly irregular and change the momentum of a fluid considerably, such as pipe elbows or valves, the velocity gradients and hence, frictional heating, plays more of a role. However, in inspection of Table 5.2, it can be ascertained that the viscous heating effect relies more on fluid velocity than its geometry. This is why the geometries with the highest velocities, namely the cylinders with aspect ratios of 5 and 8, achieve the most viscous heating and hence, the lowest energy efficiencies.

Another interesting aspect of Figures 5.7 to 5.9 is that the spherical capsules experience a relatively high energy efficiency value, even though the capsule orientation is the most complicated. With a highly irregular flow field, one may expect the viscous dissipation effect to be greatest in the spherical regime, but this is not the case. The reason for this can be attributed to reduced drag effects due to swirling motion within the HTF.

This swirling effect is simply the effect of circular HTF motion in the deeper pockets of the HTF domain. Since the spherical domain sees two such areas where the

flow area radically increases (namely, the inlet and outlet to the capsule control volume), there are flow swirl effects captured in these recesses. To get a more visual interpretation of this effect, a velocity pathline plot was created using FLUENT post-processing techniques, and can be seen in Figure 5.10 for a lengthwise cross-section of the fluid.

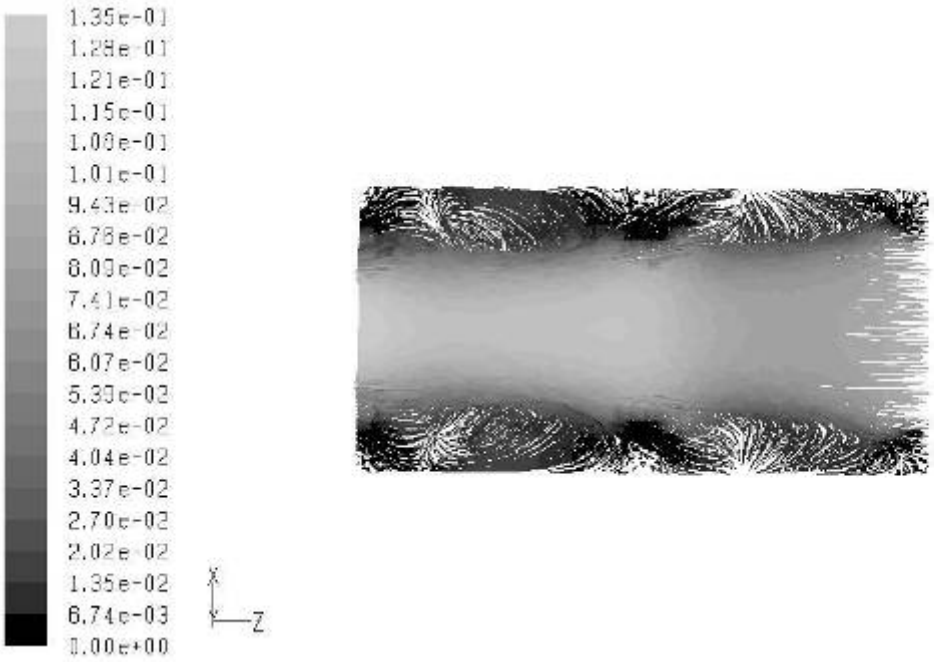


**Figure 5.10: Velocity pathlines for the spherical geometry, in m/s.**

In the above figure, the darker areas represent areas of low velocity, while the lighter areas represent places of high velocity. It can clearly be seen by the streaks that a sort of circular flow motion exists adjacent to the flow, which is occurring from right to left in Figure 5.10. Along the inlet and outlet to the capsule control volume, on top and on bottom, small curved particle pathlines are noticed, which happen to be located at the thin spaces between the spherical capsules. This effect can only be explained by the swirling motion of the HTF in these pockets. These tiny eddy currents serve to reduce viscous generation by eliminating the no-slip wall condition, as well as to conduct heat transfer from the HTF to the capsules. Since the velocity gradients along these swirl areas are not nearly as great as if there were a no slip wall, the viscous dissipation developed drops drastically, which raises the overall energy efficiency. It is for this reason why the spherical geometry experiences much higher efficiency values than one might expect.

It can also be seen from the efficiency figures that the inlet HTF also has an effect on the energy efficiency. The reason for this is the effect of inlet HTF on charging times, and the effect of the charging times on the viscous heating values. From the right hand side of equation (4.29), the viscous heating term depends on two factors: the average pressure drop and the overall volume of HTF used in the simulation. Since the volume of heat transfer fluid is simply the product of the charging time and the flow rate, it should be obvious that the lower charging times should give rise to lower viscous heating, and in turn should amount to higher energy efficiencies. This is exactly the case: since the lower inlet temperatures produce much lower charging times, the amount of viscous heating is reduced, which ultimately leads to higher energy efficiencies.

The effect of flow rate on the energy efficiency is similarly explained. Since the viscous heat dissipation depends on the charging time as well as the flow rate, it is straightforward to note that the higher flow rates (which do not lower charging times significantly) produce more viscous dissipation, due to a larger volume of fluid needed to complete charging. This is the reason why the energy efficiencies for the larger flow rates are a few orders of magnitude smaller than the efficiencies for the smaller flow rates. To better visualize this effect, a comparison of energy efficiencies with respect to geometry and flow rate is performed by choosing a single inlet temperature, $T_{in}$ = 271K. This can be seen in Figure 5.11.

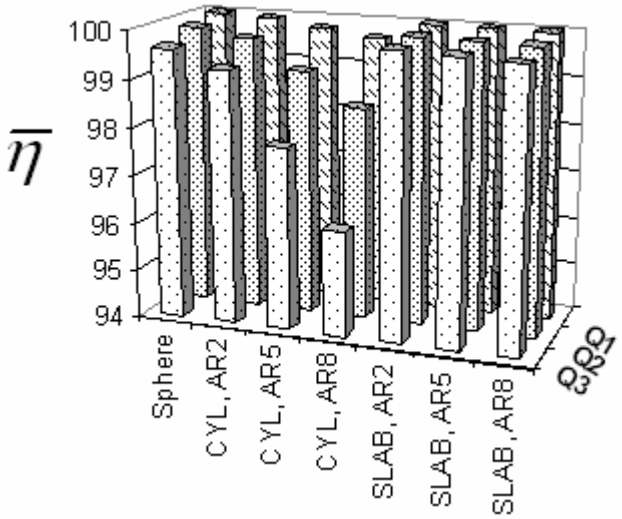


**Figure 5.11: Normalized energy efficiencies with respect to geometry and flow rate ($T_{in}$ = 271K).**

### 5.2.3 Exergy Efficiency

The performance of the system on an exergy basis is now investigated. Exergy analyses are more helpful than energy in a number of ways, since they assess both the quantity and the usefulness of energy. Cold exergy is an excellent example, since exergy treats cold as a useful commodity, due to the inclusion of the effect of ambient conditions.

The term "cold energy" seems somewhat contradictory. The change in energy from a solid to a liquid state in water is inherently negative, while the change in exergy (given a reference temperature higher than the solidification temperature) is actually positive. This is due to the usefulness of the stored energy. If the temperature of the thermal storage strays farther away from the ambient, the change in exergy is positive, since it becomes more useful. Analogously, if its change in temperature moves towards the ambient, the exergy change is deemed negative. This is an interesting, and certainly useful, impact of the exergy analysis. For example, a block of ice at 0ºC, placed in a room at 20ºC, certainly has cooling potential in both the energy and the exergy sense. However, if the room temperature is reduced to 1ºC, the exergy content of the block of ice would greatly decrease, since the potential for the thermal storage has lessened. However, in the energy sense, the block of ice would have the exact same amount of latent energy to receive from the ambient, which can be misleading, since the cooling potential of the block of ice is only useful in the 0ºC to 1ºC temperature range.

It is for this reason why exergy analyses for cold TES is more useful. It can provide much more insight into the actual performance of the system, by treating cold energy as a useful quantity. Thus, the exergy efficiencies, like the energy efficiencies, were calculated for each flow rate, inlet temperature and geometry, and the results can be seen in Figures 5.12 – 5.14, once again grouped by flow rate.

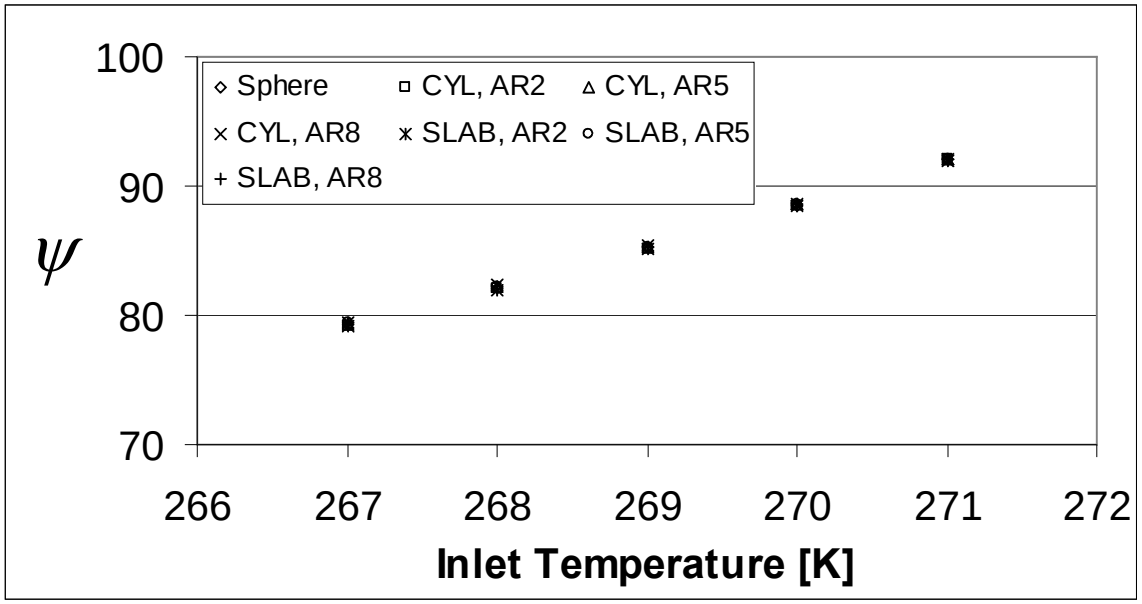


**Figure 5.12: Charging exergy efficiencies, flow rate $Q_1 = 8.7\times10^{-4}$ m$^3$/s.**

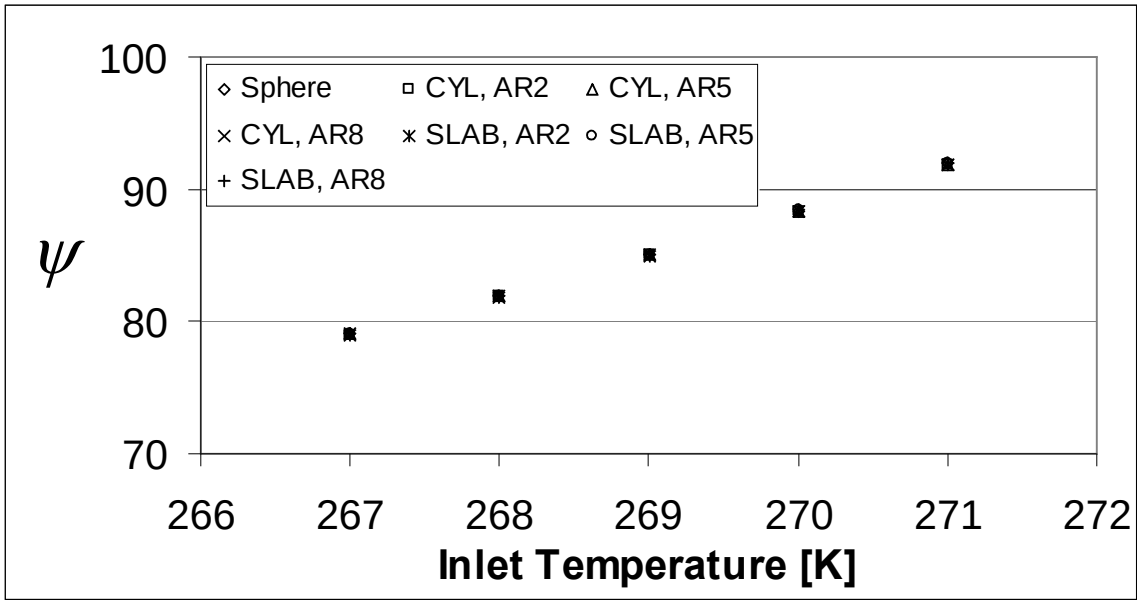


**Figure 5.13: Charging exergy efficiencies, flow rate $Q_2 = 1.74\times10^{-3}$ m$^3$/s.**

There is one immediate and glaring difference between the energy and exergy efficiencies. Although all energy efficiencies are well over 99%, the exergy efficiencies attained are much lower, ranging from around 78% to 93%. There are also a few more observations that can be inferred by the above graphs. The exergy efficiencies increase with increased temperature and the exergy efficiencies appear quite independent of capsule geometry.

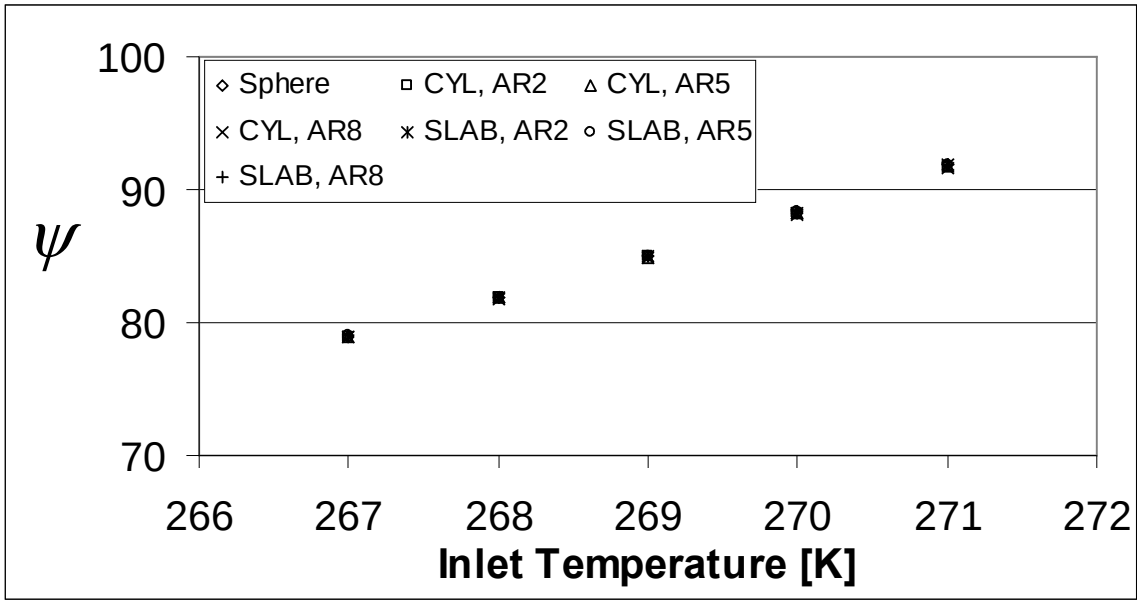


**Figure 5.14: Charging exergy efficiencies, flow rate $Q_3 = 2.61\times10^{-3}$ m$^3$/s.**

The reasons for the much lower exergetic efficiency can be explained once the concept of exergy is fully understood. The exergetic efficiency is by definition the ratio between the desired and required exergy contents. However, these contents are much less than their energy counterparts, due to the inclusion of the ambient temperature [see equations (4.45 – 4.48)]. However, the required and desired exergy values differ for a somewhat different reason than the energy case, and this is solely a result of exergy destroyed. The exergy destroyed from equation (4.51) is a result of both the ambient temperature effect and the entropy generation effect, and it is only after the entropy generation is examined with more scrutiny, that the exergy efficiencies can be explained in full. Before the destroyed exergy is to be explained, though, it is interesting to note the exergy efficiencies when compared by flow rate and geometry, as inlet HTF temperature is kept constant, to ascertain the differences between the geometries and over HTF flow rates. As examples, the charging case is examined at both extremities; with inlet HTF temperatures of 271K and 267K for Figure 5.15 a) and b), respectively.

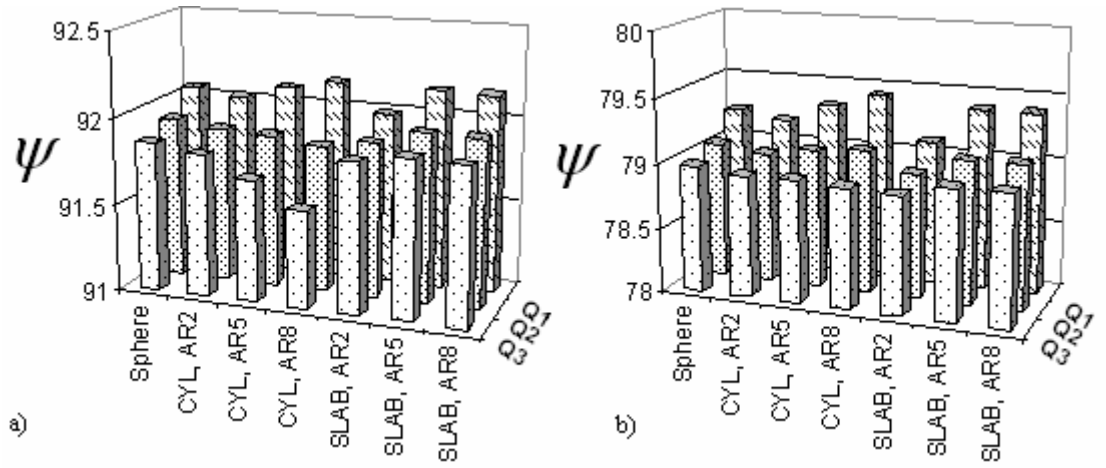


**Figure 5.15: Charging exergy efficiencies according to geometry and flow rate, with inlet HTF temperatures of 271K (a) and 267K (b).**

The above figure demonstrates the differences in exergy efficiencies when both geometry and flow rate are varied. In all cases, the exergy efficiency decreases with increased flow rate. However, when the geometry is varied, the exergy efficiencies do not all follow the same trends across aspect ratios. The above phenomena, as well as the very large effect of inlet HTF temperatures on exergy efficiencies, can be explained more fully once the exergy destroyed terms are examined (next section).

### 5.2.4 Exergy Destroyed

The exergy destroyed is one of the most important analysis tools when determining the performance of a particular process. It is an important indicator of the types and quantities of losses present in a system process. It is also the sole difference between the desired and required exergy contents in the exergy efficiency equation, so it is directly linked to the exergetic efficiency and it can be used to explain all of the differences in the exergy efficiency graphs in Figures 5.12 to 5.15. As briefly stated in section 4.3.2, the exergy destruction occurs from entropy generation, which is a direct result of two separate phenomena: entropy generation from viscous dissipation (see equation 4.54) and entropy generation from phase change and heat transfer to/from the capsules as in equation (4.56). In contrast to the case of energy conservation, exergy is not always conserved. For example, every real-world process incurs some type of irreversibility, and while some can be visualized and interpreted very clearly, other sources of irreversibility

are not so apparent. For example, unwanted heat gain or loss to the atmosphere as a result of imperfect insulation in a system is a source of irreversibility, as are all losses due to friction (and in this case, viscous dissipation). However, there is another source of entropy generation which results in exergy destruction in this scenario. This is a direct result of the heat transfer between the capsules and the surrounding heat transfer fluid. Since entropy is not conserved like energy, every case of heat transfer will involve some entropy generation. This is a corollary of the second law of thermodynamics, which briefly states that the entropy of a closed system is always increasing. In this case, the entropy of the entire system, which includes the control volume *plus* the entire mass of HTF used to cool or heat the capsules, will be greater when the process is completed. This change in entropy between initial and final states is the entropy generation, and it is split into two parts; generated entropy from heat transfer and entropy generation resulting from viscous dissipation. Before these two are compared, they will be lumped together for the purpose of viewing the total exergy destroyed across geometries and inlet HTF temperatures. They can be seen in Figures 5.16, 5.17 and 5.18 for inlet HTF flow rates of $Q_1$, $Q_2$ and $Q_3$, respectively.

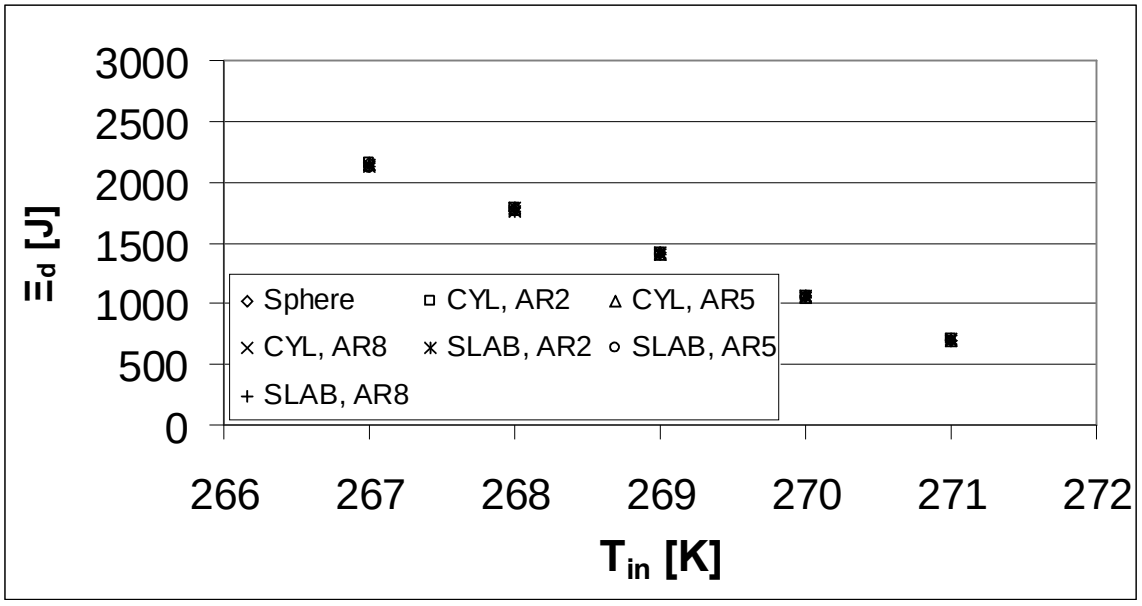


**Figure 5.16: Charging exergy destruction for $Q_1 = 8.7\times10^{-4}$ m$^3$/s.**

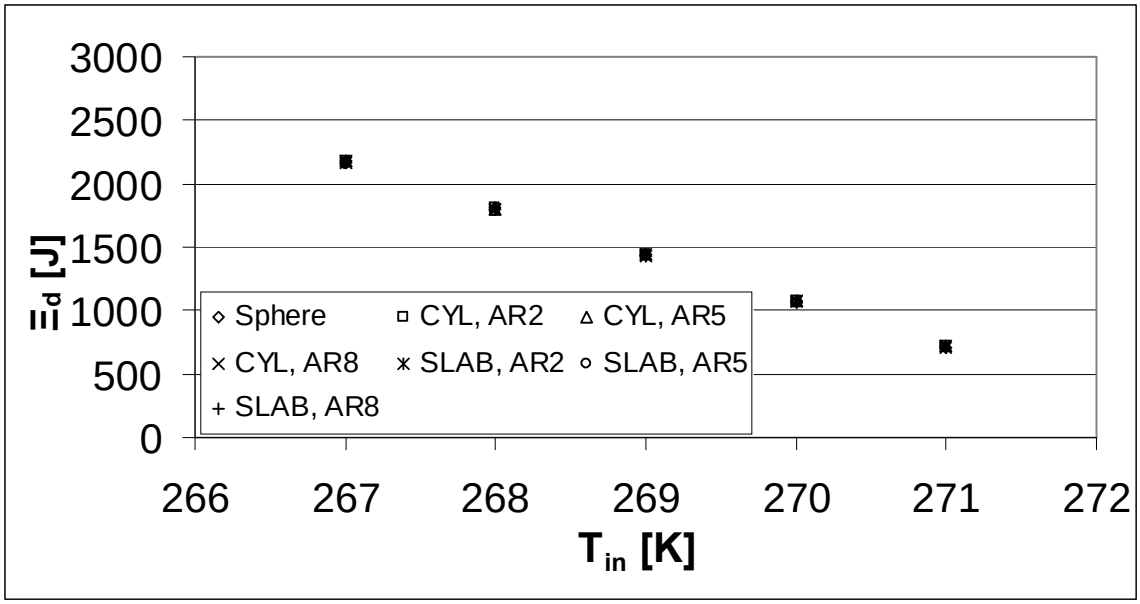


**Figure 5.17: Charging exergy destruction for $Q_2 = 1.74\times10^{-3}$ m$^3$/s.**

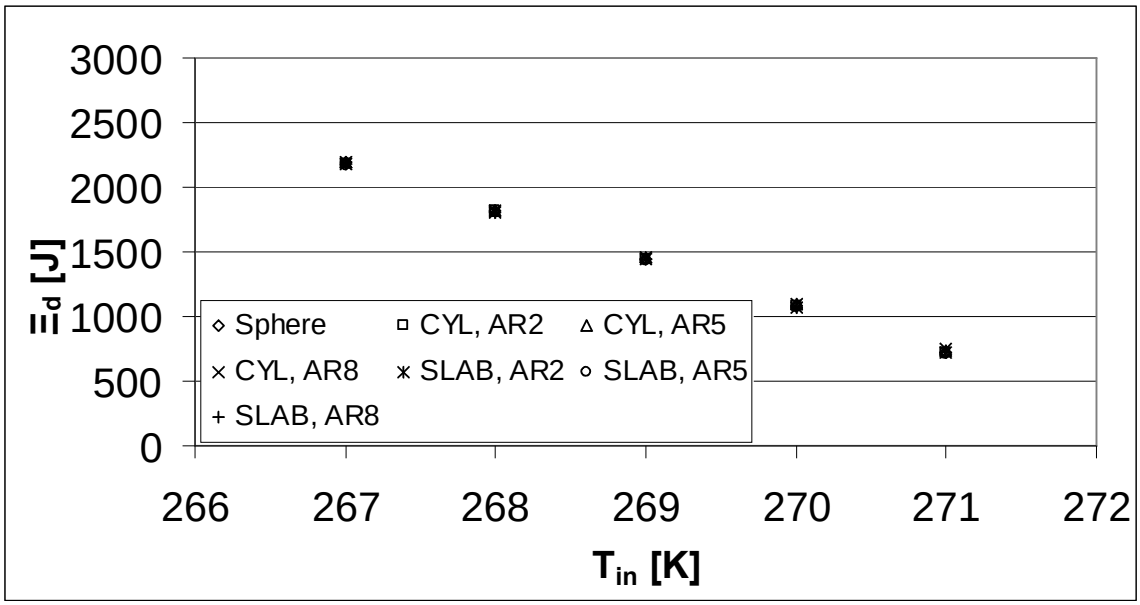


**Figure 5.18: Charging exergy destruction for $Q_3 = 2.61\times10^{-3}$ m$^3$/s.**

In viewing the above figures, two conclusions can be immediately observed. The exergy destroyed increases with increased inlet HTF temperatures, and when holding the inlet HTF temperature constant, the exergy destroyed remains relatively constant across all geometries and inlet HTF flow rates.

The fact that exergy is destroyed more when inlet HTF temperatures are lowered is readily explained, since exergy analyses allow for a closer investigation at the usefulness, and not the overall quantity, of energy. The lower inlet HTF temperatures

will be heated up much more than the higher temperatures, meaning that a larger temperature gradient will be observed. In addition, when the temperature at which the heat transfer is occurring is lowered, more *quality* fluid is used to complete the process, rendering it less efficient. For example, if one wants to freeze a tray of ice cubes, a fixed amount of heat energy must be extracted, whether it is frozen in a conventional freezer, or frozen using a high quality source – such as liquid nitrogen. However, using a very cold substance such as liquid nitrogen to cool some ice cubes will require a much larger loss of quality cold energy (exergy), which is directly proportional to the entropy generation. As a result, less entropy is generated (and less exergy is destroyed) when a conventional freezer is used instead of liquid gas such as nitrogen, making it much more efficient exergetically. This may seem like common sense, but in the world of energy analyses, the two processes could be deemed equally efficient!

As stated earlier, the other glaring aspect of the above figures is that the exergy destroyed does not vary by any marked amount, when comparing different geometries and flow rates. However, it is interesting to compare the exergy destroyed amounts when holding this HTF temperature constant. To explain these small differences, Figure 5.19 shows the exergy destroyed when charging at a HTF temperature of 271K (a) and 267K (b).

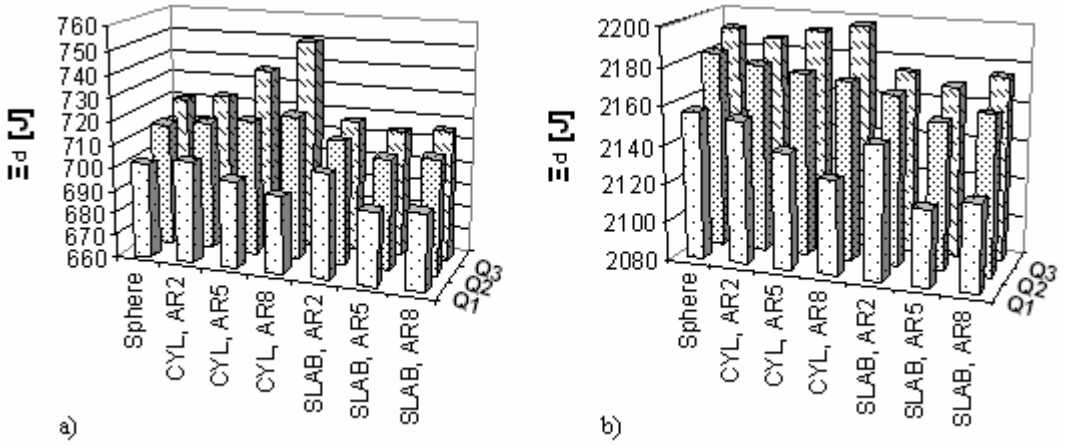


**Figure 5.19: Exergy destroyed during charging according to geometry and flow rate, with inlet HTF temperatures of 271K (a) and 267K (b).**

Since the exergy destroyed has an integral role in the exergetic efficiency, there again should be no surprise that the higher inlet HTF temperature in Figure 5.19a

experiences much less exergy destroyed, and achieves much higher exergetic efficiencies than the case of the lower inlet HTF temperature in Figure 5.19b. However, it is interesting to note that for the case where the inlet HTF temperature is 271K, the highest exergy destroyed is achieved with the cylindrical capsules of high aspect ratio, at the highest flow rate, while the lowest aspect ratio is achieved again by the cylindrical capsule with an aspect ratio of 8, but this time with the lowest flow rate. However, for the case of the lower inlet HTF temperature of 267K, while the highest exergy destroyed content was realized by the cylindrical capsule with an aspect ratio of 8, the lowest amount of exergy destroyed was realized by the slab capsule with an aspect ratio of 5, at the smallest flow rate.

The reasons for the above differences depend on several variables. When the HTF temperature is held constant, the temperature change and total mass of HTF used in equation (4.56) becomes very important to the exergy destroyed as a result of heat transfer. However, in equation (4.54), the bulk fluid temperature and total mass of HTF become more important when assessing viscous dissipation. Thus, as the total amount of exergy destroyed is a result of *both* of these phenomena, the portion of the total entropy generation which arises from viscous dissipation must be assessed. Therefore, to show these comparisons, the same cases as shown in Figure 5.19 are again shown; however this time only the portion of exergy destroyed due to viscous dissipation is shown. This can be seen in Figure 5.19, for the inlet HTF temperature of 271K (a) and 267K (b).

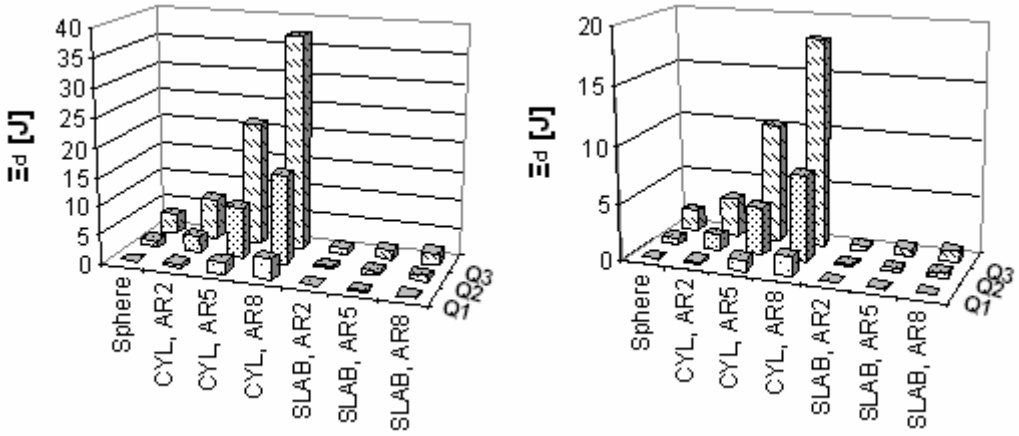


**Figure 5.20: Exergy destroyed during charging which arises from viscous dissipation, for all geometries and inlet HTF temperatures of 271K (a) and 267K (b).**

It can be observed that the amount of exergy destroyed which arises from viscous dissipation or frictional heating is very small compared to exergy destroyed due to heat transfer during phase change in the capsules. This is not unexpected, since there is usually a very small amount of energy loss due to pipe or duct flow when compared to the overall kinetic energy of the field. As a result, the main differences between the destroyed exergy (and hence, exergy efficiency) arise from the entropy generation in equation (4.56), in other words due to heat transfer during the phase change of the capsules.

However, the differences between the exergy efficiencies are quite small. As a result, the exergy destroyed differences are very similar in Figure 5.19. These variations in both the destroyed exergy and exergy efficiencies occur as a result of both the viscous heating effect, as well as small differences in heat transfer entropy generation.

For the most part, the exergy destroyed due to viscous dissipation across all geometries and flow rates is quite small. In Figure 5.20, it is often less than 5 *J*. However, in some cases, as with the cylindrical capsules with higher aspect ratios and flow rates, the viscous heating is not as subtle, and it is the primary reason why these configurations become least efficient at these higher flow rates. However, when the flow rate is slowed considerably to $Q_1$, the destroyed exergy becomes much smaller, so that they become obsolete when discussing the differences between capsule geometry and flow rate.

For these smaller flow rates, which result in the best efficiency values, one of the most important conclusions which can be drawn is the finding of the optimal configuration. Since it is already ascertained that the lowest flow rates are more desirable, the task is now to explain why these differences in destroyed exergy exist.

When observing equation (4.56), it can be inferred that with the inlet HTF temperature held constant, the entropy generated – and hence, exergy destroyed – is a result of two components: the total mass of HTF used in the process, as well as its change in overall temperature. It is an intricate balance of these two values that determines the exergy destroyed. For example, for higher flow rates, the heat transfer coefficient between the capsules and the HTF is increased, but not by any large amount – which can be observed by the relatively constant charging times when compared across flow rates

(see Figures 5.4 – 5.6). This indicates that the total mass of HTF used is increased greatly, overcoming the small decrease in total HTF temperature change. In this case, the mass variable in equation (4.56) is dominant. It is for this reason why the lower flow rates experience lower exergy destroyed; even though the temperature change for the smaller amount of HTF will be greater. This should increase the destroyed exergy, as the total mass of HTF used is still dominant, and results in lower exergy destroyed.

When comparing the destroyed exergy across geometries, however, the same conclusions cannot be made. For some geometries and flow rates, the trend is to increase across increased aspect ratios, while for others the trend is to decrease along the same variables. Furthermore, in some cases, there are optimal values attained with respect to exergy destroyed. For example, the slab capsule with an aspect ratio of 5 results in the most efficient scenario across all flow rates and geometries. This is a result of a very little amount of exergy destroyed due to viscous dissipation (see Figure 5.20), while still retaining a very good heat transfer coefficient, which lowers the total mass of HTF used (as in equation 4.56).

Although the comparisons between exergy destroyed when varying geometry and flow rate are interesting, they are relatively insignificant when compared by inlet HTF flow rate. By comparing Figures 5.16, 5.17 and 5.18, to Figure 5.19, it can be observed that the greatest change in exergy destruction, and hence exergy efficiency, is obtained when varying the inlet HTF temperature. However, these other comparisons are nonetheless important. In the charging scenario, the slab capsule with an aspect ratio of 5 is most efficient, but not by a large amount.

## 5.3.0 Discharging

For the discharging process, the entire process was simulated in like fashion; all processes were run until the liquid fraction $\beta = 1$ everywhere in the PCM. The flow rates and geometries are identical to those used in the charging case, except for one difference; the inlet flow temperatures are changed. Due to the discharging nature of this process, the HTF temperature is above that of the cold capsules, to ensure heat can be properly transferred to the capsules and a subsequent cold flow difference is achieved in the HTF.

For the cases investigated herein, the inlet flow temperature is changed from 275K to 279K, and the effects of the inlet temperature changes are monitored. As with the charging process, the results will be discussed in three sections, the discharging times, the energy efficiency and the exergy efficiency, and similarities to the charging case can be highlighted.

### 5.3.1 Discharging Times

As noted earlier, the discharging times were first recorded, and are defined as the time it takes for the liquid fraction to equal 1 everywhere in the PCM. The results are seen in Figures 5.21 to 5.23 for the same three flow rates $Q_1$, $Q_2$, and $Q_3$, and for the same geometries investigated in the charging section.

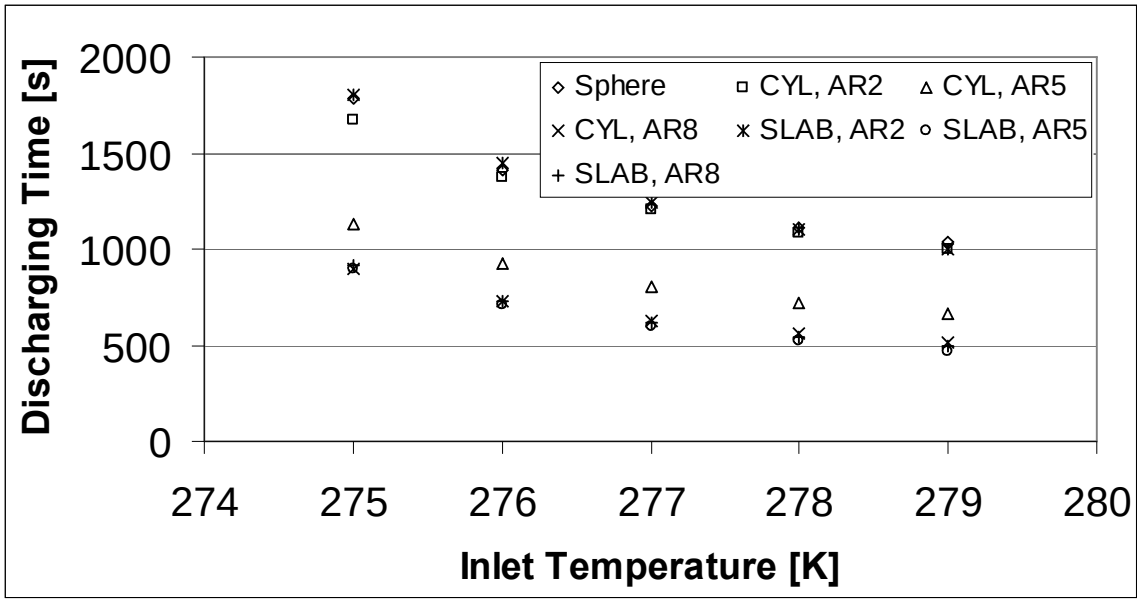


**Figure 5.21: Discharging times for all geometries, with flow rate $Q_1 = 8.7\times10^{-4}$ m$^3$/s.**

In discussion of these figures, many parallels can be drawn from the charging case to explain these discharging times. First, it is quite clear that when the inlet HTF temperature is raised, the discharging times are raised as well. This is due to the same phenomena as seen in the case of the charging capsules; the temperature gradients.

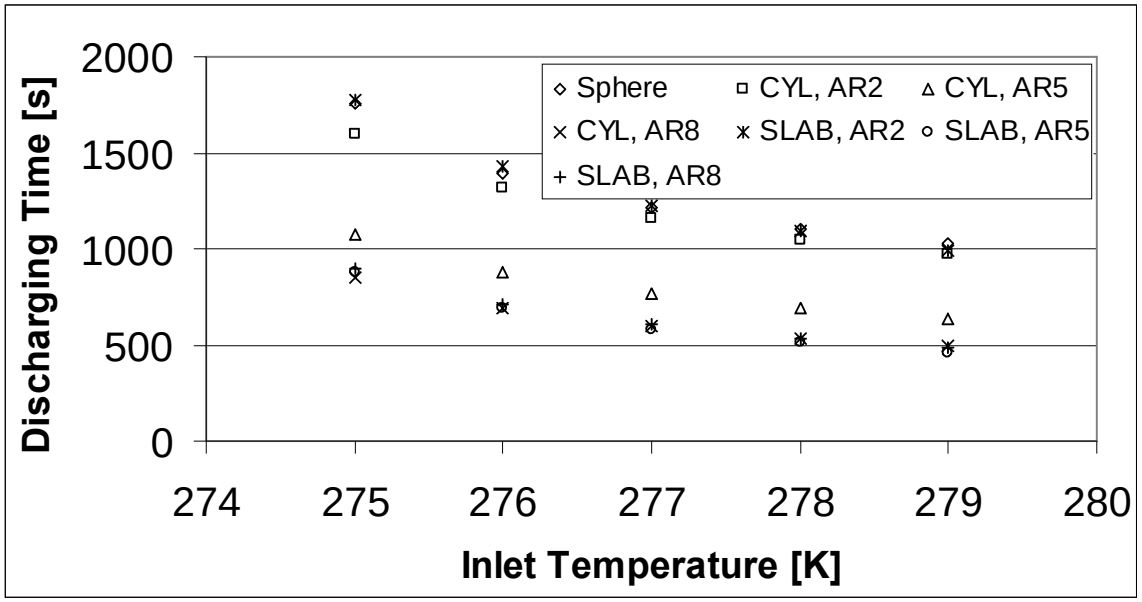


**Figure 5.22: Discharging times for all geometries, with flow rate $Q_2 = 1.74\times10^{-3}$ m$^3$/s.**

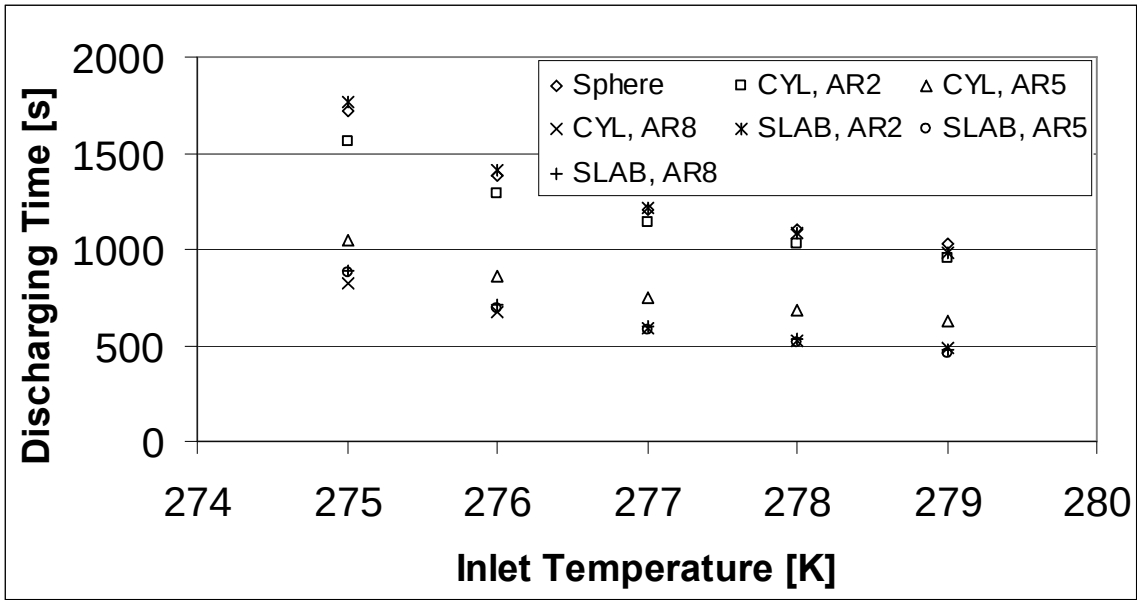


**Figure 5.23: Discharging times for all geometries, with flow rate $Q_3 = 2.61\times10^{-3}$ m$^3$/s.**

Since the heat transfer to the capsules again depends on the difference in temperature between the HTF and the capsules, it is expected that a larger inlet velocity produces smaller charging times. This is because the larger temperature differences make it possible for more heat to transfer to the HTF, which effectively cools and freezes the capsules at a much higher rate. In the opposite fashion, a smaller inlet temperature produces a smaller temperature difference, which is why the heat transfer rate will diminish and subsequently, discharging times will increase.

Another few factors should be pointed out in investigation of Figures 5.21 to 5.23, which again draw close parallels to the case of capsule charging. In specific, two main things can be inferred from the figures; the flow rate again does not have much effect on the discharging time, and once again the capsule surface area has a large effect on discharging time. The reasons for these occurrences are similar to the ones explained in the charging case – the capsules with the largest surface area experience the highest heat transfer rates, while the capsules with the lowest surface area experience the lowest heat transfer rates. Since the overall discharging times depend completely upon the heat transfer rate between the HTF and the capsules, it is understandable why the capsules with the largest amount of surface area, namely the cylinders with high aspect ratio, experience the shortest discharging times.

### 5.3.2 Energy Efficiency

Once again, the energy efficiency was calculated according to the equations previously outlined in Chapter 5. The resulting normalized values are again grouped in terms of inlet HTF flow rate, and are displayed in Figures 5.24 to 5.26 for the $Q_1$, $Q_2$, and $Q_3$ flow rates. In viewing these figures, it is noticed first that the energy efficiency values are again quite high, and this is due to the nature of the defined energy efficiency equation. In equations (4.34) to (4.42), the energy efficiency equations are outlined. This efficiency, similar to the charging case, is simply a ratio of the desired energy output to the required energy input. The difference between these two values, therefore, is the viscous heating term, which again is quite miniscule and draws a close parallel to the charging case. So, for the longer discharging times, more pressure energy is converted into unrecoverable heat energy, which is why the energy efficiencies are decreased for lower inlet flow temperatures. Conversely, for the lower discharging times, which reflect high inlet flow temperatures, the energy efficiencies are much higher.

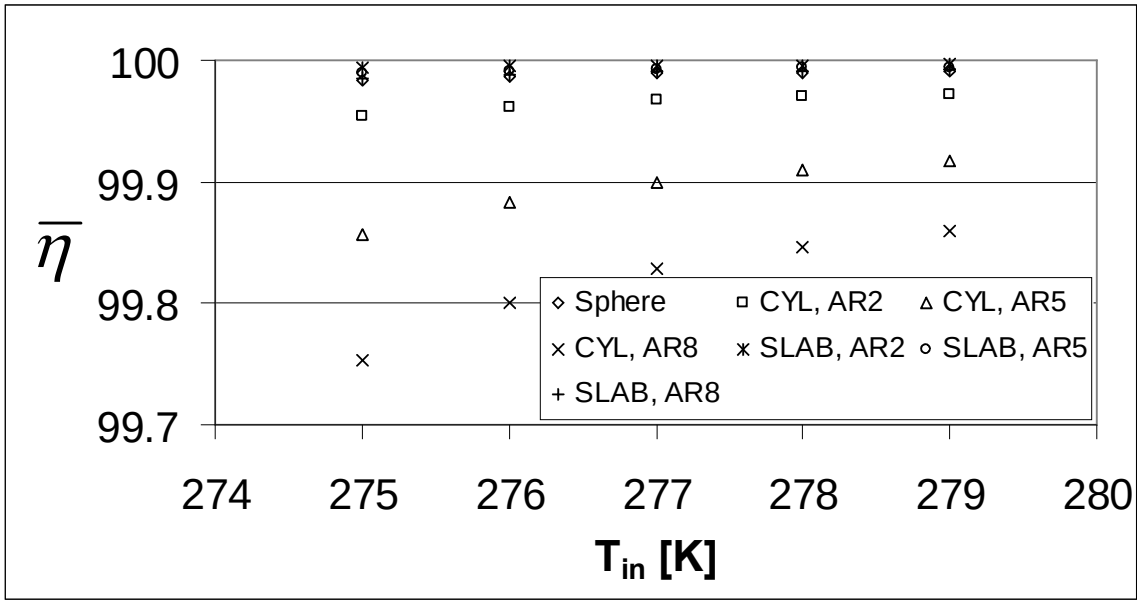


**Figure 5.24: Discharging normalized energy efficiencies; flow rate $Q_1 = 8.7\times10^{-4}$ m$^3$/s.**

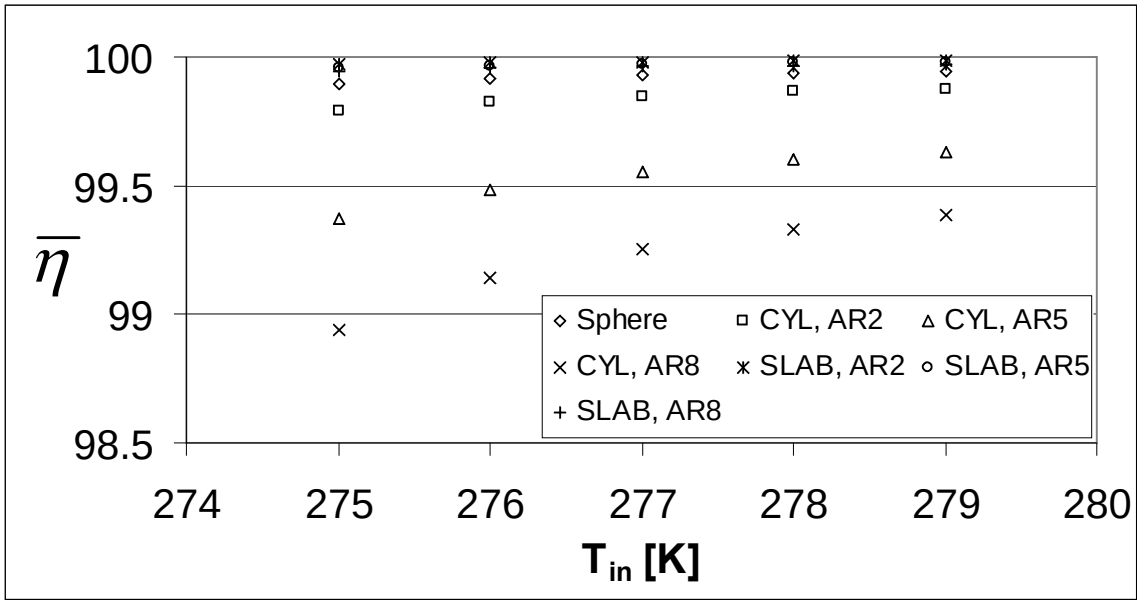


**Figure 5.25: Discharging normalized energy efficiencies; flow rate $Q_2 = 1.74\times10^{-3}$ m$^3$/s.**

Though the flow rate does not have much effect on the discharging times, it does have a larger effect on the energy efficiency. Again, this can be attributed to the viscous heating effect. Since the amount of viscous dissipation depends on the flow rate, pressure drop, and charging time, it is expected that a higher flow rate, which often corresponds to higher pressure drop as well, will produce a larger viscous dissipation value over the discharging process.

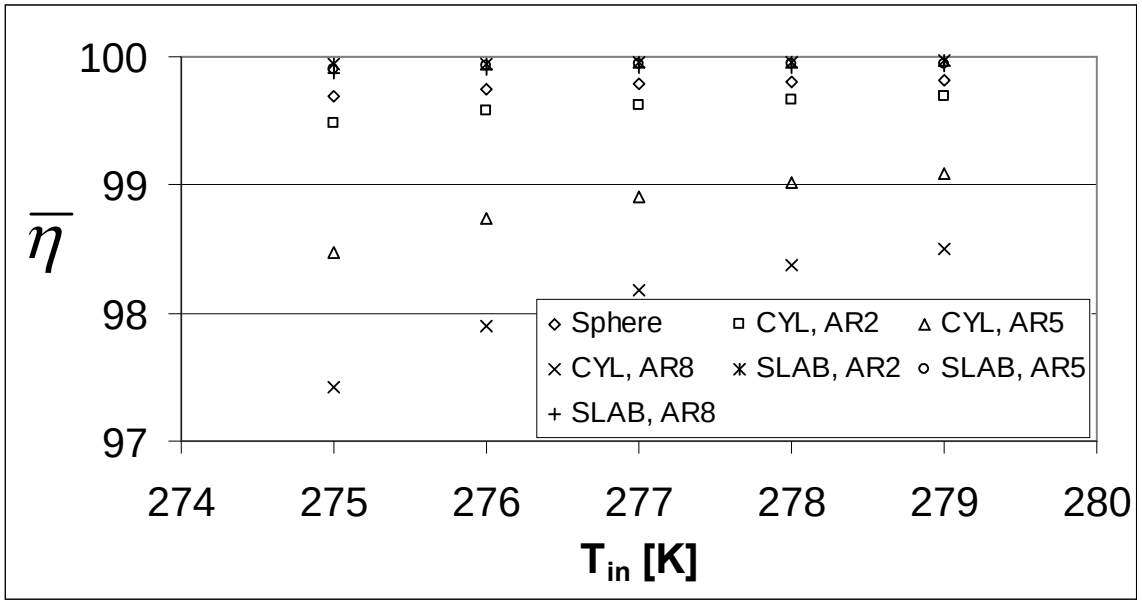


**Figure 5.26: Discharging normalized energy efficiencies; flow rate$Q_3 = 2.61\times10^{-3}$ m$^3$/s.**

This is the reason why the energy efficiency decreases with increased flow rate; the difference in charging time does not make up for the large variation in pressure drop and flow rate, so the net effect is more energy converted from pressure to heat energy.

Comparisons between capsule geometry and energy efficiency for the discharging process are similarly made. Since the main criteria for the energy efficiency is the viscous heat generation, it is a very small pressure drop which is desirable for a high efficiency. For this reason, the slab capsules, which have a uniform surface, experience the highest energy efficiency values, followed by the spherical capsules and lastly the cylindrical capsules in order of aspect ratio.

Once again, a note should be made about the swirling effect of the spherical capsule domain. The reduced skin friction (drag) which was experienced during charging occurred in the same fashion during discharging. For this reason, the discharging efficiencies for the spherical capsules, in both the energy and the exergy sense, were much higher than anticipated.

Now that the flow rate, capsule geometry and inlet HTF temperature effects have been discussed, it is again interesting to compare the energy efficiency across all flow rates and geometries with the inlet HTF temperature kept constant. This is done in Figure 5.27, with the inlet flow rate of $T_{in}$ = 275K chosen as the HTF temperature.

The energy efficiencies during discharging very closely resemble the energy efficiencies during charging, for the same reasons. The geometry and inlet velocity, which greatly impact viscous heating, have the greatest effects on the energy efficiency, which is why the cylindrical capsules achieve the lowest efficiencies, followed by the spherical and lastly the slab capsules, with the slab capsule of aspect ratio 2 being the best geometry energetically.

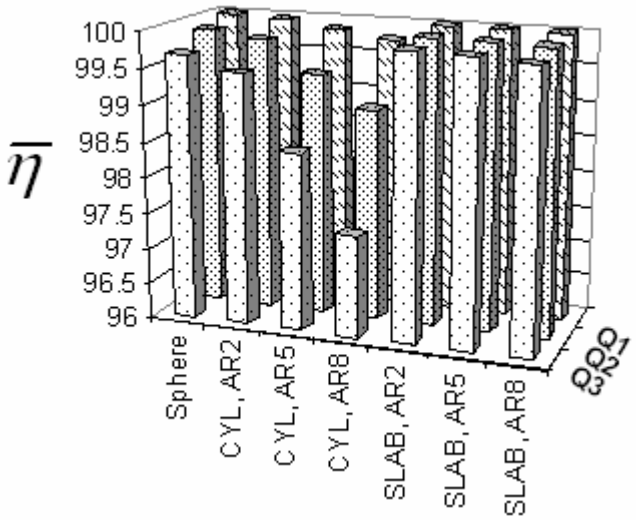


**Figure 5.27: Normalized energy efficiencies with respect to geometry and flow rate ($T_{in}$ = 275K).**

### 5.3.3 Exergy Efficiency

The exergy efficiency for the discharging process, defined by equations (4.45) to (4.68), was monitored for all solutions, and the results are displayed in Figures 5.28 – 5.30 for flow rates of $Q_1$, $Q_2$ and $Q_3$, respectively.

From inspection of the following figures, three main points should be addressed. The exergy efficiencies are once again markedly lower than the corresponding energy efficiencies. The exergy efficiencies decrease with increasing inlet HTF temperatures, and they do not vary by any significant amount when compared across geometry and flow rates.

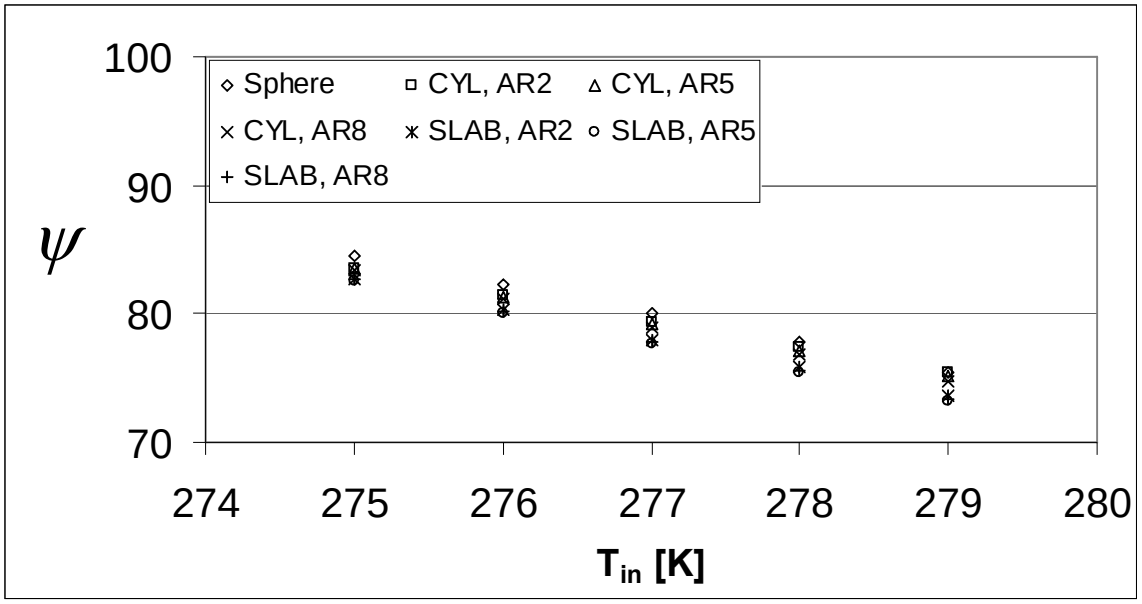


**Figure 5.28: Discharging exergy efficiencies; flow rate $Q_1 = 8.7\times10^{-4}$ m$^3$/s.**

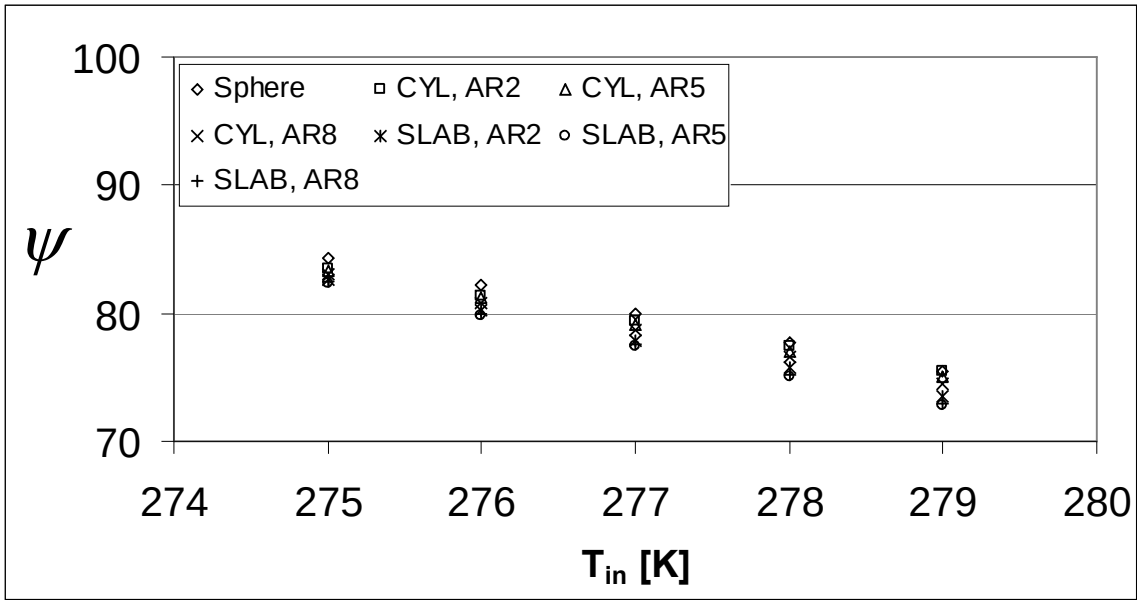


**Figure 5.29: Discharging exergy efficiencies; flow rate $Q_2 = 1.74\times10^{-3}$ m$^3$/s.**

The exergy efficiency values in the case of discharging vary between around 72% and 85%, which is in major contrast to the energy efficiency values, once again all well over 99%. The reasons for these differences were as explained earlier: exergy, unlike energy, is not conserved. For every real-world process, entropy is generated, which in turn means that exergy is destroyed, signifying the unrecoverable exergy lost in the process.

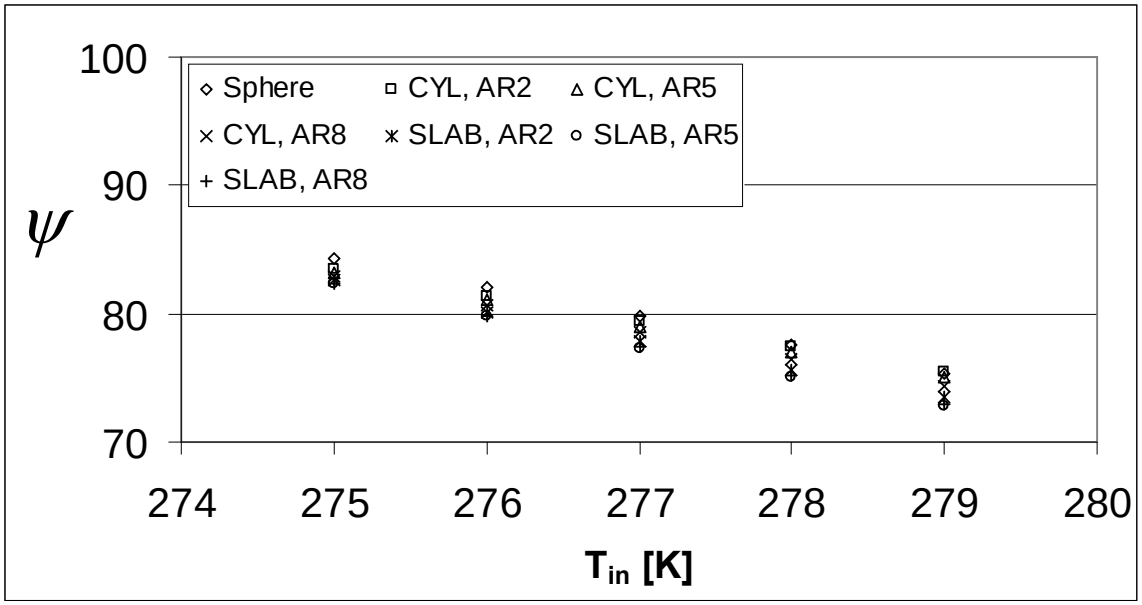


**Figure 5.30: Discharging exergy efficiencies; flow rate $Q_3 = 2.61\times10^{-3}$ m$^3$/s.**

It should be apparent as well that the exergy efficiencies are lower in the discharging case than the charging case (compare the above figures with Figures 5.12 – 5.14). The reason for this is due to the large amount of initial exergy contained in the PCM. During discharging, the PCM initially resides in the form of ice, which is a very high exergy source. However, capturing this high quality source by means of a flowing HTF is somewhat less efficient, due to the temperature at which the heat transfer takes place. Since the inlet HTF must be at a higher temperature than the solidification temperature of the PCM, the exergy flow difference during discharging cannot be as large as the exergy flow difference in charging, due to the nature of the logarithmic equations (4.43) to (4.48). As a result, the discharging case will always experience a lower efficiency than the charging case, when inlet HTF temperatures are similarly different from the solidification temperature.

The exergy efficiency decreases when the inlet HTF temperature is increased, as expected, due to the nature of the exergy analysis. To reiterate, exergy analyses assess both the quantity and the quality of the energy. In the charging case, which was explained earlier, the exergy analysis obtained that a low quality source to freeze the capsules was the most efficient, since it wastes the least amount of quality, cold flow. In this case, the desired outcome of the process is to create a more quality exergy flow

difference, or in simpler terms, a more useful cold flow, resulting from the melting of the capsules. A lower inlet HTF temperature closer to the solidification temperature of 273 K allows for a much greater difference between the inlet and outlet exergy flows, due to the lower temperature at which it occurs. For the higher inlet HTF temperatures, the same temperature difference between the inlet and outlet HTF flows will be realized. Since this HTF change will occur at a much higher temperature – and closer to the ambient, making it less desirable exergetically – the exergy efficiency declines.

Similarly to the charging case, it was found that while the exergy efficiencies do vary somewhat more according to geometry and flow rate than the charging case, these effects are still minor in comparison to the differences realized by changing the inlet HTF temperature. However, in order to inspect these differences with more scrutiny, the inlet HTF is held constant, and the exergy efficiencies can be compared across geometry and flow rate in Figure 5.31 for the inlet HTF temperatures of 275K (a) and 279K (b).

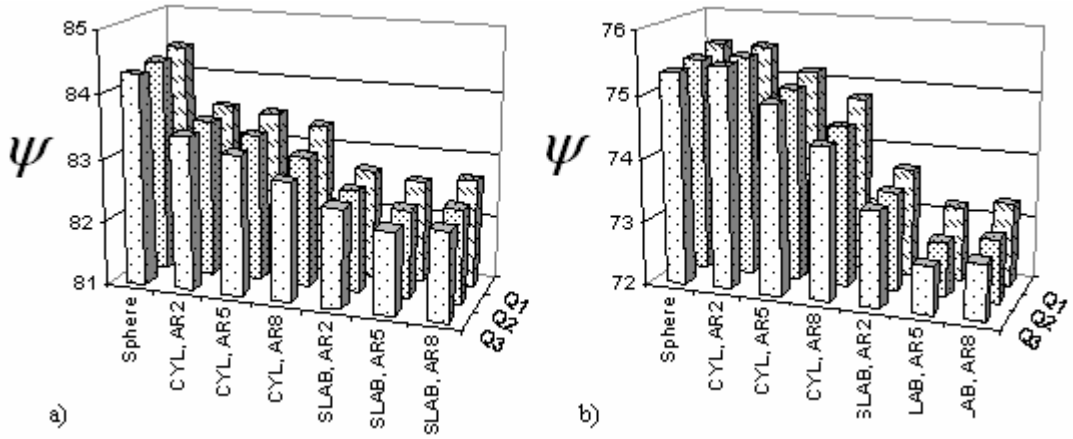


**Figure 5.31: Charging exergy efficiencies according to geometry and flow rate, with inlet HTF temperatures of 275K (a) and 279K (b).**

Figure 5.31 indicates the difference between efficiencies when the HTF inlet temperature is changed dramatically. It can be seen that the efficiency ranges lie between 82% and 85% for the 275K case, while for the case of a 279K inlet temperature, the efficiency range is much lower, between 72% and 76%.

Two other trends in Figure 5.31 are the geometric and flow rate considerations. Geometrically, Figure 5.31 indicates that the spherical geometry is best suited for the lower inlet temperature of 275K, while for the higher inlet HTF temperature, the cylinder with an aspect ratio of 2 is the best suited geometry, followed closely by the spherical

capsules. The least desirable geometry for all cases was the slab capsule with an aspect ratio of 5. This comes in contrast to the charging case, where the slab capsule with an aspect ratio of 5 resulted in the most efficient geometry. In addition, the effect of flow rate on efficiency was very similar to the charging case. When the flow rate is increased, the efficiency decreases in all cases. The reasons for these phenomena are again quite complicated, and they are better explained with regards to the exergy destroyed for the discharging case. For this reason, the explanation for the differences in efficiency across geometries and flow rates is left until the next section, since the destroyed exergy gives a better overall scope of the types and magnitudes of system losses.

### 5.3.4 Exergy Destroyed

The destroyed exergy for all geometries, flow rates and inlet HTF temperatures were recorded in the same fashion as the charging case, and the results can be seen in Figures 5.32 to 5.34 for flow rates of $Q_1$, $Q_2$ and $Q_3$, respectively.

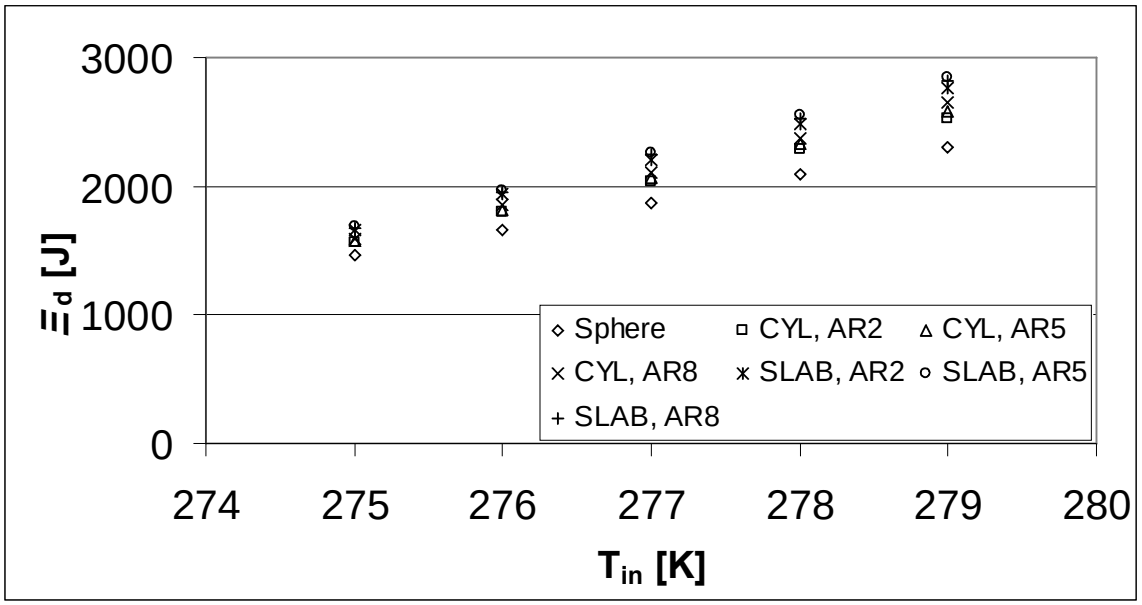


**Figure 5.32: Discharging exergy destruction for $Q_1 = 8.7\times10^{-4}$ m$^3$/s.**

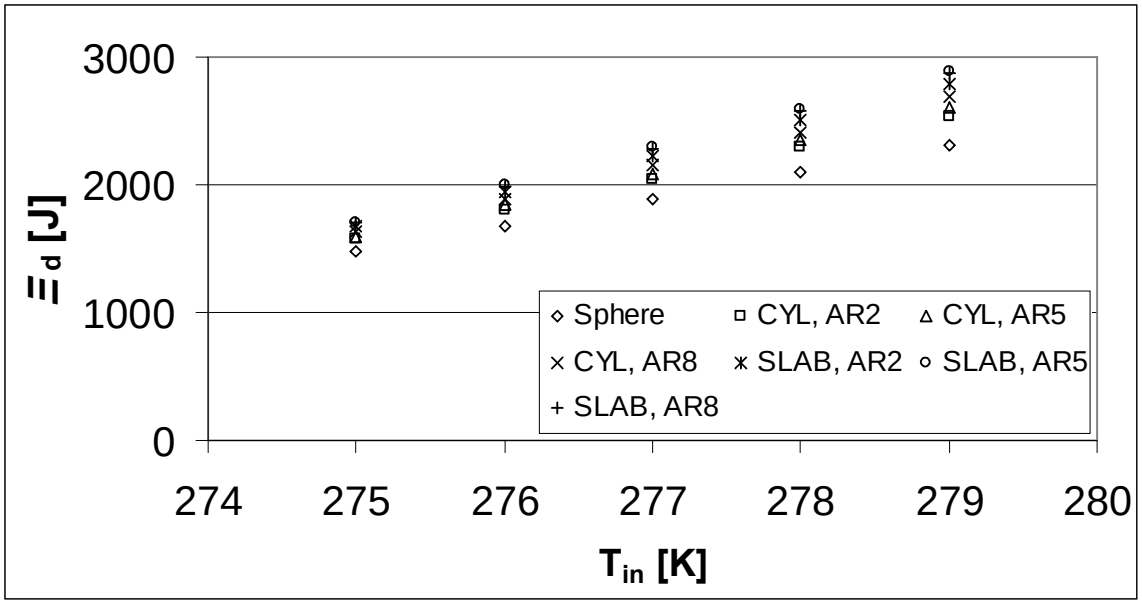


**Figure 5.33: Discharging exergy destruction for $Q_2 = 1.74\times10^{-3}$ m$^3$/s.**

Analysis of the destroyed exergy provides a very helpful insight into system behavior, and the types and magnitudes of losses in the system. Since all real world systems incur some type of loss, there is a considerable amount of destroyed exergy in the discharging process. In this case, it varies between about 1400*J* to almost 3000*J* for a single capsule during discharging.

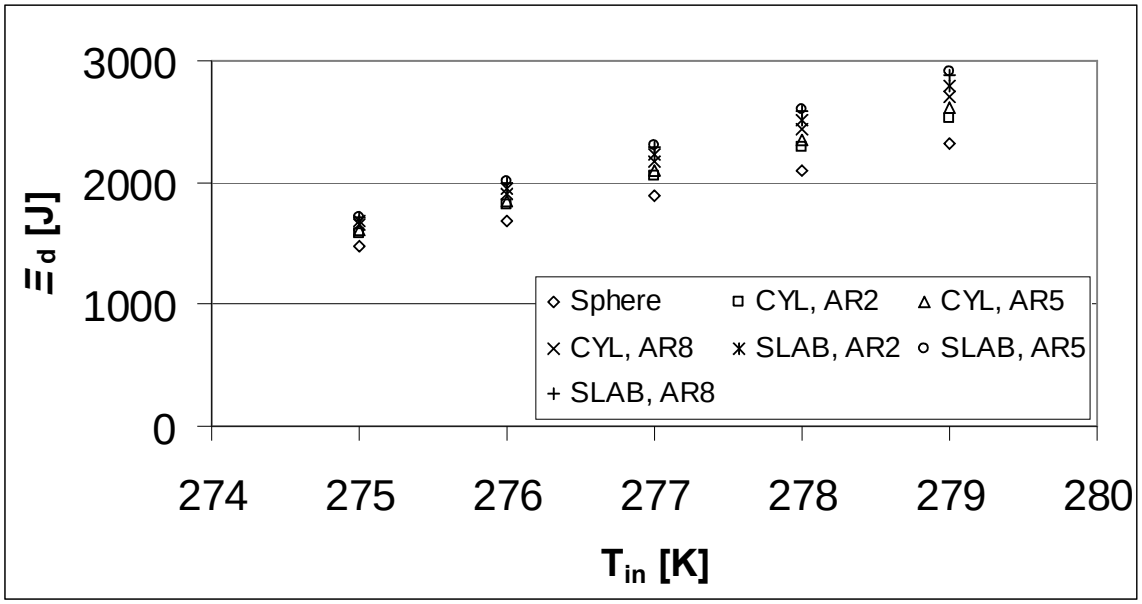


**Figure 5.34: Discharging exergy destruction for $Q_3 = 2.61\times10^{-3}$ m$^3$/s.**

Similar to the charging case, all destroyed exergy decreases when the inlet HTF temperature strays farther from the solidification temperature, and the destroyed exergy contents are quite similar when compared across geometry and flow rate.

When compared by inlet HTF temperature, it should be fairly straightforward why the destroyed exergy increases with increasing temperature. For the same reasons why the exergy efficiency decreases, the destroyed exergy will increase. In other words, as the inlet HTF temperature is increased, the potential for a very good quality flow difference is lessened, since the inlet flow quality (or exergy content) is lower than if it was closer to the solidification temperature of 273K. For example, consider two similar cases: the first, melting 1kg of ice, initially at 273K (0ºC), in 100kg of water, initially at 293K (20ºC); the second, melting the same 1kg of ice, at the same initial temperature, in 100kg of water, this time at an initial temperature of 278K (5ºC). A quick calculation shows that the entropy generation – and hence, exergy destroyed – is more than three times greater in the first scenario. This is the main reason why ice cubes are used primarily in low temperature cooling, since for higher temperature cooling it becomes very inefficient exergetically. However, in the energy case, there is very little separating the above two cases and they could be considered equally efficient, which can be misleading.

As mentioned, there are only minor differences between exergy destroyed and exergy efficiency when viewed across varying geometry and flow rate. However, these differences are nonetheless important, and they are better seen when holding the inlet HTF temperature constant. For this purpose, the destroyed exergy for all geometries and flow rates is shown in Figure 5.35 for inlet HTF temperatures of 275K (a) and 279K (b).

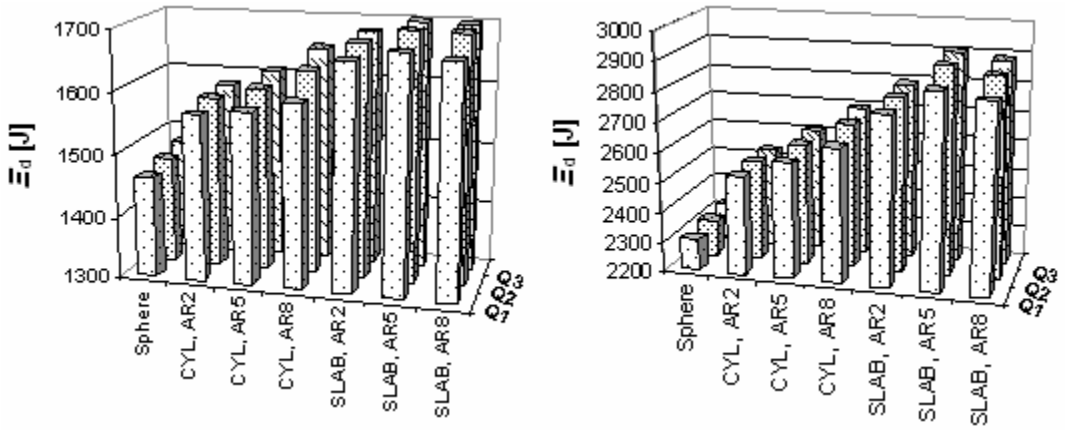


**Figure 5.35: Exergy destroyed during discharging according to geometry and flow rate, with inlet HTF temperatures of 275K (a) and 279K (b).**

It can be seen in Figure 5.35 that the sphere clearly has the least amount of exergy destroyed. This is mirrored in Figure 5.31, since the spherical capsules are the most efficient for the charging case, and very close to the most efficient for the discharging case. The reasons for this can be better understood once the entropy generation and exergy destroyed equations in (4.51) through (4.61) are consulted. In the case of charging, the mass variable in equation (4.56) was found to be dominant, and there is no difference in the case of discharging. Therefore, capsule geometries which provide the least amount of mass to collect the thermal exergy will destroy the least amount of exergy and hence, attain maximum exergy efficiencies. Thus, the geometries which have the most desirable heat transfer characteristics, namely the cylindrical and spherical capsules, will use less mass of HTF for discharging. They are more desirable exergetically. Conversely, the slab capsules, which have comparatively poor heat transfer characteristics, will use more mass of heat transfer fluid and attain higher exergy destruction and lower efficiency values. It is also for this reason why increasing the flow rate has a negative effect on efficiency and destroyed exergy; when the flow rate is increased, the total HTF mass increases, which impacts the system in the same way.

Another interesting aspect when comparing the exergy destroyed in Figure 5.35 with the exergy efficiency in Figure 5.31 is the fact that for the inlet HTF temperature of 279K, the spherical capsules clearly have the least amount of destroyed exergy, but when viewing the efficiency, they are not the clear favorites. Besides having good heat transfer characteristics, the cylindrical capsules also have a relatively large amount of PVC

surface area, so more exergy must be spent on heating this PVC domain. In other words, the greater the surface area of the capsule, the more energy must be expended in heating up the PVC portion of the domain, which creates a thermal resistance. Thus, for the cylinders with the high aspect ratios, even though there is a very good heat transfer rate from the HTF to the capsules, a large amount of heat must be used to first heat up the PVC capsule walls, which also provide some thermal resistance, and hence the destroyed exergy will increase. But, for the cylindrical capsules with a small aspect ratio, this effect is negligible, and as a result they become almost as efficient as the spherical capsules.

However, the issue of viscous dissipation still should not be neglected.

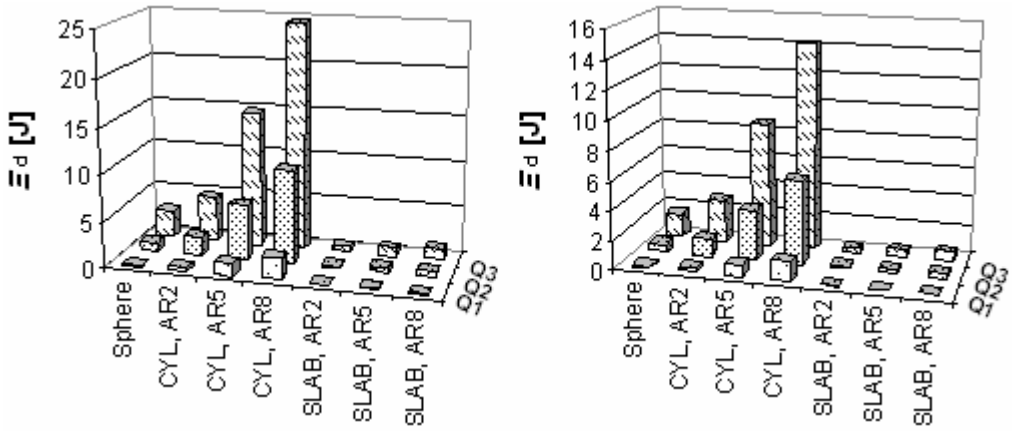


**Figure 5.36: Exergy destroyed during charging which arises from viscous dissipation, for all geometries and inlet HTF temperatures of 271K (a) and 267K (b).**

In order to more fully explain the differences in destroyed exergy when viewed across geometries and flow rates, the exergy destroyed due to viscous dissipation only – as in equation 4.54 – is presented in similar fashion as in Figure 5.36.

One observation inferred from Figure 5.36 is that the destroyed exergy actually increases with increased inlet HTF temperature. For the total exergy destruction, the effect is exactly opposite, so it could seem counter-intuitive that the two modes of exergy destruction act in opposite ways with regards to changing the inlet HTF temperature. However, from inspection of equation (4.54), it is straightforward to explain. When the generated entropy of equation (4.54) is multiplied by the ambient temperature as in equation (4.51), the resulting value is the heat generated by the viscous dissipation, multiplied by the ambient-to-bulk fluid temperature ratio. Since this temperature ratio is

much higher when the inlet HTF temperature (and hence, bulk fluid temperature) is lower, it results in a larger amount of exergy destroyed. This effect far outweighs the larger amount of heat generation which would normally result from a higher discharging time in the lowered inlet HTF temperatures.

Another similarity exists when comparing the viscous dissipation in the charging and discharging modes. This is the very small part that viscous dissipation plays in the overall destroyed exergy quantities. It is interesting to note that the most obvious form of irreversibility, namely frictional heating in the HTF medium, is the least important when performing exergy analyses. It is only when a exergy and entropy balance is performed that the proper modes and quantities of losses can be evaluated and assessed.

## 5.4 Effect of Reference Environment

Now that the energy and exergy efficiencies, as well as the exergy destruction contents, have been discussed, the effect of the reference environment must be discussed with equal scrutiny. The reason is to determine what, if any, effect the reference environment has on the efficiency. The reference temperature should have a large effect on the overall performance of the system, since it arises directly because of the reference temperature (which is normally very hot in cold TES applications), when there is a need for space cooling. In order to determine the effects of the reference temperature on energy and exergy efficiency for the charging processes, the reference temperature was varied from 275K to 320K, in increments of 5K, and the resulting efficiencies were tabulated as in Figure 5.37. The spherical geometry, with a flow rate $Q_3$, was chosen, along with the two inlet HTF temperature extremes; namely 267K and 271K.

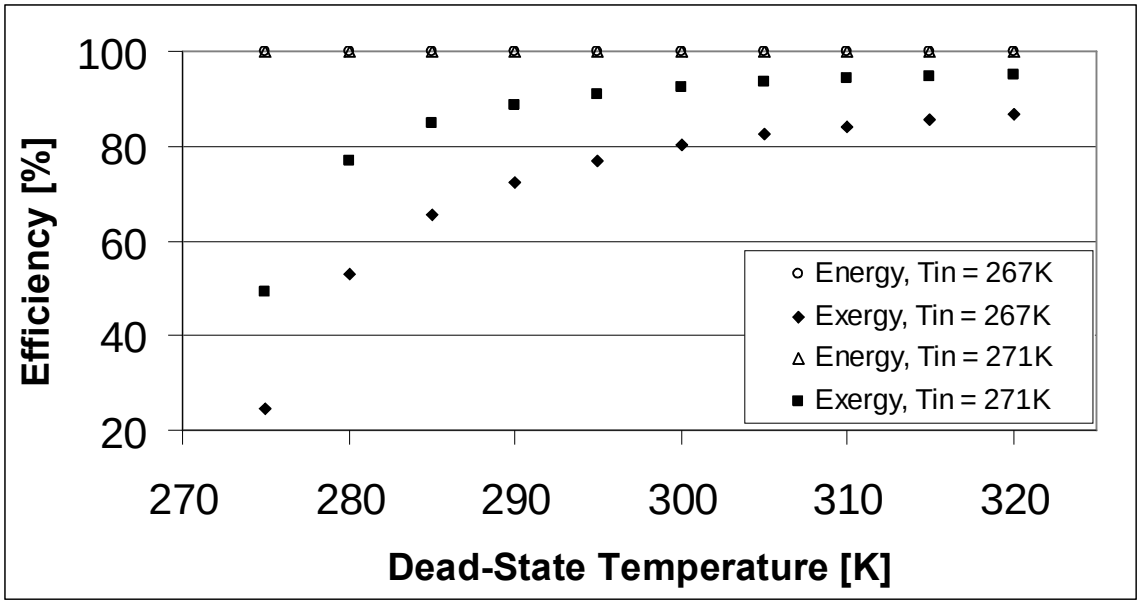


**Figure 5.37: Effect of dead-state temperature on energy and exergy normalized efficiencies, for the spherical geometry while charging, with flow rate $Q_3 = 2.61\times10^{-3}$ m$^3$/s.**

One aspect of Figure 5.37 is the fact that the energy efficiency is unaffected by dead-state temperature. This is a result of the independence of the energy analyses on the ambient conditions. However, in cold TES exergy analyses, the reference temperature is actually very important, since it governs the potential of thermal storage. The above figure accurately reflects this, and as dead-state temperatures increase, the exergy efficiencies increase along with it. This is due to the fact that the stored exergy content becomes much larger for larger dead-state temperatures, while the destroyed exergy content (see Figure 5.39) is largely unaffected.

The effect of dead-state temperature on the efficiencies of the discharging processes is explained analogously. The exergy destroyed content in Figure 5.39 remains largely unaffected by the change in dead-state temperature; however the amount of latent exergy stored in the PCM is greatly increased with increasing dead-state temperature. To show these effects, once again the spherical geometry was chosen, with a flow rate $Q_3$, and the extremities of temperatures used, namely inlet temperatures of 275K and 279K, are shown in Figure 5.38.

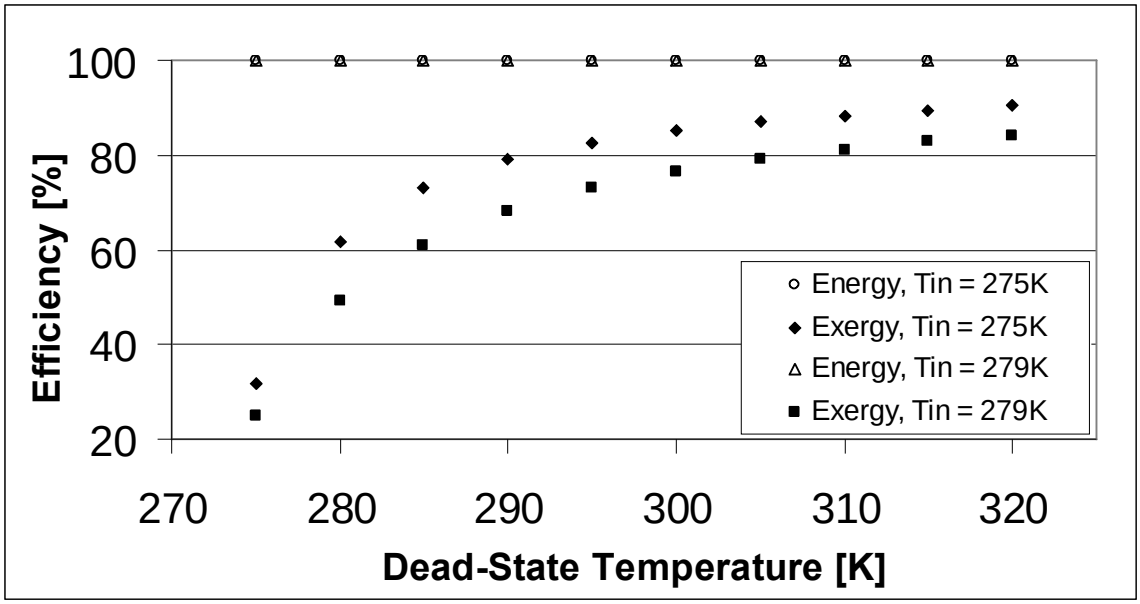


**Figure 5.38: Effect of dead-state temperature on energy and exergy normalized efficiencies, for the spherical geometry while discharging, with flow rate $Q_3 = 2.61\times10^{-3}$ m$^3$/s.**

The variations in exergy destroyed, which have a large role in the exergy efficiencies, are now examined as in Figure 5.39.

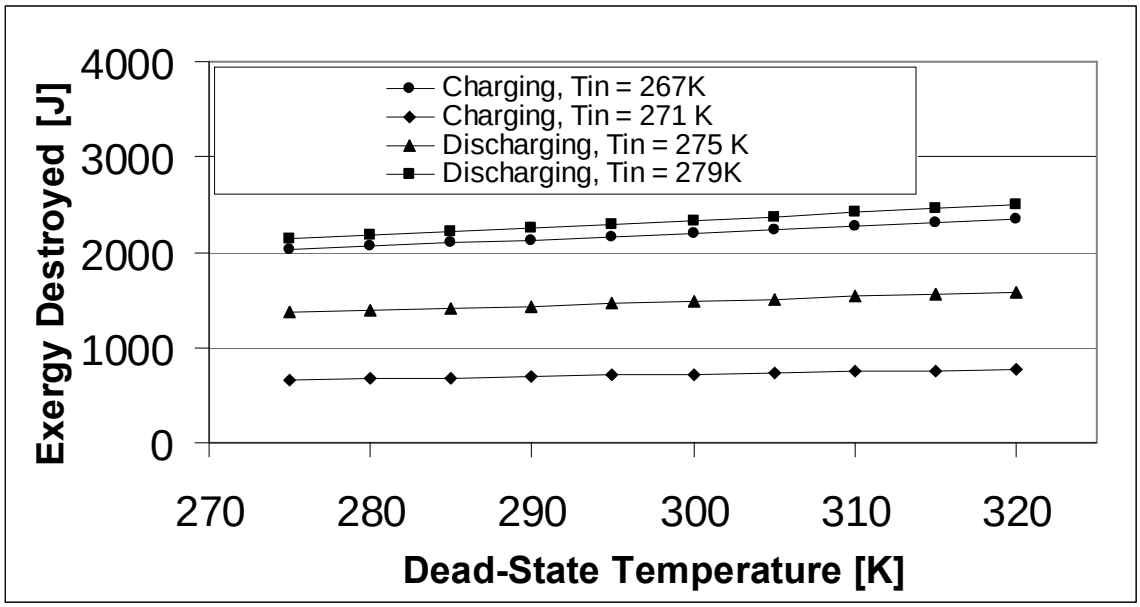


**Figure 5.39: Exergy destruction with respect to dead-state temperature; the spherical geometry with flow rate of $Q_3 = 2.61\times10^{-3}$ m$^3$/s is shown.**

To stay consistent with the above figures, the spherical geometry was chosen again, with a flow rate of $Q_3$, and the same range of ambient temperatures is chosen as in the above

two figures. The trend in the above figure is that the destroyed exergy contents increase with increasing dead-state temperature, as expected since the exergy efficiency is directly proportional to the dead-state temperature, as in equation (4.51). This explains why a linear relationship exists between the destroyed exergy and the dead-state temperature. When the ambient temperature is much warmer, all cold fluids and solids in the system have a much higher quality, and therefore the energy that is lost occurs at a much higher quality level, and subsequently more exergy is destroyed.

These reasons may seem to imply that all cold TES processes are more efficient when the ambient temperature is lower, but this is not the case. Even though the destroyed exergy contents do increase with increased dead-state temperatures, this effect is far outweighed by the change in flow and capsule exergy contents in the charging and discharging modes. In other words, in the charging case, while the increase in dead-state temperature does lower the total exergy destruction, the amount of exergy stored in the PCM after charging increases by a far greater amount, which ultimately lowers the efficiency. Similarly, in the discharging case, though a slight increase in dead-state temperature will actually raise destroyed exergy, it will cause the flow exergy difference realized by the flowing HTF to increase by a greater amount, again raising the efficiency of the process.

Now that ambient temperature conditions have been addressed, a few more comparisons will be conducted before the results and discussion section can be concluded for a more complete assessment of the data obtained in this thesis.

## 5.5 Other Comparisons

When comparing the charging times (Figures 5.4 – 5.6) and discharging times (Figures 5.20 – 5.22), it is apparent that the charging times are greater than the discharging times for similar temperature differences. This is due to the supercooling or superheating phenomena which exist in the solid or liquid states. When the process is initialized prior to transient solutions, it is done so at a temperature of 2 K above or below the freezing point. For instance, for the discharging process, the capsules have an initial temperature of 271K and for the charging process they have a temperature of 275 K. The amount of

sensible heat contained in this superheated or supercooled PCM must first be extracted or released, and it is the differences in the heat capacity of these two phases which the charging time differences can be attributed. Since the specific heat capacity of ice is less than half that of water, it is expected that, in the discharging case, the ice is heated to the melting temperature much faster than the water is cooled in the charging case. There is also an impact of the thermal conductivity of both the ice and water, which would likely cause the opposite effect, but its effect has shown to be miniscule in comparison to the supercooling and superheating effects. The effects of the charging time differences is shown when comparing all of the energy efficiencies, exergy efficiencies and exergy destroyed contents as well.

Another interesting comparison that can be made is the comparison between the energy and exergy efficiencies. As noted earlier, all energy efficiencies, which include only viscous dissipation as losses, had magnitudes which were so close to 100% that the values had to be normalized in order to focus in on the differences in the last percentile. In contrast, the exergy efficiencies were much lower; ranging from around 70% to just above 90% in some cases. Figure 5.40 displays the energy and exergy efficiencies for the cylindrical capsules with an aspect ratio of 8, and flow rate $Q_3$, in the discharging (a) and charging (b) cases.

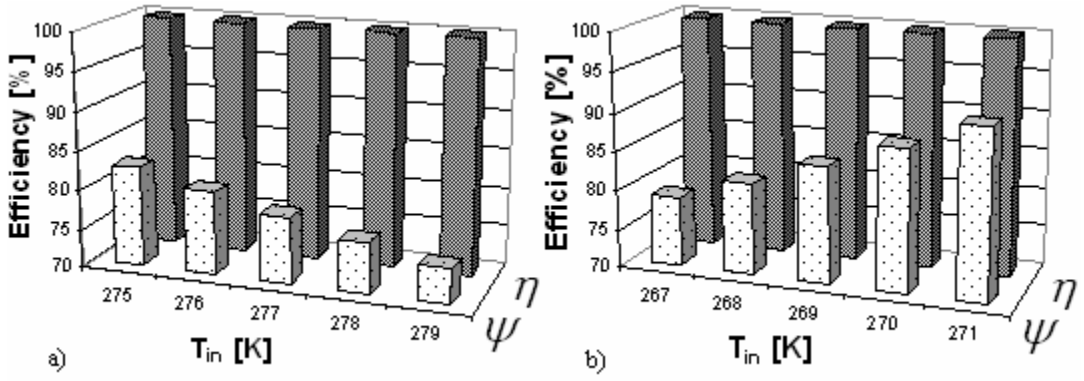


**Figure 5.40: Exergy and energy efficiency comparisons for the discharging (a) and charging (b) cases; the cylindrical capsule with aspect ratio 8 is shown with flow rate $Q_3 = 2.61\times10^{-3}$ m$^3$/s.**

From inspection of Figure 5.40, the energy efficiencies appear to be around 100% for all cases, indicating that the process is nearly ideal. However, in looking at the exergetic efficiencies, the same results cannot be summarized. The exergy efficiencies are much lower, in large part due to the exergy destroyed from heat transfer

accompanying the phase change of the capsules. While energy analyses do provide good insight into system behavior, they are insufficient when analyzing cold TES systems, and only when the exergy analysis is performed is a more complete understanding of system losses understood.

Consider what kinds of losses designers may experience with full storage tanks, since this thesis is concerned only with single capsules in a bed of like capsules. In such a bed, much more energy and exergy will be wasted, and designers will have no choice but to give attention to the factors affecting them. To better illustrate this point, a few more figures have been prepared in Figures 5.41 and 5.42. These convey the amount of exergy destroyed in a full storage tank of either 1,000 or 5,000 capsules during solidification and melting. For brevity, only the flow rate of $Q_3$ is shown with the spherical capsules, and inlet temperatures of 271K for Figure 5.41 and 275K for Figure 5.42.

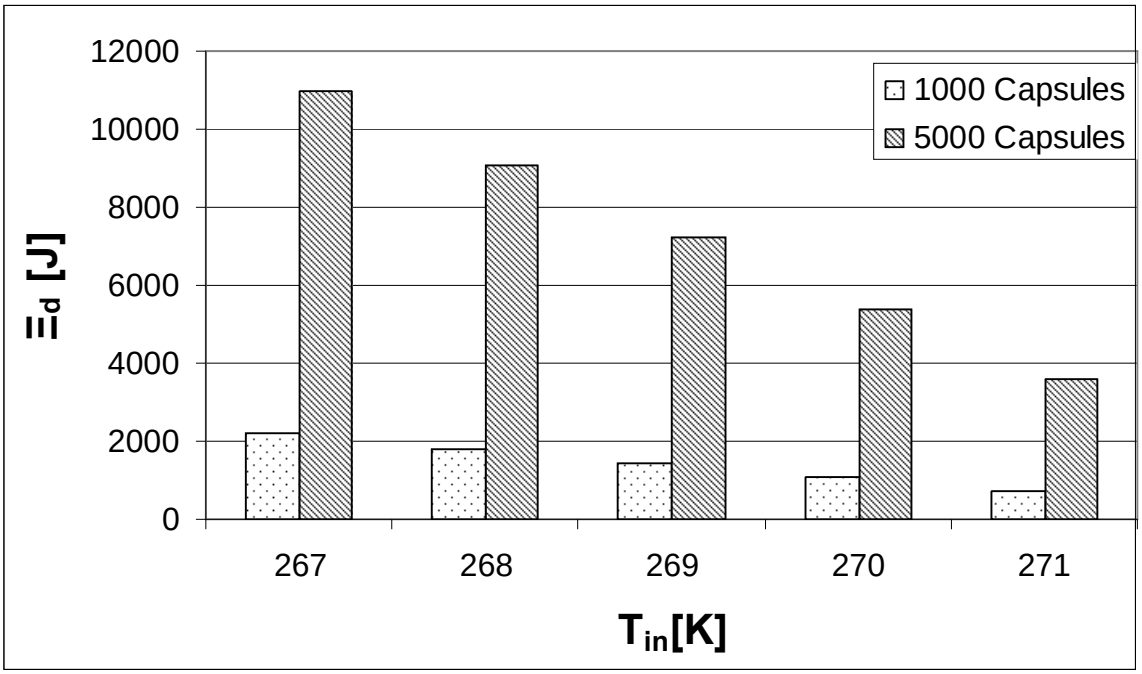


**Figure 5.41: Exergy destroyed contents during charging for the spherical geometry, experiencing a flow rate of $Q_3 = 2.61\times10^{-3}$ m$^3$/s and an inlet temperature of 267K in a bed of 1000 or 5000 capsules.**

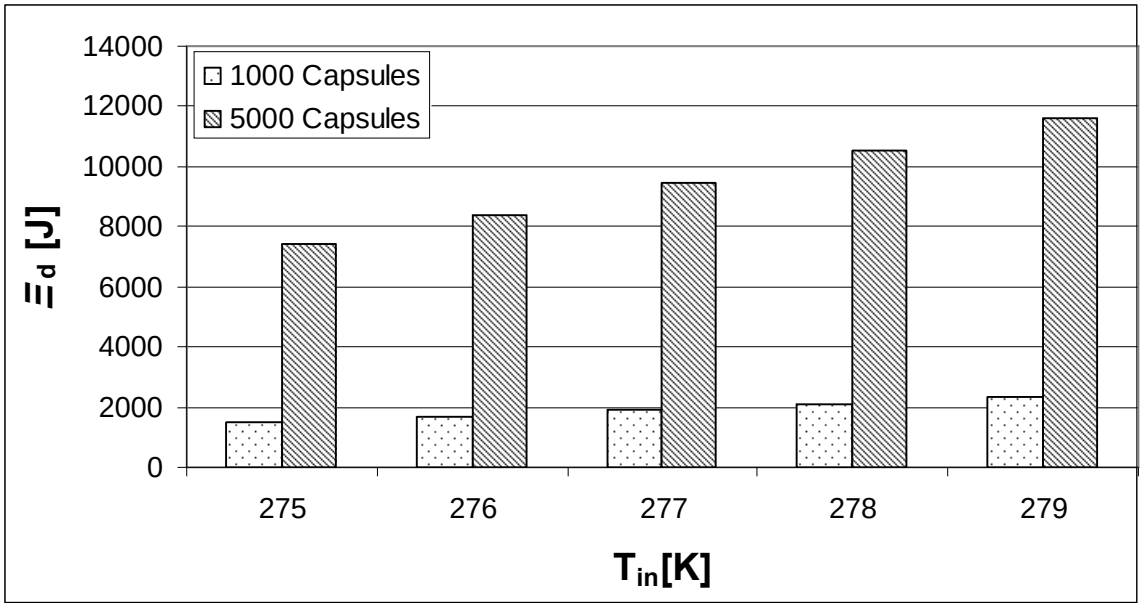


**Figure 5.42: Exergy destroyed contents during discharging for the spherical geometry, experiencing a flow rate of $Q_3 = 2.61\times10^{-3}$ m$^3$/s and an inlet temperature of 279K in a bed of 1000 or 5000 capsules.**

By viewing Figures 5.41 and 5.42, it is more apparent that the amount of exergy loss due to irreversibilities cannot be neglected when a full bed of capsules is considered. The flow phenomena for these cases must be investigated. For every daily charging/discharging process, upwards of 10 kJ of exergy can be lost if no attention is paid to the inner capsule dynamics. It is for this reason why exergy analyses should be implemented during design and before building systems, since large system losses can be avoided by choosing the correct inlet HTF temperatures, flow rates and capsule geometries.

The most important factor regarding exergy efficiency was found to be the inlet HTF temperature. By regulating the temperature – and hence, quality – of the entering HTF fluid, large gains in efficiency can be realized. In addition, it was also found that having a slower HTF flow rate also increased the efficiency in all cases, though the efficiency gains were not as large as when the inlet temperatures were varied. In many cases, the geometries were very similar in efficiency and exergy destroyed. Another final note should be made about the spherical capsules. These geometries have been used in the industry for a number of years, and have many advantages in encapsulated ice TES systems. They can be manufactured to be any size, require no internal structure, and can be packed fairly efficiently at random. For these reasons, if no internal capsule structure

is specified, or it is expensive to implement, the spherical capsules should be the most efficient geometry in most cases.

# 6.0 Conclusions and Recommendations

The process of solidification and melting of some common encapsulated ice TES geometries is simulated here using the commercially available FLUENT 6.0 software for computational fluid mechanics and heat transfer. Various geometries, including spherical, slab (rectangular) and cylindrical capsules with varying aspect ratios are investigated, and modeled to be in a packed bed of like capsules. After extensive grid size, time step, and far-field boundary condition independence tests, the model was validated and found to be in good agreement with experimental results. Following this validation, trials were performed while varying the inlet heat transfer fluid (HTF) temperature, flow rate and reference temperature. The inlet HTF temperature for the charging case ranged from 267K to 271K in increments of 1K, while for the discharging case the inlet HTF temperature varied from 275K to 279K, again in increments of 1K. The initial temperatures of the capsules in the charging and discharging case were set at 275K and 271K, respectively. Three flow rates, chosen to be similar to real-world scenarios, were also investigated, and their effect on the charging and discharging processes were also recorded. In all, 210 simulations were performed on various computers with a range of computing speeds, and the computational time totaled over 1400 hours to carry out all of the trials.

Once these trials were performed, the processes were investigated from thermodynamic principles to give a more realistic view of the performance of each process. Detailed energy and exergy analyses were applied to the processes in full, and gave much meaningful insight into the overall performance. During these analyses, a number of conclusions can be drawn, and relate to the charging and discharging times, energy efficiencies, exergy efficiencies and exergy destruction of the system.

For the case of capsule charging, it was found that lower inlet HTF temperatures achieved solidification faster than higher temperatures. Increasing the flow rate decreased the charging time, but not by the relatively large amounts seen when changing inlet HTF temperatures. However, the solidification times varied significantly when geometry was changed, and the geometries with the best heat transfer characteristics and greater amount of surface area achieved complete solidification faster than others. The

capsules which attained the lowest solidification times were the cylindrical capsules, with highest aspect ratio. As the aspect ratio decreased, the solidification times increased, due to the reduced surface area and inlet flow velocity associated with the domain. The next fastest geometry to solidify was the spherical capsules, followed by the slab capsules, in decreasing order of aspect ratio, for the same reasons.

For the case of capsule discharging, similar results were observed. Higher inlet HTF temperatures melted the PCM faster than lower ones, which is why the higher temperatures attained melting times markedly lower than the inlet temperatures closer to the solidification temperature. The geometries which had desirable heat transfer characteristics in the charging process also produced similar results in the discharging process: the cylinder, followed by the spheres and then the slab capsules, attained the lowest melting times. The aspect ratio, like in the case of capsule charging, tended to increase with decreased melting times.

In studying the energy efficiencies of the system, it was first noticed that the values obtained were quite high; over 99% in all cases. While this is unusual in a broad sense, it is not unexpected, due to the nature of the losses occurring in the system. Due to the assumptions adopted in this thesis, the only energy losses in the system occur as a result of the viscous heating of the fluid. While this value is quite small when compared to the thermal energy transferred, it is certainly not a negligible one, since it amounts to a pressure drop as the heat transfer fluid passes the capsules, which relates directly to the pumping power required for the processes to occur. This is the reason why the normalized energy efficiencies were created, in order to study the energy changes as a result of the boundary conditions and geometry of the system, instead of their overall absolute values.

The conclusions which were drawn in the energy analysis are closely related to the charging and discharging times, due to the nature of the efficiency equation. Since the energy efficiency depends directly on the viscous dissipation within the fluid, the geometries with the fastest moving fluid and the greatest amount of surface area produced the highest velocity gradients in the heat transfer fluid. While this amounts to a higher convective heat transfer rate, and lowers the charging time, the amount of viscous heating is greatly increased, which ultimately lowers the energy efficiency. As a result,

for both the cases of charging and discharging, the cylindrical capsules were of the lowest energy efficiency, followed by the spherical capsules, with the slab capsules seeing the highest efficiencies. In terms of aspect ratio, it was found, unsurprisingly, that the energy efficiency decreased with increased aspect ratio, once again the effect of the heat transfer fluid velocity and geometry surface area on the overall viscous dissipation.

It was also surprising to note that the spherical geometry had unusually high energy efficiencies in both the charging and the discharging cases. Due to the inconsistent geometry of the system, coupled with a relatively high inlet heat transfer velocity, it was expected that this geometry have the lowest energy efficiency. However, this was not the case, and in investigation of the flow fields, it was deemed due to the reduced skin friction or drag in the capsule geometry from swirl effects. In the deep pockets of the heat transfer fluid zone, where velocities are expected to be quite erratic and viscous effects visible, a circular swirling motion was developed, which allowed the flowing heat transfer fluid to pass through the control volume with much more ease. The swirling motion of these recesses acted as a sort of "slip wall" where viscous effects are quite negligible, and served to reduce the amount of overall viscous dissipation, while still retaining a relatively high heat transfer rate to the capsules.

The inlet flow rate was found to have a large effect on the energy efficiency, due to the amount viscous heating it incurs. For the larger flow rates, the velocity gradients become much higher and as a result, the viscous dissipation increases. This lowers the energy efficiency so that for the higher the flow rate was set, the lower the efficiency recorded. In the same facet, the inlet heat transfer fluid temperature had a large effect on efficiency. Once again, the viscous dissipation is the only factor to consider, and for the inlet temperatures which strayed farther away from the solidification temperature – namely the lowest temperatures for the charging case and the highest temperatures for the discharging case – the charging time was reduced. This lowered the amount of overall viscous dissipation in the fluid, since the dissipation term relies on the total volume of heat transfer fluid used in the process. Therefore, it can be summarized that the lowest inlet heat transfer fluid temperatures in the charging case, as well as the highest inlet heat transfer fluid temperatures in the discharging case, incur the highest energy efficiencies.

While assessing the exergy efficiencies of the system, it was found that the results drastically differed from its energy counterpart. Firstly, it was noticed that the efficiency values ranged from 79% to 92% in the charging case, and 72% to 84% in the case of discharging. This is much lower than the energy case, and it is due in large part to the inclusion of the destroyed exergy due to heat transfer accompanying phase change. Since the system undergoes a change from one state to another, exergy is destroyed in the process. It is this destroyed exergy which must be minimized in order to optimize system design.

Another difference between energy and exergy analyses is the dependence on geometry. In the energy analysis, the only losses in the system result from viscous dissipation. The highest efficiencies resulted from scenarios which incurred the least amount of viscous heating. These situations corresponded to the lowest inlet HTF velocities coupled with the inlet HTF temperatures, which maximized heat transfer rates. However, in the exergy analysis, a different trend was noticed. For both the charging and discharging cases, it was found that the inlet HTF temperatures that significantly raised charging times were the best temperatures to use exergetically. In the case of charging, this meant that using a higher temperature fluid to freeze the capsules resulted in higher efficiencies. In the case of discharging, a lower inlet temperature was more efficient. This is a result of using the least amount of a quality, cold fluid in the charging case, and producing a colder, quality fluid in the discharging case. However, for the discharging case, the exact opposite effects were realized by the energy analysis. As a result, the energy analysis should be deemed inexact for producing such unrealistically high efficiency values, and optimum conditions which disagree with the exergy analysis (and for the most part, common sense).

However, one similarity exists between the two analyses; the effect of HTF flow rate on both the energy and exergy efficiencies. For all cases, it was observed that lowering the flow rate had a positive effect on system performance. This is once again largely due to the optimization of quality energy in the system. For the charging case, the quality fluid in question is the cold inlet HTF, which must receive heat from the charging capsules. For smaller flow rates, a lesser mass of HTF must be used to complete the process, resulting in less quality fluid being used. For the larger flow rates, more quality

fluid must be used, which results in both a greater amount of viscous dissipation and a greater amount of exergy input due to the usage of this quality fluid.

In terms of geometry, there were very small differences in exergy efficiency, but these differences were noted nonetheless. For both the charging and discharging cases, the most efficient geometry varied according to inlet HTF temperature and flow rate. However, the most efficient scenarios are of utmost importance, so for the charging case, the cylindrical capsule with an aspect ratio of 8 was most efficient, but only with an inlet HTF temperature of 271K and flow rate $Q_1$. This is due to the increased heat transfer characteristics of the system, which minimized the amount of destroyed exergy due to wasted quality fluid used. In the discharging case, however, the spherical capsules were the most efficient, with an inlet HTF temperature of 275K and flow rate $Q_1$. It is interesting to note that a different capsule geometry resulted in a more efficient scenario in the discharging case. After close examination, the cause of this was determined to be surface area resistance and increased volume in the PVC region. Since the cylindrical capsules have much greater surface area with higher aspect ratios, more of the PVC must be heated first in order to extract the latent heat from the capsules. This phenomenon creates more destroyed exergy and raises the total amount of required exergy to complete the process, ultimately resulting in a lower efficiency.

The exergy destroyed was found to perhaps be the greatest indicator of system performance, because it illustrates the quantity and locations of irreversibilities within the system. The exergy destroyed is a result of quality energy being forever lost in a process, and is a clear indicator of thermodynamic performance because it is intimately related to the exergy efficiency. The destroyed exergy in this case is the result of two phenomena; destroyed exergy due to viscous heating and destroyed exergy, due to entropy generation accompanying heat transfer and phase change. In all cases, a greater amount of destroyed exergy resulted in a lower exergy efficiency.

Two main notes should be summarized about the two modes of exergy destruction; the comparisons in overall magnitude, and the fact that in the discharging case, the two modes of destroyed exergy experienced different dependencies on inlet HTF temperature. In comparing the magnitude of exergy destroyed, it was found that destroyed exergy due to viscous dissipation was minor in comparison to the exergy

destroyed accompanying heat transfer and phase change. This is due to the extremely small amount of actual energy which is lost in pressure drop and friction when compared to the overall amount of thermal energy or exergy present in the system. In all cases, the contribution to exergy destroyed resulting from viscous dissipation was less than 1%, and plays no significant role when determining losses. However, since destroyed exergy values are very similar across geometries, it should not be ignored, since its inclusion could lead to more efficient geometric design of the interior flow fields of encapsulated TES storage tanks. The other note which must be addressed is the fact that for the case of discharging, the lowest amount of destroyed exergy was found when the inlet HTF temperature was set to 275K – closest to the solidification temperature. While this makes sense in terms of extracting the most quality flow from the discharging capsules, the opposite effect was noticed when viewing the destroyed exergy from viscous dissipation. Since the viscous dissipation relies on the bulk fluid temperature (which is more or less equal to the inlet HTF temperature), a higher inlet temperature results in less exergy is destroyed; since the frictional heating occurs at a less quality state. When the inlet HTF temperature is lowered, this frictional heating will occur at a more quality temperature, resulting in more destroyed exergy. However, since the contribution to overall destroyed exergy from this mode is quite small, no noticeable effect was observed due to this trend.

In summary, for a more straightforward view of the many results viewed in this thesis, they are listed below in point form.

In the case of capsule charging (solidification), the following observations were made.

- Charging times tended to decrease along with decreased inlet heat transfer fluid temperatures.
- The cylindrical capsules, followed by the spherical and the slab capsules, experienced the lowest charging times.
- Charging times decreased with increased capsule aspect ratio.
- Flow rate has little effect on charging times when compared to varying the inlet HTF temperature, though higher flow rates did produce lower charging times.
- Increased heat transfer fluid temperatures corresponded to decreased energy efficiencies.

- Increased heat transfer fluid temperatures resulted in increased exergy efficiencies.
- Increased flow rates correspond to decreased energy and exergy efficiencies.
- The slab capsules were the most efficient energetically, followed closely by the spherical capsules and lastly the cylindrical capsules.
- The most efficient energy scenario was realized by the slab capsule with aspect ratio of 2, flow rate $Q_1$ and inlet HTF temperature of 267K, which attained an efficiency of 99.99995%.
- Exergetically, the best scenario was realized with the cylindrical capsule with aspect ratio of 8, flow rate $Q_1$ and inlet HTF temperature of 271K, resulting in an exergy efficiency of 92.15%.
- Increased aspect ratios led to decreased energetic efficiencies for all shapes.
- There was no clear connection between aspect ratio and exergy efficiency for all shapes; some increased, decreased, or attained maxima or minima when aspect ratio increased.
- Destroyed exergy due to viscous dissipation was far less than exergy destroyed due to entropy generation resulting from heat transfer accompanying phase change.

In the case of capsule discharging (melting), the following observations were made.

- Discharging times tended to decrease along with increased inlet heat transfer fluid temperatures.
- The cylindrical capsules, followed by the spherical and the slab capsules, experienced the lowest discharging times.
- Discharging times decreased with increased capsule aspect ratio.
- Flow rate has little effect on charging times when compared to the effects seen by changing inlet HTF temperature, but higher flow rates produced lower charging times.
- Increased heat transfer fluid temperatures corresponded to decreased energy efficiencies.

- Increased heat transfer fluid temperatures resulted in increased exergy efficiencies.
- Increased flow rates correspond to decreased energy and exergy efficiencies.
- The slab capsules were the most efficient energetically, followed closely by the spherical capsules and lastly the cylindrical capsules.
- The most efficient energy scenario was realized by the slab capsule with aspect ratio of 2, flow rate $Q_1$ and inlet HTF temperature of 279K, which attained an efficiency of 99.99996%.
- Exergetically, the best scenario was realized with the spherical capsule, flow rate $Q_1$ and inlet HTF temperature of 275K, resulting in an exergy efficiency of 84.45%.
- Increased aspect ratios led to decreased energetic efficiencies for all shapes.
- There was no clear connection between aspect ratio and exergy efficiency for all shapes; some increased, decreased, or attained maxima or minima when aspect ratio increased.
- Once again, the destroyed exergy due to viscous dissipation was far less than exergy destroyed due to entropy generation resulting from heat transfer accompanying phase change.

Lastly, the effect of the dead-state (or reference) temperature is very interesting to note. It was noticed that while the reference temperature had absolutely no effect on the energy efficiency, the exergy efficiency was drastically improved by increasing the dead state temperature. The opposite effect was also true; a lowering of the reference temperature produced much lower exergy efficiencies. This is due to the quality of the latent storage. For higher reference temperatures, the latent heat storage is much higher, which produces much higher efficiencies since the exergy destroyed term is largely unaffected by reference temperature in comparison.

When comparing the overall effect of geometry on the performance of the processes, one final note should be made. Although many different optimal conditions can be realized by varying the flow rate and aspect ratios of the capsule geometries, on a broader scale, the effect of inlet HTF temperature is much more dominant when viewing

both the energy and exergy efficiencies. For this reason, the spherical capsules, which do attain very high energy and exergy efficiency values, should be used with negligible drawbacks on efficiency values. These spherical capsules, as noted earlier, are very cost effective, since they can be simply dumped into any storage tank and tend to pack quite efficiently at random.

Before concluding, a few recommendations for anyone interested in conducting a similar study should be outlined. These include improvising the current model and conducting other similar studies which could be used in conjunction with the study in question here.

Since FLUENT 6.0 software is a very powerful tool in computational fluid mechanics and heat transfer, it could be used to investigate the impact of turbulence on the aforementioned study. Since turbulence is left relatively untouched in the discussion of the results, it is nonetheless important. For example, the spherical pathlines realized in Figure 5.10 indicate a turbulent flow regime, but it is unclear to what extent turbulence plays in the viscous heating of the other geometries, which experienced purely laminar flow fields. If more capsule rows were considered, possibly with gaps to more correctly simulate real flow conditions, the effect of this turbulence on the skin friction in the HTF flow field could be of interesting debate. In addition to this, using turbulent analysis, the number of capsule rows could be optimized in order to obtain the least amount of viscous heating, entropy generation and destroyed exergy in the storage tank.

Other future works which would enhance the usefulness of this thesis could inspect an entire storage system, subject to heat leakage, to determine the effects of storage tank insulation on overall efficiency. It is expected that the addition of this phenomena to the problem would increase the accuracy of the results in relation to real-world scenarios. However, the computational requirements for such a task would be immense, so until more computing power is available, these results should be taken as sufficient. Other works could also focus on aspect ratio optimization, since it is clear that maxima and/or minima do exist in exergy efficiency analysis. Entropy generation minimization could be an excellent future task as well. In addition to this, another interesting future work could be an exergoeconomic analysis, which broadly stated, combines exergy analysis with economics to help builders see more cost-friendly designs

which also reduce environmental impact. These future studies could also be used to determine the best operating strategies by region, and should provide a more complete insight into the design and implementation of the charging and discharging modes of various encapsulated ice TES systems.

# 7.0 References


Adref, K. T. and Eames, I. W., 2002, "Experiments on Charging and Discharging of Spherical Thermal (Ice) Storage Elements," *International Journal of Energy Research* **26**, pp. 949 – 964.

Aseev, D. L. and Alexandrov, D. V., 2006, "Unidirectional Solidification with a Weak Mushy Layer. The Influence of Weak Convection," *Acta Materialia* **54**, pp. 2401 – 2406.

ASHRAE, 1997, ASHRAE Fundamentals Handbook (SI). Chapter 20: Physical Properties of Secondary Coolants (Brines), pp. 20.6 – 20.7.

Assis, E., Katsman, L, Ziskind, G. and Letan, R., 2007, "Numerical and Experimental Study of Melting in a Spherical Shell," *International Journal of Heat and Mass Transfer* **50**, pp. 1790 – 1804.

Barba, A. and Spiga, M., 2003, "Discharge Mode for Encapsulated PCMs in Storage Tanks," *Solar Energy* **74**, pp. 141 – 148.

Bedecarrats, J. P., Strub, F., Falcon, B. and Dumas, J. P., 1996, "Phase Change Thermal Energy Storage using Spherical Capsules: Performance of a Test Plant," *International Journal of Refrigeration* **19**, pp. 187 – 196.

Benmansour, A., Hamdan, M. A. and Bengeuddach, A., 2006 "Experimental and Numerical Investigation of Solid Particles Thermal Energy Storage Unit," *Applied Thermal Engineering* **26**, pp. 513 – 518.

Bilir, L. and Ilken, Z., 2005, "Total Solidification Time of a Liquid Phase Change Material Enclosed in Cylindrical/Spherical Containers," *Applied Thermal Engineering* **25**, pp. 1488 – 1502.

Cabeza, L. F., Castellon, C., Nogues, M., Medrano, M., Leppers, R. and Zubillaga, O., 2007, "Use of Microencapsulated PCM in Concrete Walls for Energy Savings," *Energy and Buildings* **39**, pp. 113 – 119.

Casano, G. and Piva, S., 2002, "Experimental and Numerical Investigation of the Steady Periodic Solid-Liquid Phase-Change Heat Transfer," *International Journal of Heat and Mass Transfer* **45**, pp. 4181 – 4190.

Chan, C. W. and Tan, F. L., 2006, "Solidification Inside a Sphere – An Experimental Study," *International Communications in Heat and Mass Transfer* **33**, pp. 335 – 341.

Chang, W. S. and Nixon, J. L., 2001, "Long-Term Experience with External-Melt Ice-On-Coil Storage Cooling System," *ASHRAE Transactions* **107**, pp. 532 – 537.

Chen, S. L., Chen, C. L., Tin, C. C., Lee, T. S. and Ke, M.C., 2000, "An Experimental Investigation of Cold Storage in and Encapsulated Thermal Storage Tank," *Experimental Thermal and Fluid Science* **23**, pp. 133 – 144.

Chen, Y. H. and Lin, H. T., 1997, "Natural Convection in an Inclined Enclosure with a Fluid Layer and a Heat-Generating Porous Bed," *Heat and Mass Transfer* **33**, pp. 247 – 255.

Cheralathan, M., Velraj, R. and Renganarayanan, S., 2007, "Performance Analysis on Industrial Refrigeration System Integrated with Encapsulated PCM-Based Cool Thermal Energy Storage System," *International Journal of Energy Research* **31**, pp. 1398 – 1413.

Cho, K. and Choi, S. H., 2000, "Thermal Characteristics of Paraffin in a Spherical Shell Capsule During Freezing and Melting Processes," *International Journal of Heat and Mass Transfer* **43**, pp. 3183 – 3196.

Chorin, A. J., 1968, "Numerical Solution of Navier-Stokes Equations," *Mathematics of Computation* **22**, pp. 745 – 762.

Choudhury, C., Chauhan, P. M. and Garg, H. P., 1995, "Economic Design of a Rock Bed Storage Device for Storing Solar Thermal Energy" *Solar Energy* **55**, pp. 29 – 37.

Churchill, S. W., 1983, "Comprehensive Theoretically Based, Correlating Equations for Free Convection from Isothermal Spheres," *Chemical Engineering Communications* **24**, pp. 339 – 352.

Cristopia, 2003, *Sub-Zero Thermal Energy Storage for Process Cooling*, Kansas City, USA.

De Souza, S. I. S., and Vielmo, H. A., 2005, "Numerical Analysis of Water Melting and Solidification in the Interior of Tubes," *Journal of the Brazilian Society of Mechanical Sciences and Engineering* **27**, pp. 119 – 131.

Dekhtyar, R. A., Sikovsky, D. P., Gorine, A. V. and Mukhin, M., 2002, "Heat Transfer in a Packed Bed at Moderate Values of the Reynolds Number," *High Temperature* **40**, pp. 693 – 700.

Delgado, J. M. P. Q., 2006, "A Critical Review of Dispersion in Packed Beds," *Heat Mass Transfer* **42**, pp. 279 – 310.

Dincer, I. and Rosen, M., 2002, *Thermal Energy Storage: Systems and Applications*, John Wiley & Sons Ltd., Chichester, England.

Eames, I. W. and Adref, K. T., 2002, "Freezing and Melting of Water in Spherical Enclosures of the Type Used in Thermal (Ice) Storage Systems," *Applied Thermal Engineering* **22**, pp. 733 – 745.

El-Kotb, M., El-Sharkawy, A., El Chazly, N. M., Khattab, N. M. and El-Deeb, S., 2006, "Thermal Characteristics of Paraffin Wax for Solar Energy Storage," *Energy Sources, Part A* **28**, pp. 1113 – 1126.

Erek, A. and Ezan, M. A., 2007, "Experimental and Numerical Study on Charging Processes of an Ice-On-Coil Thermal Energy Storage System," *International Journal of Energy Research* **31**, pp. 158 – 176.

Ettouney, H., El-Dessouky, H. and Al-Ali, A., 2005, "Heat Transfer during Phase Change of Paraffin Wax Stored in Spherical Shells," *Journal of Solar Energy Engineering* **127**, pp. 357 – 365.

Hasnain, S. M., 1998, "Review on Sustainable Thermal Energy Storage Techniques, Part 1: Heat Storage Materials and Techniques," *Energy Conversion and Management* **30**, pp. 1127 – 1138.

Hawlader, M. N. A., Uddin, M. S. and Zhu, H. J., 2002, "Encapsulated Phase Change Materials for Thermal Energy Storage: Experiments and Simulation," *International Journal of Energy Research* **26**, pp. 159 – 171.

Hawlader, M., Uddin, M. S. and Khin, M. M., 2003, "Microencapsulated PCM Thermal-Energy Storage System," *Applied Energy* **74**, pp. 195 – 202.

Hawlader, M., Uddin, M. S. and Zhu, H. J., 2000, "Preparation and Evaluation of a Novel Solar Storage Material: Microencapsulated Paraffin," *International Journal of Sustainable Energy* **20**, pp. 227 – 238.

Henze, Gregory P., 2003, "An Overview of Optimal Control for Central Cooling Plants with Ice Thermal Energy Storage," *Journal of Solar Energy Engineering* **125**, pp. 302 – 309.

Henze, Gregory P., 2005, "Energy and Cost Minimal Control of Active and Passive Thermal Storage Inventory," *Journal of Solar Energy Engineering* **127**, pp. 343 – 351.

Ihm, P., Krarti, M. and Henze, G. P., 2004, "Development of a Thermal Energy Storage Model for EnergyPlus," *Energy and Buildings* **36**, pp. 807 – 814.

Inalli, M., Unsal, M. and Tanyildiza, V., 1996, "A Computational Model of a Domestic Solar Heating System with Underground Spherical Thermal Storage," *Energy* **22**, pp. 1163 – 1172.

Ismail, K. A. R., Henriquez, J. R. and Da Silva, T. M., 2003, "A Parametric Study on Ice Formation Inside a Spherical Capsule," *International Journal of Thermal Sciences* **42**, pp. 881 – 887.

Karakilcik, M., Dincer, I. and Rosen, M., 2006, "Performance Investigation of a Solar Pond," *Applied Thermal Engineering* **26**, pp. 727 – 735.

Kasza, K. E. and Hayashi, K., 1999, "Ice Slurry Cooling Research: Storage Tank Ice Agglomeration and Extraction," *ASHRAE Transactions* **105**, pp. 260 – 266.

Kayansayan, N. and Acar, M. A., 2006, "Ice Formation around a Finned-Tube Heat Exchanger for Cold Thermal Energy Storage," *International Journal of Thermal Sciences* **45**, pp. 405 – 418.

Kerslake, T. W. and Ibrahim, M. B., 1990, "Two-Dimensional Model of a Space Station Freedom Thermal Energy Storage Canister," *Energy Conversion Engineering* **2**, pp. 151 – 159.

Khudhair, A. M. and Farid, M. M., 2004, "A Review on Energy Conservation in Building Applications with Thermal Energy Storage by Latent Heat Using Phase Change Materials," *Energy Conversion and Management* **45**, pp. 263 – 275.

Kiatreungwattana, K. and Krarti, M., 2002, "Evaluation of an Internal Melt Ice-On-Coil Storage Tank during Partial Charging and Discharging Cycles," *ASHRAE Transactions* **108**, pp. 1061 – 1071.

Koszawa, Y., Aizawa, N. and Tanino, M., 2005, "Study on Ice Storage Characteristics in Dynamic-Type Ice Storage System by Using Super-cooled Water. Effects of the Supplying Conditions of Ice-Slurry at Deployment to District Heating and Cooling System," *International Journal of Refrigeration* **28**, pp. 73 – 82.

Kousksou, T., Bedecarrats, J. P., Dumas, J. P. and Mimet, A., 2005, "Dynamic Modeling of the Storage of an Encapsulated Ice Tank," Applied Thermal Engineering **25**, pp. 1534 – 1548.

Kuznetsov, A. V., 1995, "An Analytical Solution for Heating in a Two-Dimensional Porous Packed Bed by a Non-Thermal Equilibrium Fluid Flow," *Applied Scientific Research* **55**, pp. 83 – 93.

Laguerre, O., Amara, S. B., Alvarez, G. and Flick, D., 2008, "Transient Heat Transfer by Free Convection in a Packed Bed of Spheres: Comparison between Two Modeling Approaches and Experimental Results," *Applied Thermal Engineering* **28**, pp. 14 – 24.

Lamberg, P. and Siren, K., 2003, "Approximate Analytical Model for Solidification in a Finite PCM Storage with Internal Fins," *Applied Mathematical Modeling* **27**, pp. 491 – 513.

Lee, A. H. W. and Jones, J. W., 1996, "Laboratory Performance of an Ice-On-Coil, Thermal Energy Storage System for Residential and Light Commercial Applications," *Energy* **21**, pp. 115 – 130.

Lee, A. H. W. and Jones, J., 1996, "Modeling of an Ice-On-Coil Thermal Energy Storage System," *Energy Conversion and Management* **37**, pp. 1493 – 1507.

Lin, H. J. and Horvath, S., 1981, "Viscous Dissipation in Packed Beds," *Chemical Engineering Science* **36**, pp. 47 – 55.

MacPhee, D. and Dincer, I., 2008, "Thermal Modeling of a Packed Bed Thermal Energy Storage System during Charging," *Applied Thermal Engineering*, doi:10.1016/j.applthermaleng.2008.03.041

MacPhee, D. and Dincer, I., 2008, "Thermal Performance Analysis of the Solidification and Melting Processes in Various Encapsulated Ice Geometries," *Numerical Heat Transfer*, In Progress.

Matsumoto, K., Namiki, Y., Odaka, M., Kawagoe, T., Nakagawa, S. and Kang, C., 2004, "Continuous Ice Slurry Formation Using a Functional Fluid for Ice Storage," *International Journal of Refrigeration* **27**, pp. 73 – 81.

Mousavi, S. M., Jafari, A., Yaghmaei, S., Vossoughi, M. and Sarkomaa, P., 2006, "Computer Simulation of Fluid Motion in a Porous Bed Using a Volume of Fluid Method: Application in Heap Leaching," *Minerals Engineering* **19**, pp. 1077 – 1083.

Nakayama, A., Kuwahara, F. and Kodama, Y., "An Equation for Thermal Dispersion Flux Transport and its Mathematical Modeling for Heat and Fluid Flow in a Porous Medium," *Journal of Fluid Mechanics* **563**, pp. 81 – 96.

Nakayama, A., Kuwahara, F., Sugiyama, M. and Xu, G., 2001, "A Two-Energy Equation Model for Conduction and Convection in Porous Media," *International Journal of Heat and Mass Transfer* **44**, pp. 4375 – 4379.

Nallusamy, N., Sampath, S. and Velraj, R., 2007, "Experimental Investigation on a Combined Sensible and Latent Heat Storage System Integrated with Constant/Varying (Solar) Heat Sources," *Renewable Energy* **32**, pp. 1206 – 1227.

Nallusamy, N., Sampath, S., and Velrag, R., 2006, "Study on Performance of a Packed Bed Latent Heat Thermal Energy Storage Unit with Solar Water Heating System," *Journal of Zhejiang University SCIENCE A* **7**, pp. 1422 – 1430.

Nsofor, E. C., 2005, "Investigations on the Packed Bed for High-Temperature Thermal Energy Storage," *International Journal of Green Energy* **2**, pp. 337 – 351.

Ozonur, Y., Mazman, M., Paksoy, H. O. and Evliya, H., 2005, "Microencapsulation of Coco Fatty Acid Mixture for Thermal Energy Storage with Phase Change Material," *International Journal of Energy Research* **30**, pp. 741 – 749.

Paksoy, H. O., 2003, "Cooling in All Climates with Thermal Energy Storage" Annex 14, General State-of-the-Art Report: Subtask 1.

Pinelli, M. and Piva, S., 2003, "Solid/Liquid Phase Change in Presence of Natural Convection: A Thermal Energy Storage Case Study," *Journal of Energy Resources Technology* **125**, pp. 190 – 198.

Regin, A. F., Solanki, S. C. and Saini, J. S., 2006, "Latent Heat Thermal Energy Storage Using Cylindrical Capsule: Numerical and Experimental Investigations," *Renewable Energy* **31**, pp. 2025 – 2041.

Rosen, M. A. and Dincer, I., 2003, "Exergy Methods for Assessing and Comparing Thermal Storage Systems," *International Journal of Energy Research* **27**, pp. 415 – 430.

Rosen, M. A., Dincer, I. and Pedinelli, N., 2000, "Thermodynamic Performance of Ice Thermal Energy Storage Systems," *Journal of Energy Resources Technology* **122**, pp. 205 – 211.

Rosen, M. A., Pedinelli, N. and Dincer, I., 1999, "Energy and Exergy Analyses of Cold Thermal Storage Systems," *International Journal of Energy Research* **23**, pp. 1029 – 1038.

Sahin, A. Z., 1999, "The Effect of Variable Viscosity on the Entropy Generation and Pumping Power in a Laminar Fluid Flow Through a Duct Subjected to Constant Heat Flux," *Heat and Mass Transfer* **35**, pp. 499 – 506.

Saito, A., 2002, "Recent Advances in Research on Cold Thermal Energy Storage," *International Journal of Refrigeration* **25**, pp. 177 – 189.

Sari, A. and Kaygusuz, K., 2002, "Thermal and Heat Transfer Characteristics in a Latent Heat Storage System Using Lauric Acid," *Energy Conversion and Management* **43**, pp. 2493 – 2507.

Sari, A. and Kaygusuz, K., 2002, "Thermal Performance of a Eutectic Mixture of Lauric and Stearic Acids as PCM Encapsulated in the Annulus of Two Concentric Pipes," *Solar Energy* **72**, pp. 493 – 504.

Sari, A. and Kaygusuz, K., 2005, "Thermal Energy Storage System Using a Technical Grade Paraffin Wax as Latent Heat Energy Storage Material," *Energy Sources* **27**, pp. 1535 – 1546.

Sari, A. and Kaygusuz, K., 2006, "Thermal Energy Storage Performance of Fatty Acids as a Phase Change Material," *Energy Sources, Part A* **28**, pp. 105 – 116.

Sassmore, 2008, "Evapco® Ice coils - Featuring the Extra-Pak™ Technology. http://www.evapco.com/media/pdf/ice_coils_catalog.pdf

Sharma, S. D. and Sagara, K., 2007, "Latent Heat Storage Materials and Systems: A Review," *International Journal of Green Energy* **2**, pp. 1 – 56.

Singh, C., Tathgir, R. G. and Muralidhar, K., 2006, "Experimental Validation of Heat Transfer Models for Flow Through a Porous Medium," *Heat Mass Transfer* **43**, pp. 55 – 72.

Voller, V. R. and Prakash, C., 1987c, "A Fixed-Grid Numerical Modeling Methodology for Convection-Diffusion Mushy Region Phase-Change Problems," *Int. J. Heat Mass Transfer* **30**, pp. 1709 – 1720.

Voller, V. R., 1987a, "Modeling Solidification Processes," Technical report, *Mathematical Modeling of Metals Processing Operations Conference, American Metallurgical Society*.

Voller, V. R., Brent, A. D. and Reid, K. J., 1987b, "A Computational Modeling Framework for the Analysis of Metallurgical Solidification Process and Phenomena," Technical report, *Conference for Solidification Processing*.

Wang, M. J. and Kusumoto, N., 2001, "Ice Slurry Based Thermal Storage in Multifunctional Buildings," *Heat and Mass Transfer* **37**, pp. 597 – 604.

Wei, J., Kawaguchi, Y., Hirano, S. and Takeuchi, H., 2005, "Study on a PCM Heat Storage System For Rapid Heat Supply," *Applied Thermal Engineering* **25**, pp. 2903 – 2920.

Wen, D. and Ding, Y., 2006, "Heat Transfer of Gas Flow Through a Packed Bed," *Chemical Engineering Science* **61**, pp. 3532 – 3542.

Xing, L., Hongyan, L., Shujun, W., Lu, Z. and Hua, C., 2006, "Preparation and Thermal Properties of Form Stable Paraffin Phase Change Material Encapsulation," *Energy Conversion and Management* **47**, pp. 2515 – 2522.

Yamada, M., Fukusako, S. and Kawabe, H., 2002, "A Quantitative Evaluation of the Production Performance of Ice Slurry by the Oscillatory Moving Cooled Wall Method," *International Journal of Refrigeration* **25**, pp. 199 – 207.

Yamagishi, Y., Sugeno, T., Ishige, T., Takuchi, H. and Pyatenko, A. T., 1996, "An Evaluation of Microencapsulated PCM for Use in Cold Energy Transportation Medium," *Energy Conversion Engineering Conference* **3**, pp. 2077 – 2083.

Yamagishi, Y., Takeuchi, H., Pyatenko, A. T. and Kayukawa, N., 1999, "Characteristics of a Microencapsulated PCM Slurry as a Heat Transfer Fluid," *AIChE Journal* **45**, pp. 696 – 707.

Yee, S. S. and Kamiuto, K., 2002, "Effect of Viscous Dissipation on Forced-Convection Heat Transfer in Cylindrical Packed-Beds," *International Journal of Heat and Mass Transfer* **45**, pp. 461 – 464.

Yuksel, N., Avci, A. and Kilic, M., 2006, "A Model for Latent Heat Storage Systems," *International Journal of Energy Research* **30**, pp. 1146 – 1157.

Zhang, Y., Su, Y., Zhu, Y. and Hu, X., 2001, "A General Model for Analyzing the Thermal Performance of the Heat Charging and Discharging Processes of Latent Heat Thermal Energy Storage Systems," *Journal of Solar Energy Engineering*, **123**, pp. 232 – 236.

Zhu, Y. and Zhang, Y., 2001, "Modeling of Thermal Processes for Internal Melt Ice-On-Coil Tank Including Ice-Water Density Difference," *Energy and Buildings* **33**, pp. 363 – 370.

Zukowski, M., 2007, "Mathematical Modeling and Numerical Simulation of a Short Term Thermal Energy Storage System using Phase Change Material for Heating Applications," *Energy Conversion and Management* **48**, pp. 155 – 165.

# 8.0 Biographical Sketch

David MacPhee was born in Pembroke, Ontario. The third of four children, he excelled at a young age in mathematics which compelled him to study in the field of engineering. He obtained his Bachelor of Science in Mathematics and Engineering at Queen's University in Kingston, Ontario, in 2006. After taking the next few months to decide his future, he ultimately chose to continue his schooling career as a graduate student at the University Of Ontario Institute Of Technology in Oshawa, Ontario, studying in the field of thermal energy storage systems. Over the next year and a half, he studied the heat transfer, fluid mechanics and thermodynamics of such systems, and learned much about the many relevant computer aided design and simulation software used in analysis. His research works, coupled with his excellent graduate course work, earned him the Jeffrey Boyce Engineering Award in energy related research in 2008; an award given to students who excel in energy related engineering fields.

In addition to his research work, David also enjoys teaching in the fields of fluid mechanics, heat transfer and thermodynamics. He has been deeply involved as a teaching assistant in all of these subjects, and enjoys lecturing as well as laboratory demonstrations.

Upon completion of his Master of Science degree in Mechanical Engineering, he hopes to be in a better position to offer his services in the field of energy systems and thermal energy storage through a successful engineering career. However, after a reasonable amount of industrial experience, he hopes his career will direct him back to the research field and possibly to continue instructing engineering students in the more important facets of mechanical engineering.